

Summer 2008

Tin dioxide nanoparticle based sensor integrated with microstrip antenna for passive wireless ethylene sensing

Mercyma Deeba Balachandran
Louisiana Tech University

Follow this and additional works at: <https://digitalcommons.latech.edu/dissertations>



Part of the [Electrical and Computer Engineering Commons](#)

Recommended Citation

Balachandran, Mercyma Deeba, "" (2008). *Dissertation*. 520.
<https://digitalcommons.latech.edu/dissertations/520>

This Dissertation is brought to you for free and open access by the Graduate School at Louisiana Tech Digital Commons. It has been accepted for inclusion in Doctoral Dissertations by an authorized administrator of Louisiana Tech Digital Commons. For more information, please contact digitalcommons@latech.edu.

TIN DIOXIDE NANOPARTICLE BASED SENSOR
INTEGRATED WITH MICROSTRIP ANTENNA FOR
PASSIVE WIRELESS ETHYLENE SENSING

by

Mercyma Deeba Balachandran, M. S.

A Dissertation Presented in Partial Fulfillment
of the Requirements for the Degree
Doctor of Philosophy

COLLEGE OF ENGINEERING AND SCIENCE
LOUISIANA TECH UNIVERSITY

August 2008

UMI Number: 3318922

INFORMATION TO USERS

The quality of this reproduction is dependent upon the quality of the copy submitted. Broken or indistinct print, colored or poor quality illustrations and photographs, print bleed-through, substandard margins, and improper alignment can adversely affect reproduction.

In the unlikely event that the author did not send a complete manuscript and there are missing pages, these will be noted. Also, if unauthorized copyright material had to be removed, a note will indicate the deletion.

UMI[®]

UMI Microform 3318922

Copyright 2008 by ProQuest LLC.

All rights reserved. This microform edition is protected against unauthorized copying under Title 17, United States Code.

ProQuest LLC
789 E. Eisenhower Parkway
PO Box 1346
Ann Arbor, MI 48106-1346

LOUISIANA TECH UNIVERSITY
THE GRADUATE SCHOOL

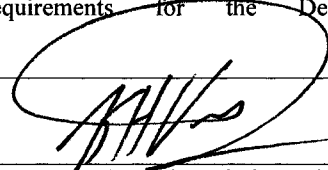
May 14, 2008

Date

We hereby recommend that the dissertation prepared under our supervision
by Mercyma Deeba Balachandran

entitled TIN DIOXIDE NANOPARTICLE BASED SENSOR INTEGRATED WITH
MICROSTRIP ANTENNA FOR PASSIVE WIRELESS ETHYLENE SENSING

be accepted in partial fulfillment of the requirements for the Degree of
Doctor of Philosophy in Engineering



Supervisor of Dissertation Research



Head of Department

Engineering

Department

Recommendation concurred in:

Yusuf K. Vol

Hafiz

Chris W.

Advisory Committee

Philip J. Coone

Approved:

Mercyma Deeba Balachandran

Director of Graduate Studies

Approved:

Wynne M. Brothey

Dean of the Graduate School

Stan Nagge

Dean of the College

ABSTRACT

In this dissertation, we present the development and integration of a passive ethylene gas sensor with triangular microstrip patch antenna for wireless monitoring of climacteric fruit freshness. The existing ethylene sensors are mostly SnO₂ resistor based active sensors, fabricated on rigid substrates requiring high fabrication temperatures and cannot be used for wireless applications. The proposed passive ethylene gas sensor is a novel nanoparticle based SnO₂ capacitive sensor which, unlike the other existing SnO₂ resistor based active thick film and thin film sensors, consists of 10 nm to 15 nm SnO₂ nanoparticles coated as a thin dielectric film of 1300 nm thickness. The nanoscale particle size and film thickness of the sensing dielectric layer in the capacitor model aids in sensing ethylene at room temperature and eliminates the need for micro hotplates used in existing SnO₂ based resistive sensors. In comparison to the high sintering deposition temperatures used for many currently available ethylene sensors fabricated on rigid substrates, the SnO₂ sensing layer is deposited using a room temperature dip coating process on flexible polyimide substrates. The capacitive sensor fabricated with pure SnO₂ nanoparticles as the dielectric showed a 5 pF change in capacitance when ethylene gas concentration was increased from 0 to 100 ppm. The change in capacitance was increased to 7 pF by introducing a 10 nm layer of platinum (Pt) and palladium (Pd) alloy deposited by sputter deposition. This also improved the selectivity of the sensor to ethylene mixed in a CO₂ gas environment. The response time was decreased to 3 min for SnO₂ samples

with Pt/Pd layer (5 min for pure SnO₂ samples) and its recovery time was decreased to 5 min compared to 7 min for pure SnO₂ samples.

The passive SnO₂ capacitive ethylene sensor is integrated with a triangular microstrip patch antenna using capacitively loaded integration methodology which represents a one of a kind passive wireless sensor tag used for detecting freshness of climacteric fruit. The integration methodology adapted also reduced the size of the triangular patch antenna by 63 percent. The decrease in sensor capacitance due to the presence of ethylene (0 to 100 ppm) changes the antenna resonant frequency by 7 MHz and return loss by 9.5 dB, which makes the system reliable for far field wireless ethylene monitoring applications. The sensor tag output was also detected using an RFID reader showing a change in demodulated signal amplitude of 3 mV. Experimental result is presented for detecting multiple sensor tags at varying distances based on the wireless measurement of return loss which eliminates the common distance problem existing in backscatter signal based tags.

APPROVAL FOR SCHOLARLY DISSEMINATION

The author grants to the Prescott Memorial Library of Louisiana Tech University the right to reproduce, by appropriate methods, upon request, any or all portions of this Dissertation. It is understood that "proper request" consists of the agreement, on the part of the requesting party, that said reproduction is for his personal use and that subsequent reproduction will not occur without written approval of the author of this Dissertation. Further, any portions of the Dissertation used in books, papers, and other works must be appropriately referenced to this Dissertation.

Finally, the author of this Dissertation reserves the right to publish freely, in the literature, at any time, any or all portions of this Dissertation.

Author B. M. Deibel

Date 05/14/2008

DEDICATION

This dissertation is dedicated in loving memory of my father Mr. D. P. Balachandran. He was a man of great wisdom, strength, and courage, and all that I am is because of him.

TABLE OF CONTENTS

ABSTRACT.....	iii
DEDICATION.....	vi
LIST OF TABLES.....	xi
LIST OF FIGURES.....	xii
ACKNOWLEDGEMENTS.....	xvi
CHAPTER 1: INTRODUCTION.....	1
1.1 Postharvest Handling of Fruits	1
1.2 Ethylene and Fruit Ripening.....	2
1.3 Research Motivation	3
1.3.1 Need for Wireless Fruit Freshness Detection	3
1.4 Overview of Sensor Tag for Fruit Freshness Detection	4
1.5 Contributions of the Dissertation.....	6
1.6 Applications.....	7
1.7 Organization of Dissertation.....	9
CHAPTER 2: RELATED RESEARCH.....	10
2.1 Ethylene Gas Sensors.....	10
2.1.1 Device Models	10
2.1.2 Sensing Materials.....	15
2.1.3 Fabrication Methods	16
2.1.4 Measurement Methodology	21
2.2 Integrated Sensor Antennas	22
2.2.1 Wireless Food Freshness Monitoring Systems	23

2.3	Present Work.....	24
CHAPTER 3: THEORY AND ANALYTICAL ANALYSIS.....		27
3.1	Theoretical Study of Ethylene Sensor	27
3.1.1	SnO ₂ Nanoparticles.....	27
3.1.2	Reaction Mechanism.....	29
3.1.3	Capacitive Ethylene Sensor	32
3.2	Antenna Theory	37
3.2.1	Theory and Simulation.....	38
3.2.1.1	Substrate.....	38
3.2.1.2	Skin Depth	39
3.2.1.3	Resonant Frequency.....	39
3.2.1.4	VSWR.....	41
3.2.1.5	Gain.....	41
3.2.1.6	Impedance.....	42
3.2.1.7	Backscattered Antenna Signal	43
3.3	Integration of Ethylene Sensor with RFID Tag Antenna	44
3.3.1	Load Integration to Antenna	44
3.3.1.1	Analytical Analysis.....	45
3.3.2	Direct Integration with Antenna	47
3.3.2.1	Theory	50
3.3.2.2	Simulations	51
CHAPTER 4: FABRICATION AND CHARACTERIZATION		54
4.1	Fabrication of Ethylene Sensor.....	54
4.1.1	Solution Preparation.....	55
4.1.2	Fabrication Steps and Techniques	55
4.1.3	Characterization of Deposited Layers.....	58
4.2	Fabrication of RFID Tag Antenna	62
4.3	Fabrication Steps for Sensor Integration with Antenna.....	64

CHAPTER 5: EXPERIMENTAL SET-UP	66
5.1 Ethylene Sensor	66
5.1.1 Experimental Set-up and Measurement Procedures	66
5.2 Ethylene Sensor Integrated with RFID Tag Antenna	68
5.2.1 Experimental Set-up.....	68
5.2.2 Measurement Techniques and Procedures.....	70
CHAPTER 6: RESULTS AND DISCUSSIONS	74
6.1 Ethylene Sensor	74
6.1.1 Experimental Results	75
6.1.1.1 Sensitivity and Reproducibility.....	75
6.1.1.2 Hysteresis.....	78
6.1.1.3 Degradation.....	80
6.1.1.4 Response Time and Recovery Time	82
6.1.1.5 Selectivity	83
6.2 Ethylene Sensor Integrated With RFID Tag Antenna	87
6.2.1 Simulation Results	88
6.2.2 Experimental Results	90
6.3 Multiple Tag Detection at Varying Distance.....	92
6.4 RFID Reader System	95
6.4.1 Reader Output Data.....	95
6.4.2 Experimental Results	96
CHAPTER 7: CONCLUSIONS AND FUTURE WORK.....	98
7.1 Conclusions.....	98
7.2 Future Work.....	101
APPENDIX A.....	104
APPENDIX B.....	108

REFERENCES.....111

LIST OF TABLES

Table 2.1	Comparison of sensing materials of existing ethylene sensors.....	16
Table 2.2	Summary of the technologies used for adding the catalysts.....	19
Table 2.3	Summary of research requirements, adopted technologies, and its advantages over the existing technologies	26
Table 6.1	Statistical data for sensitivity and reproducibility experimental data points.	76
Table 6.2	Statistical data for degradation study.....	81
Table 6.3	Comparison of slopes between day 1 and day 5 of the samples.....	82
Table 6.4	Statistical data for selectivity study	86

LIST OF FIGURES

Figure 1.1	Passive wireless sensor system for fruit freshness detection.....	5
Figure 2.1	Structure of Taguchi ceramic gas sensor [11]	11
Figure 2.2	Four element micro hotplate with SnO ₂ film for ethylene gas sensing [14]	12
Figure 3.1	SnO ₂ crystalline structure [66]	28
Figure 3.2	SnO ₂ nanocrystallites deposited by spray pyrolysis [67]	28
Figure 3.3	SnO ₂ nanoparticle in air (before exposure to ethylene).....	30
Figure 3.4	SnO ₂ nanoparticle in ethylene (after exposure to ethylene)	31
Figure 3.5	Cross section of the capacitive ethylene sensor model with SnO ₂ nanoparticles as the dielectric.....	32
Figure 3.6	Three-dimensional structure of the SnO ₂ capacitor model.....	34
Figure 3.7	Top view of dielectric region with SnO ₂ nanoparticles seen through the top copper plate before and after exposure to ethylene gas	35
Figure 3.8	Cross section of antenna substrate.....	38
Figure 3.9	Simulation model of triangular microstrip patch antenna with VSWR = 1.51 at $R_f = 915$ MHz.....	40
Figure 3.10	Gain of triangular microstrip patch antenna.....	42
Figure 3.11	Impedance of triangular microstrip patch antenna	43
Figure 3.12	Sensor connected as a load to antenna	44
Figure 3.13	Theoretical result for backscattered voltage when sensor capacitance is connected as a load to antenna	46

Figure 3.14	Different configurations for the direct integration of the sensor with antenna.....	48
Figure 3.15	Shift in frequency for change in capacitance for six different configurations of sensor integrated with the antenna.....	48
Figure 3.16	Comparison of methods of sensor integrated with antenna.....	49
Figure 3.17	915 MHz triangular patch antenna designed in the EM plane	51
Figure 3.18	Antenna integrated with capacitive sensor in the circuit level	52
Figure 3.19	Shift in R_f when capacitive sensor is directly integrated with the antenna	53
Figure 4.1	Fabrication steps for ethylene sensor on polyimide substrate.....	56
Figure 4.2	Structure of capacitive ethylene sensor	57
Figure 4.3	Fabricated capacitive ethylene sensor on polyimide substrate.....	58
Figure 4.4	Tencor measurement of copper thickness = 6934 nm, measured after reducing the thickness using etching.....	59
Figure 4.5	Roughness of the etched copper surface = 632 nm	59
Figure 4.6	Roughness of cellulose acetate layer coated on copper = 131 nm	60
Figure 4.7	Thickness of cellulose acetate insulating layer = 1226 nm	61
Figure 4.8	AFM image of SnO ₂ coated on PDDA (20 x 20 μ m area).....	61
Figure 4.9	Mask for the triangular antenna (a) top layout and (b) ground slot layout.....	62
Figure 4.10	Fabrication of microstrip antenna using photolithography	63
Figure 4.11	Triangular microstrip patch antenna (a) top surface (b) ground slot.....	64
Figure 4.12	Fabricated ethylene sensor integrated with triangular microstrip patch antenna	65
Figure 5.1	Experimental set-up for measuring ethylene sensors	67
Figure 5.2	Experimental set-up for wireless sensing of ethylene gas.....	69

Figure 5.3	Schematic diagram to show the interaction between reader antenna and sensor tag	70
Figure 5.4	Antenna return loss measured in the empty anechoic chamber before and after calibration	72
Figure 5.5	Distance optimization between the tag antenna and receiving antenna	73
Figure 6.1	Sensitivity and reproducibility of capacitive ethylene sensor to ethylene	75
Figure 6.2	Hysteresis of pure SnO ₂ dielectric layer capacitor when exposed to ethylene	79
Figure 6.3	Hysteresis of SnO ₂ with Pt/Pd dielectric layer capacitor when exposed to ethylene	79
Figure 6.4	Degradation of ethylene sensor for varying ethylene concentrations	80
Figure 6.5	Response time and recovery time of pure SnO ₂ and SnO ₂ with Pt/Pd to ethylene concentration	83
Figure 6.6	Concentration of CO ₂ present in warehouses [87]	84
Figure 6.7	Sensitivity of pure SnO ₂ and SnO ₂ with Pt/Pd layer to ethylene gas concentration mixed with CO ₂ gas	85
Figure 6.8	Modified triangular microstrip patch antenna resonating at 985 MHz with VSWR = 1.69	88
Figure 6.9	Circuit level model of sensor integrated with tag antenna	89
Figure 6.10	Simulation results for shift in R_f for change in capacitance of the sensor	90
Figure 6.11	Simulation and experimental data for shift in resonant frequency of antenna	91
Figure 6.12	Change in return loss with ethylene gas concentration	92
Figure 6.13	Experimental set-up for multiple tag testing at varying distances	93
Figure 6.14	Multiple tag detection at varying distances	94

Figure 6.15	Modular prototype of the RFID reader system.....	95
Figure 6.16	Experimental set-up for sensor tag detection of ethylene with reader	96
Figure 6.17	Reader output data of sensor tag sensing ethylene gas.....	97
Figure 7.1	Top view of interdigitated capacitor model.....	101

ACKNOWLEDGMENTS

I would like to express my sincere gratitude to my advisor, Dr. Kody Varahramyan, for his support, patience, and guidance. His technical and editorial advice has taught me innumerable insights on the workings of academic research and this dissertation. I also thank my advisory committee members Dr. Chester Wilson, Dr. Haifeng Ji, Dr. Yuri Lvov, and Mr. Philip Coane for their patient review of my work and helpful suggestions.

I am very thankful to Dr. Mangilal Agarwal for supervising this research and for taking the time to discuss technical details. My special thanks to Mr. Sudhir Shrestha and Dr. Jeevan Vemagiri for all the simulation help. It was a great pleasure to work with them. I also acknowledge the laboratory help provided by the late Mr. Tom Emory, Mr. Dee Tatum, Mr. Scott Williams, Mr. John McDonald, and Ms. Deborah Wood.

I convey my deepest thanks to all my friends for their constant prayers and encouragement. Finally, my utmost love and gratitude goes to my father, the late Mr. D. P. Balachandran, and my mother, Mrs. Mary Kalavathy, for their endless support and encouragement, without which none of this would have been possible.

CHAPTER 1

INTRODUCTION

Postharvest handling of fruits is one of the key factors in enriching the quality of fruits reaching the consumers. The harvested fruits are susceptible to several types of damage during storage and transport, which result in huge monetary losses. The research presented in this dissertation involves the realization of a passive wireless sensor tag for monitoring the freshness of climacteric fruits during postharvest storage and transport. The sensor tag is comprised of a passive ethylene gas sensor to detect ethylene gas emanated from climacteric fruits at various stages of ripening. The sensor is also integrated with a triangular microstrip patch antenna to interact wirelessly with a reader. The reader can receive data from the sensor tag, interpret, and conclude whether the fruit is raw, ripe, overripe, or spoilt. This passive wireless sensor tag will aid in the continuous monitoring of climacteric fruits in postharvest storage and transport which not only enhances consumer satisfaction, but also gives tremendous boost to the farmer's produce value by early detection of fruits in the process of spoilage.

1.1 Postharvest Handling of Fruits

The postharvest handling process of fruits consists of temporary storage in the production field, packaging, transportation, and retail storage [1]. Physical damages to

fruits occur because of improper handling in warehouse storage facilities, packaging, and transportation. Environmental damages occur during storage and transportation due to inappropriate temperature conditions resulting in either high temperature burns or chilling injuries. Damages due to diseases caused by organisms occur during all stages of produce, packaging, storage and transport. All the above mentioned damages result in accelerated rotting. Even though modern automated produce handling equipments, temperature controlled warehouse facilities, and postharvest pest control treatments have reduced losses and increased shelf life, ripeness accelerating gas emanated by the climacteric fruit itself still pose a great threat to postharvest damages.

1.2 Ethylene and Fruit Ripening

Ethylene is a naturally occurring gaseous plant hormone which affects the growth and development in all plants [2]. It is the key factor for initiating the ripening process in many fruits and for accelerating the aging process, thereby reducing the quality and shelf life of produce during postharvest transits. Based on the emission of ethylene during the ripening process, all fruits are classified into climacteric and non-climacteric. Climacteric fruits have a high respiration rate during the process of ripening and thereby produce high levels of ethylene gas. Also, the presence of ethylene gas initiates the ripening process in raw and matured climacteric fruits. Thus, we see the common phenomena of one ripe fruit in a box resulting in accelerated or even premature ripening of unripened fruits around it. Some of the examples of climacteric fruits are apples, pears, watermelons, bananas and mangoes. Non-climacteric fruits do increase in respiration while ripening but ethylene plays a negligible role or practically no role in the actual initiation of ripening. Hence non-climacteric fruits remain in the same stage of ripening after it is

picked from the plant. Some of the examples of non-climacteric fruits are cherries, grapes, strawberries, oranges and pineapples.

Postharvest handling of climacteric fruits is more difficult than the non-climacteric counterpart as the ripening process continues even after the fruit is picked from the plant and the ethylene gas emanated during ripening drastically enhances the ripening process in the fruits around it leading to overripeness and decay.

1.3 Research Motivation

In the United States, almost 23 percent wastage of fruit occurs every year in the postharvest handling [3]. The losses are much higher in developing countries and reach as high as 50 percent in under-developed countries. It is of great importance that the wastage and the huge monetary losses are reduced. As mentioned earlier, climacteric fruits continue to ripen naturally even after being picked from plants and the ripening process is further accelerated by the excess emission of ethylene gas produced by over ripened and damaged fruits. This not only affects the already ripening fruit but also causes premature ripening of raw fruit. Physical examination and removal of over ripened and damaged fruit can greatly curb the damage to other good fruit in the box. But this involves tedious physical examination of each fruit in a box which corresponds to enormous consumption of time and manual labor and practically impossible for millions of boxes shipped every day.

1.3.1 Need for Wireless Fruit Freshness Detection

Climacteric fruits emit different levels of ethylene (C_2H_4) gas at different stages of the ripening process and can function as a freshness marker [4]. When fruit begins to over ripen or is subjected to damage, there is a sudden increase in the overall ethylene

levels inside the storage box. Continuous monitoring of ethylene gas levels in each box can pave the way to detect abnormal increase in levels and the box can be examined for the cause. If the increase in ethylene gas is due to one or more overripe fruits or a damaged fruit, they can be physically removed, thus protecting the entire box from being damaged. The most important component for the above mentioned detecting system is an ethylene gas sensor to detect the quantity of ethylene gas emanated from the fruit. The ethylene detector or sensor, when integrated with an interpreting and communicating system, automatically alarms the user and thus the human intervention is reduced to simply checking that particular box and discarding the rotten fruit and preserving the freshness of the remaining fruit. This dissertation is the development of such a passive sensor tag system to detect ethylene and wirelessly transmit the data to a Radio Frequency Identification (RFID) reader.

1.4 Overview of Sensor Tag for Fruit Freshness Detection

The wireless sensor tag for climacteric fruit freshness detection consists of an ethylene gas sensor integrated with a microstrip patch antenna which can be read by an RFID reader, as shown in Figure 1.1. The integrated sensor antenna constitutes an Radio Frequency (RF) wireless sensor tag that is capable of sensing, receiving, and transmitting RF signals at 915 MHz without an identification circuit. A single sensor tag is placed on the inside top surface of a fruit carton, box or bag that is used for storage or transport. The ethylene sensor integrated with the RFID tag antenna senses the ethylene gas emanated from the fruit and changes its electrical parameters (e.g., resonant frequency). The change in the sensor electrical parameters is directly related to the sensed quantity of ethylene gas. The changes in the sensor parameters affect the RFID tag antenna

characteristics. The antenna parameter variation due to the presence of ethylene is detected wirelessly by the RFID reader. The ethylene gas level variation is detected by the reader by monitoring the change in the amplitude of the received signal. The reader analyzes the variations and interprets the received data from the sensor tag to indicate to the user whether the box of fruit is in good freshness status for shipping or storing.

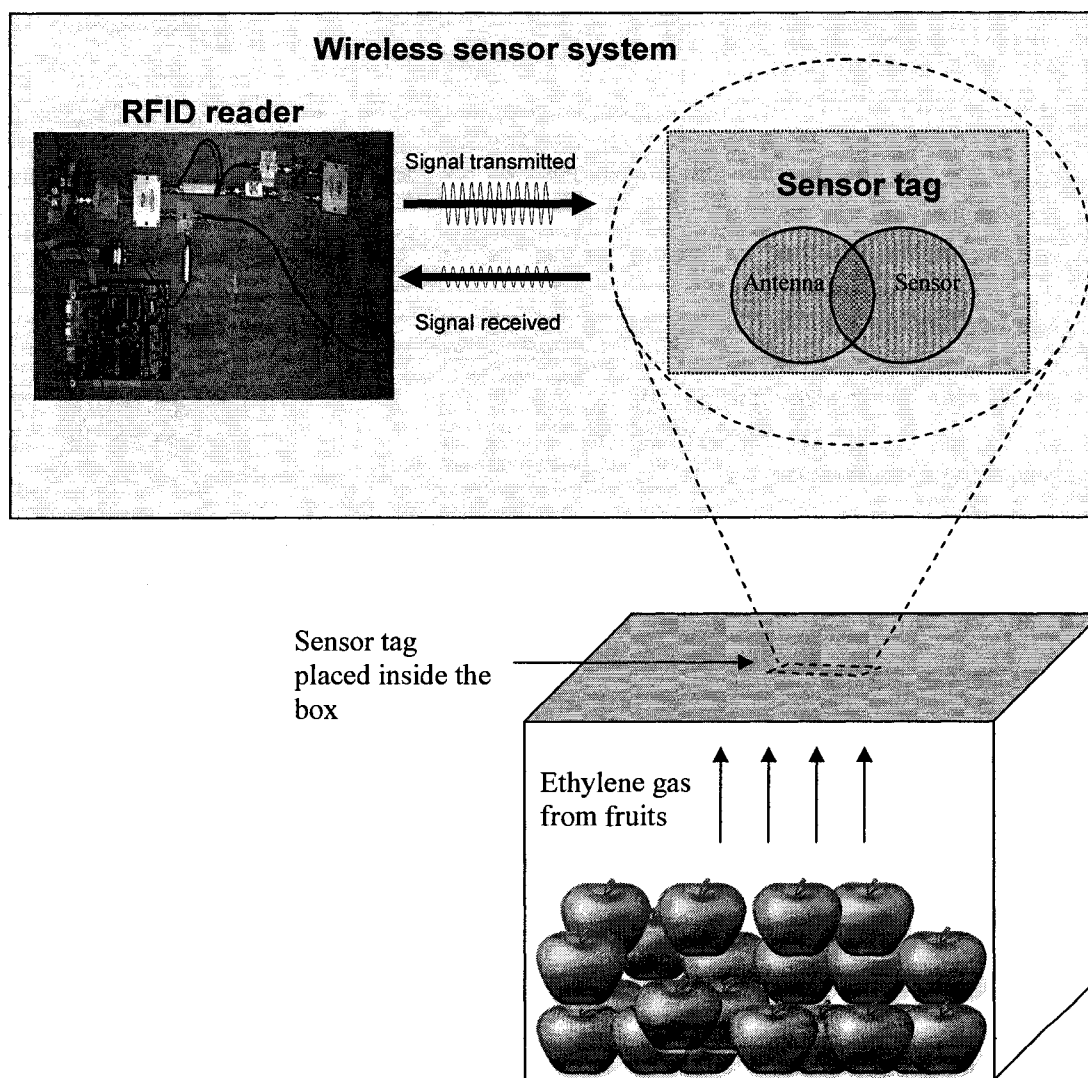


Figure 1.1 Passive wireless sensor system for fruit freshness detection.

The reader transmits and receives the RF signal at the user defined time intervals. For example, the signal can be transmitted and received once every hour or two hours based on the requirements. The received data is collected by the reader and is compared with the transmitted signal to detect the concentration of ethylene present in the box. If there is an increase in the concentration level, the reader alerts the user. The emission of ethylene from climacteric fruits is classified into low, medium and high based on the parts per million (ppm) levels [5]. Fruits like banana, guava, and mango have a low level ethylene gas emission of less than 10 ppm. Pears, cantaloupe, and peaches emit about 50 ppm and are classified as medium level emitters. Passion fruit, apple, and sapota have a high level emission of about 100 ppm. Based on the commodity that has to be monitored, the reader alarm level can be set for distinguishing between unripe, ripe, and overripe. A detailed description of sensor and antenna is given in Chapter 3.

1.5 Contributions of the Dissertation

The contributions of the dissertation are as follows:

- A novel capacitor based ethylene gas sensor with SnO₂ nanoparticles as the sensing dielectric layer was developed and tested. The capacitor model provides a greater ease of integration with passive RFID tags compared to resistor based counterparts with respect to impedance matching.
- The SnO₂ nanoparticle based ethylene sensor was fabricated at room temperature using a low cost dip coating technique on flexible polyimide substrates, which is a significant improvement over other high temperature and expensive fabrication processes on rigid substrates.

- The dissertation demonstrates the sensing capabilities of SnO₂ nanoparticles at room temperature, eliminating the need for a power supply or onboard battery as in the case of other SnO₂ based ethylene sensors. Pure SnO₂ nanoparticle based capacitor samples showed a change of 5 pF (from 0 to 100 ppm of ethylene gas concentration) and the samples with platinum (Pt) and palladium (Pd) layers alternated with SnO₂ nanoparticle layers showed a change of 7 pF.
- This work presents a novel capacitively loaded integration methodology to integrate the ethylene gas sensor with a triangular microstrip patch antenna. The sensor tag represents a one of a kind passive and wireless sensor tag that is used for detecting freshness of fruits. The integration methodology adapted also reduced the size of the triangular patch antenna by 63 percent.
- The dissertation reports on a passive sensor tag operating at 915 MHz (compared to 13.56 MHz systems) which wirelessly interacts with an RFID reader. The principle of detection is based on the change in resonant frequency and return loss of the RFID tag antenna being proportional to the ethylene gas concentration thus making the system reliable for far field wireless monitoring applications.
- A preliminary result has been presented for detecting multiple sensor tags based on the wireless measurement of return loss. This method also aids in eliminating the common distance problem existing in these types of tags.

1.6 Applications

The sensor tag developed was tested for applications pertaining to monitoring fruit freshness in various stages of postharvest fruit handling. Given the wireless

measurement system and the passive nature of the sensor, the application can also be extended to the following areas of ethylene gas sensing requirements.

1. The sensor tag can be used for applications related to detecting faulty power transformers based on the levels of ethylene gas emanating from them [6]. The wireless and continuous monitoring system presented in this dissertation can alert the user in advance and prevent sudden shutdowns and huge power outages.
2. Another application of the sensor tag is to wirelessly monitor the ethylene gas levels in the atmosphere. Ethylene gas is known to be a precursor for ozone gas (O_3) formation [7]. A high level of ozone gas content in a human respiration system causes headaches, chest and throat pains [8]. Hence, it is important to monitor the ethylene gas levels as the higher the precursor, the higher the production of ozone. The need for the constant ethylene monitoring in this area of need can be fulfilled by using the sensor tag placed at an elevated ground level and the ethylene levels can be wirelessly recorded by the RFID placed on the ground.
3. Ethylene is produced by lipid peroxidation (cell membrane degradation) in human leukemic cells [9]. Hence, measuring the ethylene gas content in human breath can reflect a diseased cell condition. In this regard, the wireless RFID sensor system can aid in monitoring the patient's exhaled ethylene content.
4. Elevated levels of ethylene content causes rapid shedding of buds, flowers, and leaves, stunted growth, and chlorosis [10]. The wireless ethylene monitoring system can be very handy in the continuous monitoring of the ethylene gas levels

without any human intervention, such as in a green house. The RFID reader can also be programmed to control an exhaust to dispose the excess ethylene.

1.7 Organization of Dissertation

Chapter 2 discusses the related research work in the field of ethylene gas sensors with respect to device configuration, sensing materials used, fabrication methods followed, and measurement methodologies pursued. The later part of the chapter gives an overview of approaches adapted for integrating sensors with antennas. Chapter 3 details the ethylene sensor and its integration methodology with RFID tag antennas. It also reviews basic concepts of the RFID system with respect to RFID tags and sensor tags. Chapter 4 presents the theoretical study of the ethylene sensor with respect to the sensing layer's response to ethylene gas concentration. It presents the theoretical and analytical study of the triangular patch antenna and its change in characteristics when ethylene is sensed. This chapter also discusses the simulation design criteria for the antenna followed by the sensor integration methodology. Chapter 5 gives a detailed account of the procedures and steps involved in the fabrication of the sensor and antenna. Chapter 6 presents the experimental results of a stand alone ethylene sensor, highlighting the sensor's sensitivity, selectivity, repeatability, reproducibility and response time. It also presents the simulation and experimental results for the integrated sensor tag measured using a network analyzer and RFID reader. Chapter 7 summarizes the contributions of the research and envisages the research directions and improvements.

CHAPTER 2

RELATED RESEARCH

This chapter presents an overview of the existing ethylene gas sensors, classified and presented according to the device model, sensing materials, fabrication techniques and measurement methodologies. The later part of the chapter gives an overview of the approaches adapted for integrating sensors with antennas.

2.1 Ethylene Gas Sensors

The key aspects of an ethylene gas sensor are device configuration, sensing materials used, fabrication methods followed, and measurement methodologies implemented. Based on the viability, area of research need, and platform of implementation, specific sensor parameters are considered. Given below are the related research works for the specific sensor parameters.

2.1.1 Device Models

The device modeling for an ethylene sensor depends on the sensing material's characteristic variations to the stimulant. Hence, the modeled sensor device can be linear or non-linear, active or passive and, based on the configuration and simplicity of its design, its ease of integration with other systems can be predicted. Given below are the existing device configurations for ethylene sensors.

1. Resistor based ethylene sensor

One of the earliest and the most famous commercial gas sensors was reported by Taguchi in 1971 using SnO_2 sintered on a ceramic tube [11]. The sensor is a simple resistor based device which is widely used for detecting carbon monoxide, benzene, isopropyl alcohol and other hydrocarbons [12]. The sensing SnO_2 paste is coated on a ceramic substrate which consists of a single heating filament passing through the ceramic substrate. When electricity is passed, the heater element heats up the ceramic substrate and the heat is transferred to the sensing SnO_2 paste. In the presence of a stimulant, the resistance changes and this change in resistance is measured between the electrode metallization. Figure 2.1 shows the structure of a Taguchi ceramic sensor with the heater coil placed inside the ceramic tube.

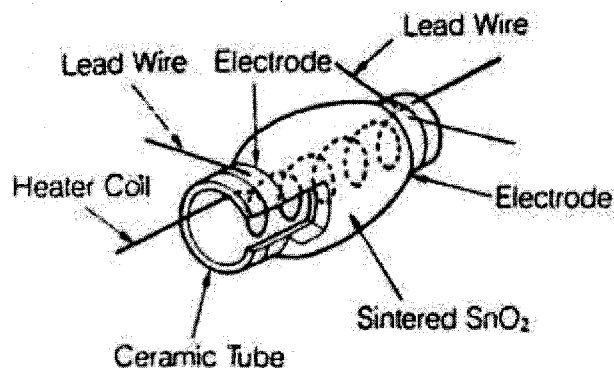


Figure 2.1 Structure of Taguchi ceramic gas sensor [11].

The sensor consumes about 0.6 W of power due to the use of the heater element and is bulky in structure. The change in resistance in the presence of a stimulant is detected by using an external circuit which measures the change in resistance by measuring the voltage drop across the sensing resistor. Though the sensor is low cost, has

good sensitivity and fast response, it lacks reproducibility, selectivity, and requires a heater element [13].

Ivanov, et al. in [14] reported a considerable improvement in the selectivity using an SnO₂ resistor based device doped with platinum (Pt) and palladium (Pd) particles. A low cost screen-printing technique is used to fabricate a four membrane sensor array to monitor ethylene gas concentration in warehouses (Figure 2.2).

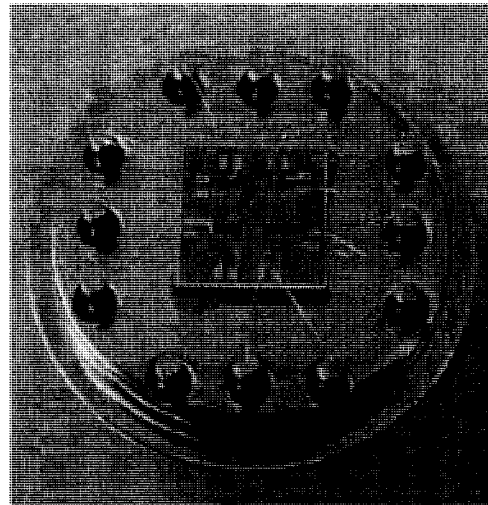


Figure 2.2 Four element micro hotplate with SnO₂ film for ethylene gas sensing [14].

The array arrangement with the various sensing materials was done to increase the selectivity of the micro-system to detect ethylene. Tin and tungsten oxides (SnO₂ and WO₃) doped with Pt, Pd, and gold (Au) used as a resistor model were used to detect the gases. Qualitative and semi-quantitative analysis was performed on the gases using principle component analysis (PCA). Even though the size of the sensor is reduced and the sensor is planar in structure when compared to the Taguchi sensor, the sensor still requires a heater element. Also, the sensor is affected by humidity.

Giberti, et al. in [15] achieved humidity compensation by implementing an algorithm based on the Claypeyron equation. The sensor used was a resistor model with SnO_2 as the sensing layer deposited as a thick film on a precut alumina substrate equipped with a heater on the back side. The temperature of the heater element is controlled by using a platinum resistor with interdigitated contacts. Even though the work quantified low ethylene concentrations (0 to 14 ppm) in 64 percent of relative humidity, the sensor is still operable only at 300^0 C and thus requires a heater element.

2. *Diode based ethylene sensor*

Kang, et al. in [16] reported Aluminium Gallium Nitride/Gallium Nitride (AlGaN/GaN) based diode and gateless high electron mobility transistor (HEMT) for ethylene gas detection. The device can operate at wide range of temperatures and presents a platform for integration with on-chip signal processing circuitry for remote sensing. The sensor is active and has cross sensitivities to other gases. He also reported another AlGaN/GaN MOS diode and ZnO schottky diode in [17] showing a much higher absolute change in sensor characteristics (current or voltage). In [18], Cheraga, et al. proposes a metal insulator semiconductor (MIS) diode and demonstrates a high sensitivity to ethylene gas using PS/ CH_x sensor configuration. The current-voltage characteristics change at the heterojunction of the structure in the presence of sensing gas changes the conductivity which was analyzed using infra-red spectroscopy. The sensor also responds to ethane and propane. The sensor showed good stability even after six months with good response time and recovery time.

3. *Field Effect Transistor based ethylene sensor*

Winqvist, et al. reported ethylene gas detection using platinum based MOSFET and palladium based MOSFET in [19] and [20] respectively. In the platinum based model, the output data of the sensor is analyzed using gas chromatography. For the calibration of the sensor, the sensor sample was flushed with different gas concentrations and registering the voltage drop across the sensor for different sensor concentrations. The sensor's sensitivity increased sharply from 160⁰ C to 210⁰ C but operating the sensor at higher temperature and analyzing the data using gas chromatography method increases the chances of electronic noise mixing with the experimental data set.

Results shown by Winqvist demonstrate the detection of low concentrations of ethylene (1 ppm) at a lower temperature of 190⁰ C. But platinum and palladium MOSFET shows maximum sensitivity to 1, 3-Butadiene at the same operating temperature which indicates that the device is more sensitive to 1, 3-Butadiene than ethylene.

4. *MNOS capacitor based ethylene sensor*

Pietrucha, and Lalevic in [21], reported a Metal Nitride-Oxide Semiconductor (MNOS) capacitive device to detect ethylene gas. The measurements were done at room temperature and the system proved to be reliable. In this structure, 80 to 100 nm of tin oxide is deposited on a 5 to 10 ohm cm p-type silicon substrate. The tin oxide was deposited using chemical vapor deposition and the palladium film was applied using electron beam evaporation. In this model, the ethylene gas changes the work function of the device. However, the device required partial hydrogen coverage at all times and response time was as high as 27 minutes.

2.1.2 Sensing Materials

Choosing the right material is an important aspect of sensor fabrication. Given below is a detailed analysis of currently available materials for ethylene sensing.

SnO₂ is the most common material for ethylene sensing as indicated in [14], [15], and [22]. The SnO₂ particles range from 4 nm to 40 nm in particle size. The materials are coated as either thick film or thin film and the porosity of the layer formed enhances the sensitivity of the material. SnO₂ nanoparticles are also well suited for doping other materials like platinum and palladium.

Recently, tungsten trioxide (WO₃) has been the new material of interest after Pitcher, et al. proved its sensitivity to ethylene gas in [23]. WO₃ also increases in conductivity when exposed to ethylene gas but the electrical change is small when compared to SnO₂ based sensors. Another material which has good sensitivity to ethylene concentrations less than 1 ppm is titanium dioxide (TiO₂), as reported in [24]. The platinum doped TiO₂ coated magnetoelastic sensor operates at room temperature. For all the above mentioned materials, doping the pure material with palladium or platinum has shown considerable increase in sensitivity and selectivity. Palladium and platinum have a tendency to absorb ethylene gas molecules, as observed in [25] and [26]. Hence, they are used as catalysts to enhance the sensitivity of the sensing material to ethylene. In [27], other materials like ZnO₂, Pt and Pd doped silver, Iridium and Nickel have been tested for ethylene sensitivity. Table 2.1 charts the applicability of the ethylene sensing materials reported in previous works to the requirements of the passive wireless sensor tag approach to fruit freshness detection. For example, most of the ethylene sensing materials are commercially available in nanoparticle form and can be coated using layer-

by-layer (LbL) or dip coating technique for simplicity and room temperature fabrication. Materials are ranked from 1 through 10 with 1 being the most suited and 10 being the least suited with *X* indicating the unavailability of data. From the table given above, we can see that pure SnO₂, Pt doped SnO₂, and Pd doped SnO₂ are well suited for our application.

Table 2.1 Comparison of sensing materials of existing ethylene sensors.

Sensor characteristics	SnO ₂	TiO ₂	WO ₃	ZnO ₂	Pt	Pt/SnO ₂	Pd/SnO ₂	PtIr	PdAg	PdNi
Sensitivity	1	8	7	9	10	3	4	6	2	5
Selectivity	7	8	<i>X</i>	10	<i>X</i>	1	3	5	2	9
Passive	<i>Yes</i>	<i>Yes</i>	<i>No</i>	<i>No</i>	<i>No</i>	<i>Yes</i>	<i>Yes</i>	<i>No</i>	<i>No</i>	<i>No</i>
Change in electrical	3	8	9	10	4	1	2	6	5	7
Cost	2	9	3	1	10	6	5	8	7	4
Fabrication methods	<i>LbL/ Dip coat</i>	<i>LbL/ Dip coat</i>	<i>X</i>	<i>Spin/ Dip coat</i>	<i>LbL/ Dip coat</i>	<i>LbL/ Dip coat</i>	<i>LbL/ Dip coat</i>	<i>X</i>	<i>LbL/ Dip coat</i>	<i>LbL/ Dip coat</i>
Response time	<i>Good</i>	<i>X</i>	<i>X</i>	<i>X</i>	<i>X</i>	<i>Good</i>	<i>Good</i>	<i>X</i>	<i>X</i>	<i>X</i>
Repeatability	4	2	3	6	<i>X</i>	1	5	<i>X</i>	<i>X</i>	<i>X</i>
Stability	2	4	<i>X</i>	6	1	3	5	<i>X</i>	<i>X</i>	<i>X</i>
Response to 915 Mhz signal	<i>X</i>	<i>X</i>	<i>X</i>	<i>X</i>	<i>X</i>	<i>X</i>	<i>X</i>	<i>X</i>	<i>X</i>	<i>X</i>

2.1.3 Fabrication Methods

This section gives an outline description of the fabrication technologies currently present for ethylene sensors. The SnO₂ sensing film is deposited as either a thick film or thin film and based on the film thickness, various fabrication procedures are followed.

Thick film sensors are usually fabricated on ceramic Al_2O_3 substrates. In [28] the thick sensitive SnO_2 film of thickness $30\ \mu\text{m}$ was prepared by pressing SnO_2 powders and heat treating at 650°C . The heat treating process reduces the surface area of the sensing nanoparticles which increases the sensitivity. The powder was then prepared as a paste by mixing and firing in an organic vehicle and coated on 96 percent alumina. In [29], Th. Becker, et al. described a SnO_2 thick planar film of $30\ \mu\text{m}$ thickness obtained using screen printing technology. The sensing layer was coated on ceramic Al_2O_3 substrates with a Pt electrode for electrical characterization and a Pt meander pattern heater element for heating the sensing film placed on the backside of the substrate.

Thin film deposition methods involve methods like chemical vapor deposition (CVD), and physical vapor deposition (PVD). CVD and PVD methods deposit about 20 to 1000 nm of layer thickness. In CVD, the film growth occurs at high temperatures and in the PVD process deposition occurs at lower deposition temperatures with lower deposition rates. In [30], Jordan, et al. proved that CVD is a good fabrication technique to increase the sensitivity of the stimulant and avoid the effect of humidity. Thin film SnO_2 sensors are also fabricated by evaporating tin on a ceramic substrate and oxidizing the metal film by spraying SnCl_4 at high temperatures (calcined at 600°C) [31]. These sensing layers are too rigid and stable to fully undergo the reaction with the stimulant. To overcome the drawback, Taguchi sensors are fabricated by sintering powdered SnO_2 with stearic acid on a ceramic substrate at elevated temperatures [11]. The high temperature evaporates the stearic acid leaving a porous SnO_2 film with higher rate of change of conductivity when exposed to ethylene.

In [29], Th. Becker, et al. shows that thick film SnO₂ sensors are used in many commercial sensors due to the materials used and the well optimized fabrication steps followed. Thick films also show better stability than thin films due to its tolerance for high temperature operation. However, they require high fabrication temperatures and are difficult to fabricate on flexible substrates. They are also very bulky and consume very high power due to the heater element.

The other fabrication method for depositing SnO₂ and WO₃ is the screen printing technique [32]. In this technique, SnO₂ nanopowders are mixed with a carrying vehicle of terpeneol and the mixer is coated using a high precision printing machine to form a thin 5 μm sensing layer which enhances with 40 nm particle size. This method of deposition leaves a highly porous surface enhancing the sensing capabilities. In [33], Cavicchi, et al. reported a sol gel technique for preparing SnO₂ films. This method is a useful technique for doping other materials like palladium and platinum. In this process, salt solutions like SnCl₄, organic tin compounds, or pure metals are dissolved in nitric acid. Catalysts are usually calculated as a weight percentage in the range of 1 to 3 percent and introduced to the solution. In [34], a simple spin coating technique is given as an attempt to increase the selectivity and sensitivity. In this method, high temperature is used only for the preparation of the sensing nanoparticles and the deposition is at room temperature. A very uniform film is formed after the deposited layer is fired at 400⁰ C. It can be seen that all the above mentioned fabrication methods use high temperature for particle fabrication, coating, and deposition.

Most of the above mentioned fabrication methods also involve doping of materials to increase the sensitivity and selectivity of the sensors. The doped materials act

as catalysts. Materials like Pd and Pt added with SnO₂ create more reactive ions and speed up the reaction process. Typical catalysts are noble metals like Pt, Pd, Au, or Ag [14][19][20]. The fabrication processes involved in depositing the additives are given below in Table 2.2.

Table 2.2 Summary of the technologies used for adding the catalysts.

<i>Technology used for adding catalysts</i>	<i>Catalytic materials</i>
Laser induced pyrolysis	Nb [35], TiO ₂ [36]
Sputtering	TiO ₂ [37], Pt [38], Pd [39], MgO [40]
Impregnation	Pt [41], Pd [42]
Electron beam evaporation	Pd [43], TiO ₂ [43]
Pulsed laser technique	Pt [44] , Pd [45]

Laser induced pyrolysis is a method in which the catalysts are added as clusters to the material [35][36]. Ultra fine particles are deposited by using precursors inside a flow reactor. Heterogeneous clusters can also be easily produced by mixing the precursor gases. This method also aids in the ease of control of the additive's concentration and the percentage of mixer with the material.

Sputtering is a method where the doping material is evaporated at high temperature in vacuum and deposited on the material to be doped [37][38][39][40]. In this method the doping material is taken as the target and high energy ions are made to bombard the target to eject atoms from the target material and deposit on the substrate. This method can be used on any substrate and is usually for depositing thin films at an energy of 10 to 100 eV.

Impregnation is a process where the catalyst is used in the form of pellets which is repeatedly dipped in the catalytic agent [41][42]. This process is best suited for noble metal catalysts. The liquid penetration of the catalytic is done using techniques like pressurizing, vacuum treatment, and acoustic activation. The solution is evaporated at high temperatures and the precipitate left behind is the additive mixed with the agent.

Electron beam evaporation is another technique used for doping SnO₂ material [43]. The dopants like Pd or Pt is used as the target sample anode which is bombarded with electrons originating from a tungsten filament maintained under high vacuum. The bombarding electron beam transforms the target material into vapor phase and these gaseous atoms deposit as a thin layer on the SnO₂ material. This technique yields high deposition rates of 0.1 μm/min to 100 μm/min at temperatures.

Pulsed laser deposition (PLD) is also similar to electron beam technique where a high power laser beam is focused [44][45] on the target material under high vacuum . This process occurs in the presence of a background gas, such as oxygen to oxidize the deposited film.

Another method of additive deposition is the electroless technique. This technique involves electrochemical reaction where the catalyst is mixed in an aqueous solution. A palladium catalyst is mixed with tin oxide by mixing stannous chloride and palladium chloride in an acidic aqueous solution which contains excess chloride ions. The tin oxide particles reduce the palladium species through a redox reaction and the resulting solution formed in a colloidal mixture of suspended particles.

2.1.4 Measurement Methodology

The existing measurement methods for ethylene detection involve complex monitoring and interpreting systems like gas-chromatography, laser technique, chemiluminescence method, IR- spectroscopy and Photoluminescent [47][48][49][50]. Gas chromatography involves the sample collection and injecting into a chromatography tube and is absorbed by an inert absorbing sheet. This method is useful in measuring very low levels of ethylene (below 1 ppm) but is bulky and in-situ measurement is not possible.

Laser measurement technique involves the use of pulsed cascade lasers focused on the sample and the absorption spectrum is analyzed. Based on the peaks of absorption, ethylene concentration as low as 2 ppb can be detected with a very short response time. However, it is a very expensive and bulky system of measurement. IR-spectroscopy is used for detecting ethylene gas above 20 ppm as lower ppm of hydrocarbon gas such as ethylene has no effect on the sensing method.

The invention reported in [51] uses a sensor, microprocessor, compressor, humidifier, vacuum pump, O₂/CO₂ generator and anion generator to detect gases from vegetables and maintains the freshness by controlling the humidity, temperature, pressure, O₂/CO₂ and anion levels. The sensor used is a SnO₂ or TiO₂ sensor to detect gaseous sulphides from vegetables and Trimethylamine (TMA) from fish respectively. The device control is done using a microprocessor which compares the data read from the sensors to the already charted data for fresh vegetables. The device is bulky and uses microcontrollers for the sensing applications.

2.2 Integrated Sensor Antennas

Recently, the integration of sensor with microstrip antenna has proved to be a convenient method for wireless sensing due to the application of microstrip antennas in RFID tags. The earliest work on a sensor integrated with an antenna was reported in [52] for sensing the moisture content in a slurry using a circular patch antenna. The sensing material was used as the dielectric and its permittivity changes with respect to the moisture content in the slurry. The change in permittivity shifts the resonant frequency of the antenna by 0.035 GHz for 0 to 100 percentage change in moisture content. Similar work for humidity sensing was reported by Chang, et al. in [53] by modifying the polyimide dielectric layer. A total change of 7 MHz shift in frequency was observed for a 0 to 100 percentage variation in relative humidity. The sensor antenna is also integrated with a tag chip and the data is transmitted wirelessly to be read by an RFID reader. Another complete RFID humidity sensing system was reported in [54] by Harpster, et al. The paper reports a single chip integrated humidity sensor interacting with an antenna using inductive coupling. This means that the antenna has to be placed at the very close range of 0.6 cm. The results also showed a very small variation of 0.25 MHz frequency shift. Denoth, et al. in [55] demonstrated a practical snow and soil wetness sensor. A monopole antenna of 4 mm in diameter and operating in the range of 0.2-2 GHz was used as an in-situ measurement method. The measurement error for liquid was about $\pm 0.7\%$ and $\pm 2\%$ for soils.

Bogosanovich, et al. in [56] presented a sensor for measuring the permittivity of materials using a rectangular microstrip patch antenna by directly using the solid or liquid material under measurement as the dielectric layer of the antenna. Different permittivity

of the materials under measurement changes the resonant frequency of the antenna which compared well with the theoretical calculations. Solids such as PTFE, nylon, thordon, and acrylic and liquids such as water, ethanol, and pentanol were measured with good accuracy.

Another improved method of a sensor integrated with an antenna was reported by Thomy, et al. in [57]. A metallic sheet antenna without a substrate is used to detect temperature in harsh environments such as deep freezing conditions. The system is applicable to the temperature control of food products.

All the above mentioned integration methodologies require the modification of existing antennas as the sensing layer is integrated as a dielectric. This also inhibits the complete diffusion of the sensed quantities as the sensing layer is mostly covered by the top reflecting surface of the antenna.

2.2.1 Wireless Food Freshness Monitoring Systems

In [58], Nambi, et al. reported a wireless biosensor for detecting food pathogens using an RFID sensor system. The system proposes a commercial biosensor detecting Salmonella and E. Coli integrated with a 13.56 MHz RFID tag. The tag operates in the near field range and the integration of the sensor with the tag is through a microcontroller.

The invention given in [59] reports a perishable integrity sensor integrated with a RFID transponder. The sensor monitors the time and temperature, thereby giving the percentage of shelf-life remaining. The transponder uses an internal clock, memory units and sensor connected together through a chip with interface connections. The data is stored in the memory and is transmitted wirelessly to an interrogator. The RFID

transponder is bulky and expensive and requires power to run the complex circuits. It also requires Arrhenius plots to compare and interpret the data. One of the main disadvantage in this system is the chance of missing data (rise or fall in temperature) when the sensor is in the sleep mode. In [60], Vergara, et al. demonstrates a fruit quality RFID sensor system using three fabricated sensors based on Pt and Au doped SnO₂ sensors and Au doped WO₃ sensor. The sensors are integrated on a commercially available RFID transceiver operating in 13.54 MHz. The data analysis is performed using fuzzy ARTMAP classifier.

2.3 Present Work

The related research works in the field of ethylene sensors and sensors integrated with antennas have many drawbacks when applied to a passive sensor tag platform. Our current work requires an ethylene sensor which is passive, uses low temperature fabrication and is easy to integrate with RFID tag antenna [61]. All of the existing ethylene sensors are resistor based devices. The pure SnO₂ resistor based sensor's resistance before exposure is about 6 K Ω and after exposure to ethylene gas reduces to about 5 K Ω . When these sensors are integrated with a 50 Ω impedance RFID tag antenna, the device will be highly impedance mismatched and the change will have no effect on the antenna characteristics. Our research has presented a capacitor model in the range of 1 to 10 pF by using the dielectric property of SnO₂ particles as mentioned in [62]. Even a small change of 1 pF shifts the antenna R_f by 10 MHz.

Moreover, the existing resistor based bulk (sensing layer thickness is 5 μm and higher with particle diameter of ca 40 nm) ethylene sensor models need a heater element for sensing the stimulant. This is unsuitable for integration with passive RFID tags. In

our present work, the use of the nanoparticle based SnO₂ capacitive model overcomes the drawback by increasing the sensitivity of the sensor to the stimulant by decreasing the sensing layer thickness and particle size mentioned in [63]. In [64], Gong presents that the smaller the SnO₂ particle diameter, the larger is the surface to volume ratio resulting in low sensing temperature. The ethylene sensor presented here, has an SnO₂ nanoparticle diameter of 10 to 15 nm and thickness of 1300 nm which enables the sensor to sense ethylene gas at room temperature.

The overview of the existing sensor antenna integration methodologies indicates that almost all the papers presented the case wherein the sensing layer constitutes the dielectric layer of the antenna. This requires alteration to the existing antenna and inhibits the complete diffusion of the stimulant due to the top reflecting surface of the antenna. We have presented a capacitively loaded technique mentioned in [65] for integrating the ethylene sensor to the triangular microstrip antenna. In this method, the capacitive sensor is fabricated in parallel with the antenna. Hence, the necessity to alter the existing antenna is prevented. This method also reduces the size of the antenna (explained in detail in section 3.3).

Compared to the existing complex measurement methods and commercially available handheld ethylene detectors, the passive sensor tag interaction with the RFID reader proves to be a good measurement methodology for wireless sensing without human intervention. The sensor tags designed to sense ethylene gas wirelessly communicates with a RFID reader which has the capability to interact with multiple tags and send the analyzed and interpreted data to the user directly or through cyberspace. The passive nature of the tag and the RFID reader communication in cyberspace validates the

apt application of the presented passive sensor tag for fruit freshness detection. Table 2.3 summarizes the presented research's requirements, adapted technologies, and its advantages over the existing technologies.

Table 2.3 Summary of research requirements, adopted technologies, and its advantages over the existing technologies.

Features	Existing Technologies	Disadvantages of Existing Technologies	Adopted Approach in Our Device	Advantages of Our Device
Device	Resistor [11]-[15], Diode [16]-[18], FET[19][20], MNOS capacitor [21]	Resistor, diode and FET are active and are not impedance matched with RFID tag components. MNOS capacitor changes in work function to ethylene gas, hence, cannot be passively and wirelessly detected.	Parallel plate capacitor based device with sensing element as dielectric layer	Passive, less space required, simple, inexpensive and ease of integration with RFID tag antenna
Nanoparticle material with passive sensing	SnO ₂ (particle size 40 nm) [14][15][22], WO ₃ [23], TiO ₂ [24] (For other materials refer Table 2.1)	SnO ₂ (particle size 40 nm) and WO ₃ do not sense ethylene at room temperature and TiO ₂ material based sensor require magnetoelastic sensor readout system to sense at room temperature	SnO ₂ nanoparticles of 10 to 15 nm particle size and layer thickness of 500 nm to 1500 nm (low surface by volume ratio and very thin sensing layer for room temperature sensitivity)	Senses ethylene at room temperature
Fabrication techniques	Ceramic coating [28][31], Screen printing technique [32][32], CVD [30], Sol gel [33], Spin coating [34]	Requires high fabrication temperature on rigid substrates	Dip coating technique	Room temperature fabrication on flexible polyimide substrates
Measurement technique	Gas-chromatography [46], Laser technique [47], Chemiluminescence [48], IR-spectroscopy [49], Photoluminescent [50]	Complex, bulky, and expensive	Capacitively loaded to the feed of RFID triangular microstrip patch antenna	Eliminates ID circuit in tag and reduces size of antenna
Wireless sensing	Biosensor RFID system [58], Ethylene sensor integrated with RFID reader [59][60]	Requires active tags and operates using near field coupling at 13.56 MHz	Change in sensor capacitance changes the R_f and return loss of passive tag antenna which is wirelessly detected by a RFID reader	Integrated with passive RFID tags with far field wireless detection and operating at 915 MHz

CHAPTER 3

THEORY AND ANALYTICAL ANALYSIS

In this chapter, a detailed theoretical study of the ethylene sensor and microstrip patch antenna is given. Overview of antenna simulation and the basic principle of antenna integrated with the sensor are also given. The analytical analysis of methods of integration and experimental data points using antenna and lumped capacitors are also given.

3.1 Theoretical Study of Ethylene Sensor

The capacitive ethylene sensor is fabricated with SnO₂ nanoparticles as the sensing dielectric layer. Given below are the structural study and the reaction mechanism of SnO₂ nanoparticles and its role as a dielectric in the capacitive ethylene sensor.

3.1.1 SnO₂ Nanoparticles

In this work, the SnO₂ nanoparticles used is an n-type nanoparticle material of 10 to 15 nm particle size (Nyacol, pH = 10.5 to 12). It is a semiconductor material known for its good mechanical stability [66]. The material has only one stable state (no metastable state) and rutile in structural form. Figure 3.1 shows the tetrahedral rutile structure with $a=b \neq c$ and $\alpha=\beta=\gamma=90^\circ$ lattice structure. The unit cell has two tin atoms and four oxygen atoms with each tin atom placed in the center and the corners of the octahedron structure.

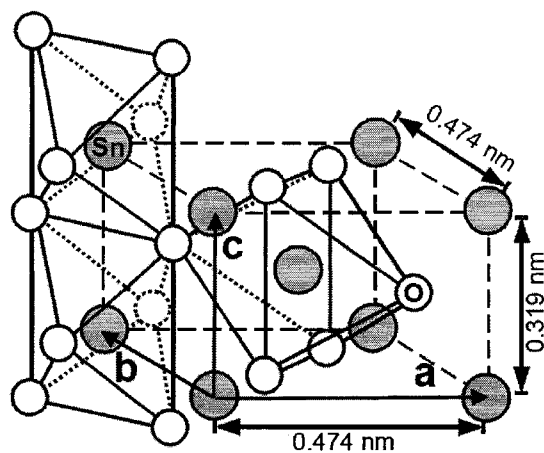


Figure 3.1 SnO₂ crystalline structure [66].

The nanocrystallites have various crystallographic planes. The crystallographic planes also play a role in the sensitivity of SnO₂ to various stimulants [63]. The various crystallographic structures are formed based on the fabrication process and the substrate on which it is coated [67]. An example of a crystallographic structure of tin dioxide using spray pyrolysis on a Si(SiO₂) substrate is shown in Figure 3.2.

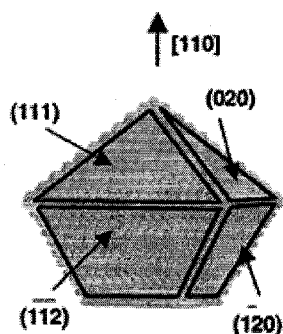


Figure 3.2 SnO₂ nanocrystallites deposited by spray pyrolysis [67].

Aqueous solution of SnCl₄·5H₂O (similar to sol-gel SnO₂ solution) is sprayed onto a 330⁰ to 535⁰ C heated Si(SiO₂) substrate. The resulting crystallographic structure

obtained is shown in Figure 3.2. The (111) plane is the most reactive plane and the (110) and (101) planes are the growth planes.

3.1.2 Reaction Mechanism

In this work, the SnO₂ nanoparticles are n-type material with electrons (e⁻) as the majority carriers. The SnO₂ nanoparticles (10 to 15 nm particle size) are suspended as milky-white sols with viscosity of 5 to 10 cps. Each individual SnO₂ nanoparticle consists of a conduction region and depletion region, as explained below.

In air, the oxygen (O₂) present in the air is adsorbed on the surface of SnO₂ and reacts with the electrons present in the conduction region. The reaction mechanism is given as follows [15][68].



As given by the Equations (3.1) and (3.2), an electron reacting with an O₂ molecule results in the formation of unstable O₂⁻ ions. The O₂⁻ ions further react with another electron to give two O⁻ ions. Thus, in a nanoparticle the loss of many electrons due to the above reaction with O₂ molecules causes a reduction in the n-type conductivity near the surface region, resulting in a build up of the depletion region. Hence, in air SnO₂ nanoparticles are expected to have a certain thickness depletion region which is comparatively more than the thickness of the conduction region for the case of thin film SnO₂ layer deposition. This phenomenon is schematically shown in Figure 3.3. The nanoparticle's outer region is depleted of electrons due to the formation of O⁻ ions. Thus, the conductivity of SnO₂ nanoparticles decreases in air. In [69], it is reported that the depletion width is 20 nm for a particle size of 30 nm in radius when kept in dry air at

room temperature using x-ray diffraction (XRD). This is approximately 33 % of the particle size. Relatively, using a linear scaling (due to the comparative nanoparticle size used in the previous work), our particle size (D_p) of 15 nm in diameter, has a depletion thickness of 5 nm in air (D_{da}).

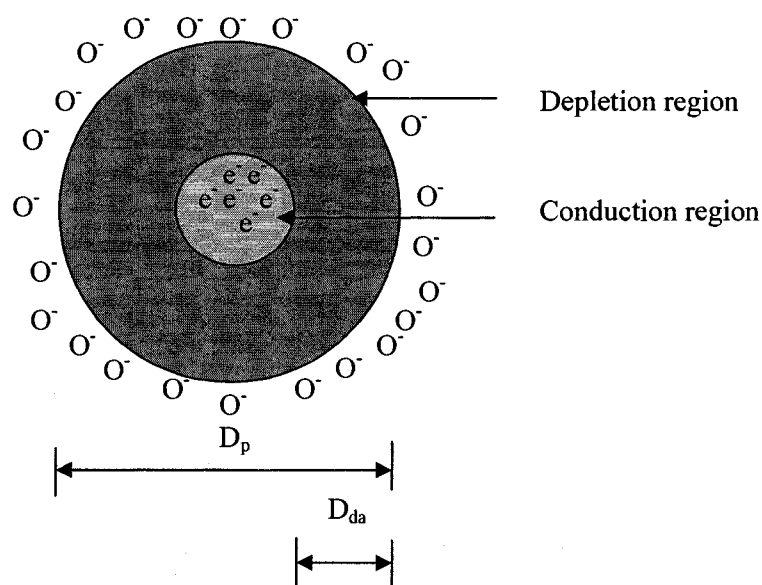
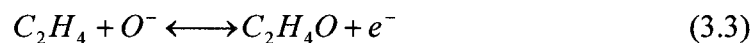


Figure 3.3 SnO₂ nanoparticle in air (before exposure to ethylene).

In the presence of a stimulant, (in our case it is ethylene gas- C_2H_4), the gas molecules react with the nanoparticles as given in the following equation [15].



The C_2H_4 gas molecule adsorbs the O^- ion, resulting in ethylene oxide gas (C_2H_4O) and an electron (e^-) which is replenished back to the SnO_2 nanoparticle. After this reaction, there will be a greater number of electrons in an SnO_2 nanoparticle thereby reducing the thickness of the depletion region and increasing the thickness of the conduction region. This phenomenon is illustrated in Figure 3.4. Thus, the overall

conductivity of the coated SnO₂ thin film increases in conductivity in the presence of ethylene gas. As given in [69], in the presence of a reducing gas like ethylene, the depletion thickness (D_{de}) reduces to a minimum of about 10 % of the particle size at a high temperature of 300⁰ C. In our case, the reaction takes place at room temperature, which means that the depletion region D_{de} might not reduce as much as it reduced in [69] due to the low reaction rate of an SnO₂ nanoparticle with oxygen at room temperature.

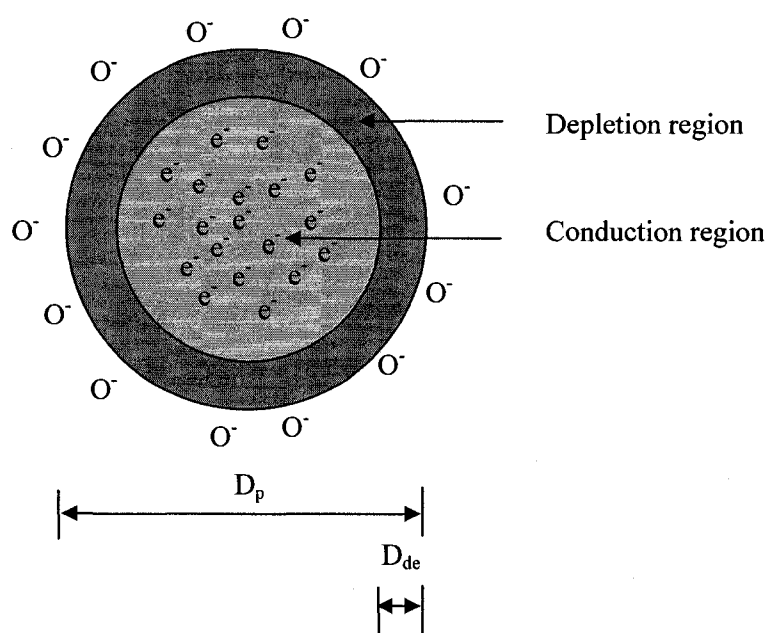


Figure 3.4 SnO₂ nanoparticle in ethylene (after exposure to ethylene).

The decrease and increase in conductivity of SnO₂ nanoparticles in air and ethylene respectively can also be explained in terms of the potential barrier [12]. In air, the depletion region is wide enough to have a high potential barrier between adjacent particles making it difficult for electrons to cross over. Thus, the conductivity of the material is low. In the presence of ethylene, the reduction of the potential barrier between

adjacent particles occurs due to the replenished electrons and results in more carrier conduction.

3.1.3 Capacitive Ethylene Sensor

In our case, the SnO_2 nanoparticles are used as the sensing dielectric layer in a capacitor model. The reaction of the capacitive sensor with ethylene gas takes place as given below. Figure 3.5 shows the capacitive sensor with SnO_2 nanoparticles as the dielectric layer and copper as the top and bottom plate. The presence of copper at the top and bottom restricts the diffusion of ethylene and the diffusion is only through the sides.

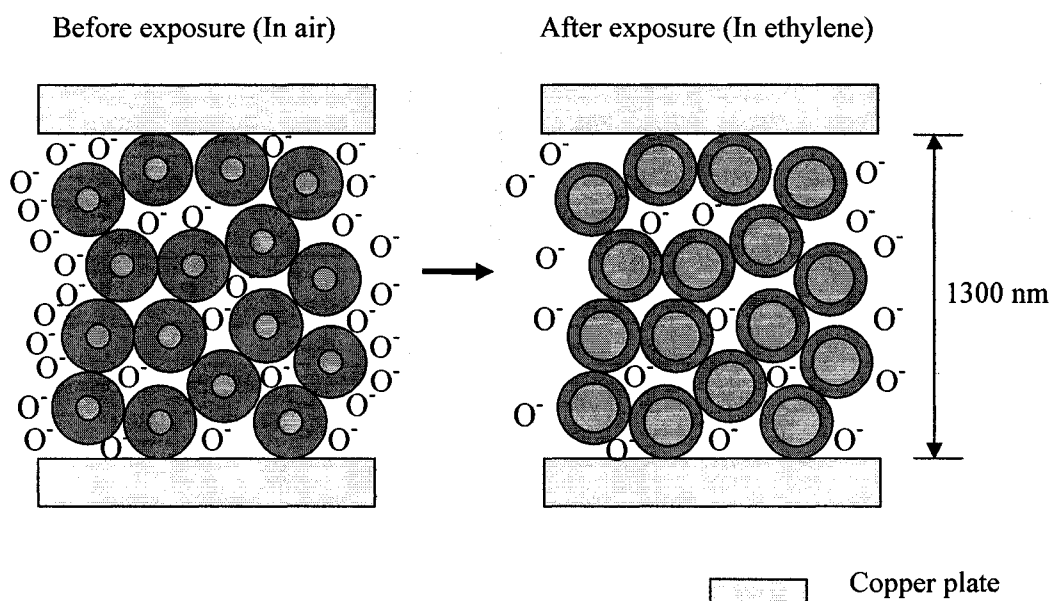


Figure 3.5 Cross section of the capacitive ethylene sensor model with SnO_2 nanoparticles as the dielectric.

As the nanoparticles are suspended in colloidal solution, after the deposition and drying, the nanoparticles can settle adjacent to each other or apart with interspatial gaps. These interspatial gaps are most likely filled with air or dry colloidal solution. The dry colloidal solution or air will act as a dielectric and can form stray capacitances between the nanoparticles. The capacitance value of these stray capacitors will be much smaller

than the capacitors formed between SnO₂ nanoparticles as the dielectric thickness is much higher and, therefore, can be neglected. In those cases where the SnO₂ nanoparticles are placed closer, but do not touch, these will have a higher stray capacitance value. As there is no change in the dielectric layer of the colloid or air, these capacitances can be taken as constants and will remain the same for samples in air and exposed to ethylene.

From Figure 3.5, let C_B be the initial capacitance of the capacitive sensor before exposure to ethylene gas.

$$C_B = \frac{\epsilon_0 \epsilon_r A_1}{d} \quad (3.4)$$

where,

ϵ_0 is the permittivity of free space (8.854×10^{-12} F/m)

ϵ_r is the dielectric constant of SnO₂ nanoparticles = 2.9 [70]

A_1 is the area of the dielectric i.e., sum of the total depletion region of the nanoparticles and the dielectric regions between nanoparticles before exposure to ethylene gas (in air).

d is the thickness of the dielectric region = 1300 nm.

Let C_A be the capacitance of the capacitive sensor after exposure to ethylene.

$$C_A = \frac{\epsilon_0 \epsilon_r A_2}{d} \quad (3.5)$$

where,

A_2 is the area of the dielectric i.e., sum of the total depletion region of the nanoparticles and the dielectric regions between nanoparticles after exposure to ethylene gas.

The dielectric thickness d remains the same after exposure to ethylene gas as the changes in the depletion thickness after exposure to ethylene happens inside the nanoparticles and the overall thickness of the nanoparticles still remain the same.

Practically, the diffusion of the ethylene gas for the fabricated samples is only on three sides as the fourth side is covered by the extended top copper plate which is grounded. Figure 3.6 shows the three-dimensional structure of the SnO_2 capacitor model.

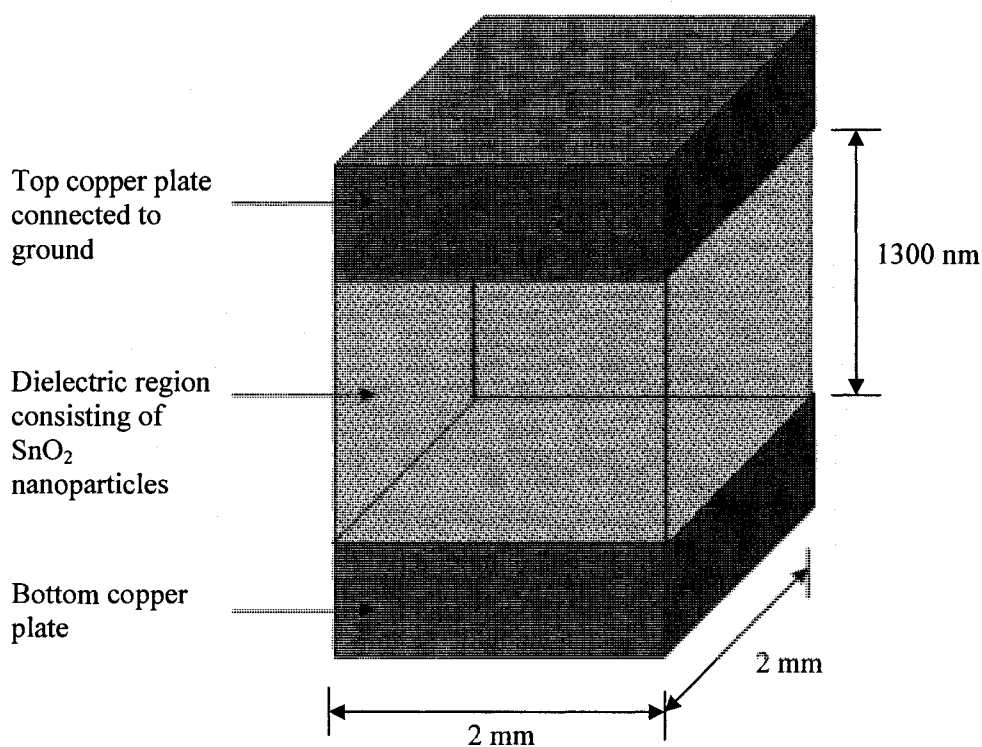


Figure 3.6 Three-dimensional structure of the SnO_2 capacitor model.

For the calculation of A_1 and A_2 , let us consider Figure 3.7. It shows the top view of a portion of the dielectric region containing the SnO_2 nanoparticles with depletion region and conduction region as seen through the top copper plate before and after exposure to ethylene gas. Let us assume that the particles are closely packed next to each

other as shown in Figure 3.7, with the nanoparticles of the bottom layer aligning vertically below the top layer of nanoparticles.

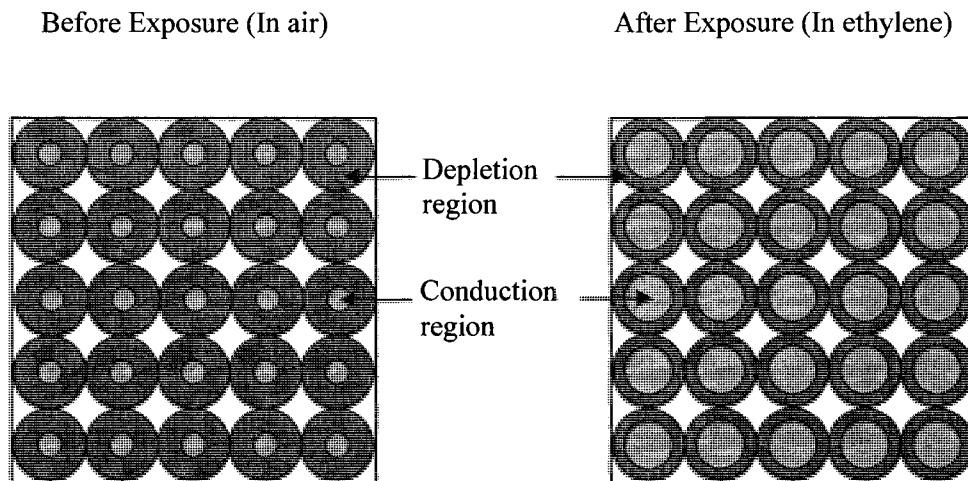


Figure 3.7 Top view of dielectric region with SnO₂ nanoparticles seen through the top copper plate before and after exposure to ethylene gas.

Before exposure to ethylene gas, the sample is left in air overnight so that the maximum diffusion of oxygen occurs and a stable depletion width is reached. The plate area A_I consists of the sum of the plate area covering the depletion region of individual nanoparticles and the dielectric regions between nanoparticles. The length and width of the copper plate deposited is 2 mm x 2 mm and the area of an individual nanoparticle was calculated as $1.766 \times 10^{-4} \mu\text{m}^2$ (particle size = 15 nm in diameter). Now, the number of nanoparticles (n) that can fit in a copper plate area (A) of 2 mm x 2 mm was calculated to be 2.26×10^{10} nanoparticles.

The dielectric area A_I is the sum of total depletion region of individual nanoparticles and the dielectric regions between nanoparticles. For the calculation of total area of the depletion region, the depletion region of an individual nanoparticle has to be

calculated which is then multiplied by the total number of nanoparticles. The area of only the depletion region of an individual SnO₂ nanoparticle (A_{da}) was calculated as,

$$A_{da} = A - A_{ca} \quad (3.6)$$

where, A_{ca} is the area of the conduction region. In air, the depletion region thickness is about 5 nm and the conduction thickness is 5 nm. Using Equation (3.6), A_{da} was calculated as $1.57 \times 10^{-4} \mu\text{m}^2$ with A_{ca} as $1.96 \times 10^{-5} \mu\text{m}^2$. Therefore, A_I was calculated as $2.79 \times 10^{-6} \text{mm}^2$ using Equation (3.7).

$$A_I = nA_{da} \quad (3.7)$$

Substituting the value of A_I in Equation (3.4), we get $C_B = 55.1 \text{ pF}$.

For the calculation of plate area after exposure A_2 , we need to calculate the length of diffusion (L) of the ethylene gas through the dielectric region to know the extent of diffusion area of ethylene gas. As given in [71], for pore radius from 2 nm to 20 nm formed by nanoparticles, the diffusion of gas into the nanoparticles is through Knudsen diffusion (D_k) which is given by,

$$D_k = \frac{2}{3} r \times \sqrt{\frac{8R_g T}{\pi M}} \quad (3.8)$$

where,

r is the pore radius (3.1 nm in our case with densely packed nanoparticles)

R_g is universal gas constant = $8.314 \times 10^7 \text{ g cm}^2 \text{ s}^{-2} \text{ mol}^{-1} \text{ K}^{-1}$,

T is temperature in Kelvin, and

M is molecular weight of ethylene gas in g mol^{-1} .

From Equation (3.8), D_k was calculated as $0.009 \text{ cm}^2 \text{ s}^{-1}$. The diffusion length (L) is give as,

$$L = \sqrt{tD_k} \quad (3.9)$$

Where, t is the time of exposure of the sample to ethylene gas (in our case, it is about 5 min). The value of L was calculated as 17.17 mm, which is much higher than the length and width of 2 mm x 2mm. Hence, we can conclude that the diffusion of ethylene gas into the dielectric region is complete diffusion.

For calculating the plate area after exposure to ethylene (A_2), we need to calculate the area of the depletion region of an individual nanoparticle after exposure to ethylene (A_{de}). If we assume that the conduction thickness increases to 6.6 nm from 5 nm after exposure to ethylene, then from Equation (3.10) given below, the area of the conduction region of an individual nanoparticle (A_{ce}) is $3.42 \times 10^{-17} \text{ m}^2$ and A_{de} is $1.42 \times 10^{-16} \text{ m}^2$.

$$A_{de} = A - A_{ce} \quad (3.10)$$

Now the total area after exposure to ethylene (A_2) is given as,

$$A_2 = nA_{de} \quad (3.11)$$

The value of A_2 was calculated to be $2.53 \times 10^{-6} \text{ m}^2$ and, substituting this value in Equation (3.5), we get $C_A = 50.01 \text{ pF}$. Thus, after exposure to ethylene the capacitance of the sensor reduces by about 5 pF, which is similar to the reduction in capacitance obtained experimentally.

3.2 Antenna Theory

The antenna is a triangular microstrip patch antenna fabricated on a flexible polyimide substrate [72]. The triangular microstrip patch antenna is a compact antenna with omnidirectional radiation pattern.

3.2.1 Theory and Simulation

An antenna is a device used for capturing and radiating electromagnetic waves in the receiving and transmitting mode of operation [73]. Some of the key parameters of an antenna are its substrate, skin depth, resonant frequency, voltage standing wave ratio (VSWR), gain, impedance, and backscattered antenna signal.

3.2.1.1 Substrate

The microstrip antennas used for RFID tags consist of a radiating top plane and a ground plane. The dielectric is usually the substrate and in our case it is flexible polyimide sheet. The antenna top and ground plane is made of copper and the thicknesses of the layers are given in Figure 3.8.

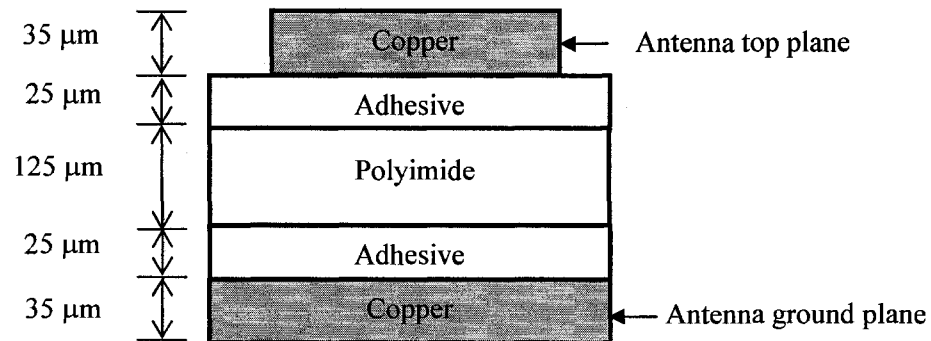


Figure 3.8 Cross section of antenna substrate.

All antenna simulations were performed using Ansoft Designer [74]. Ansoft Designer is a two-dimensional electromagnetic analysis tool which employs Method of Moments for the integral equation analysis in the spectral domain. The compact triangular microstrip antenna was designed and fabricated on a flexible Kapton sheet similar to the compact Half-Sierpinski microstrip antenna mentioned in [75] for RFID applications. The slot in the ground plane aids in increasing the gain of the antenna.

3.2.1.2 Skin Depth

The skin effect of a microstrip antenna is defined as the tendency of the alternating current supplied to the antenna to distribute itself within the conducting surface at a specified depth near the surface. The current density at this depth is greater than at the core of the conductor. This depth is defined as the skin depth (δ) of an antenna. This parameter is dependent on the material of the conducting surface and the frequency of operation as shown in Equation (3.12).

$$\delta = \sqrt{\frac{2\rho}{2\pi\mu_0\mu_r}} \quad (3.12)$$

where,

ρ is the bulk resistivity of the conducting copper material

f is the frequency in Hz

μ_0 is the permeability constant in H/m ($4\pi \times 10^{-7}$)

μ_r is the relative permeability.

The skin depth for 915 MHz signal passed on a copper sheet is 2.15 μm . This number indicate that the required thickness of the copper conducting plate of the antenna is 2.15 μm . Thickness of copper greater than this is a waste of copper material and less than the prescribed value results in a huge loss in the propagation of the current density in the antenna surface.

3.2.1.3 Resonant Frequency

Resonant frequency is defined as the frequency of the antenna at which the antenna's capacitive and inductive reactances cancel each other. However, practically all antennas contain a small amount of capacitance and inductance. The triangular microstrip

patch antenna consists of a triangular copper plate with inset feed for fine tuning to resonate at 915 MHz, as shown in Figure 3.9.

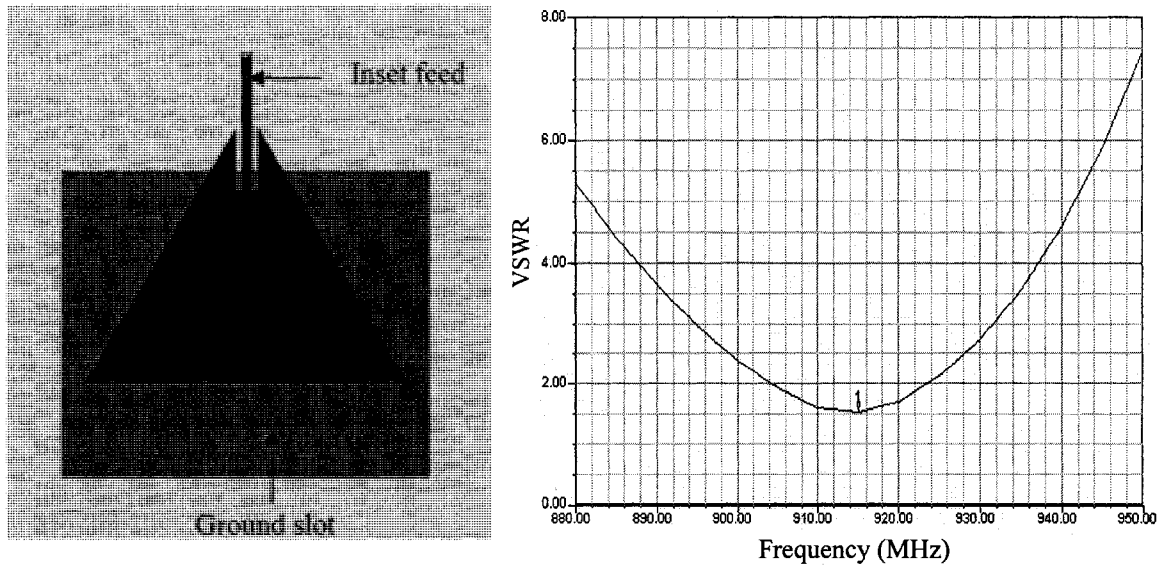


Figure 3.9 Simulation model of triangular microstrip patch antenna with VSWR = 1.51 at $R_f = 915$ MHz.

The resonant frequency of the antenna is determined by simulating the antenna for a wide sweep of frequencies. Hence, the resonant frequency is the frequency of the antenna at which the antenna performs at its best. All antennas have a range of operating frequencies around its resonant frequency at which the antenna performs well. In the case of RFID tag antennas, the bandwidth is defined as the range of frequencies for which the voltage standing wave ratio (VSWR) is less than 2. From Figure 3.9, the bandwidth of the antenna was observed as 20 MHz.

3.2.1.4 VSWR

Voltage standing wave ratio (VSWR) is the measure of the antenna capability at its resonant frequency. VSWR (S) is mathematically expressed in terms of the voltage reflection coefficient (τ),

$$S = \frac{1 + |\tau|}{1 - |\tau|} \quad (3.13)$$

The voltage reflection coefficient is mathematically represented as the ratio of the amplitude of the reflected voltage wave to the amplitude of the incident voltage wave at the load. Ideally, a VSWR=1 denotes that all the incident electromagnetic waves are absorbed and a VSWR of ∞ denotes that all the incident electromagnetic waves are reflected. Figure 3.9 shows the VSWR of the triangular microstrip patch antenna resonating at 915 MHz as 1.51 and a bandwidth of 22 MHz (902 MHz to 924 MHz) for which the VSWR is less than 2. The requirement for RFID tag antennas is that the VSWR should be less than 2 which implies that 88.9 percent of the signal is received.

3.2.1.5 Gain

Another important antenna parameter is the gain of the antenna. The higher the gain of an antenna, the greater is the reading distance. Mathematically, the gain ($G(k)$) of an antenna is defined as

$$G(k) = \frac{4\pi U(k)}{P_A} \quad (3.14)$$

where, $U(k)$ is the radiation intensity of the antenna and P_A is the time average power absorbed by the antenna. The RFID tag antenna gain requirement is greater than 0 dB or 2.15 dBi. “dBi” is the gain of the RFID antenna with reference to an isotropic antenna

(antenna which radiates in all directions). The gain of the triangular patch antenna as shown in Figure 3.10 is 1.21 dB or 3.36 dBi.

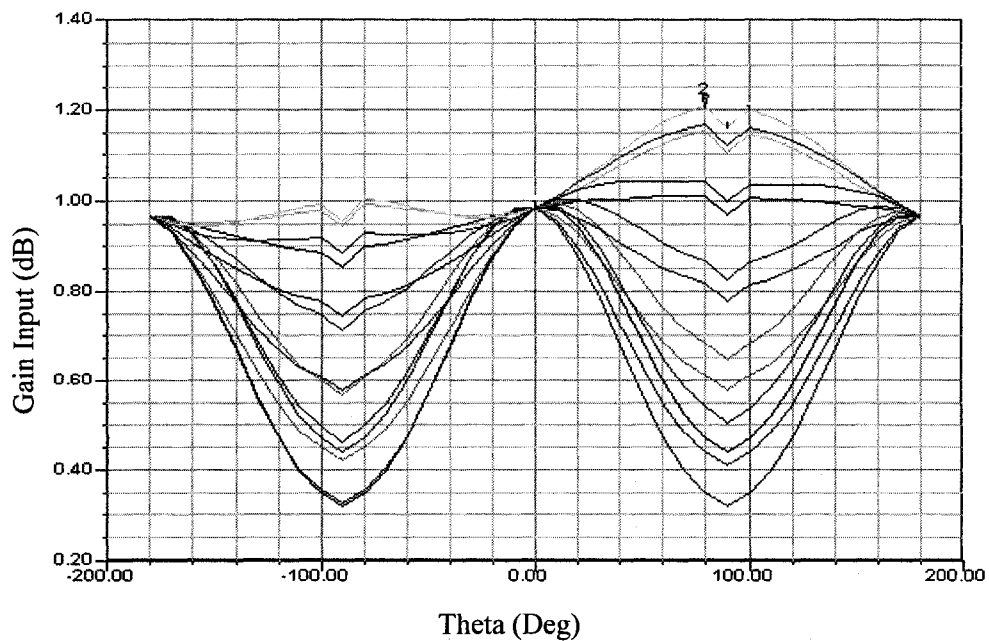


Figure 3.10 Gain of triangular microstrip patch antenna.

3.2.1.6 Impedance

Another key parameter is the impedance of an antenna. When a microstrip patch antenna is connected to other circuitry, transmission line or cable for measurement purposes, the antenna has to be impedance matched with the other component. When there is an impedance mismatch, reflections occur at the point of mismatch increasing the antenna VSWR. The antenna impedance is represented as Z_A and consists of a real part R_A and an imaginary part X_A . Ideally, R_A should be 50Ω and X_A should be zero. Figure 3.11 shows the impedance of the antenna with $R_A = 31.91$ and $X_A = 5.04$.

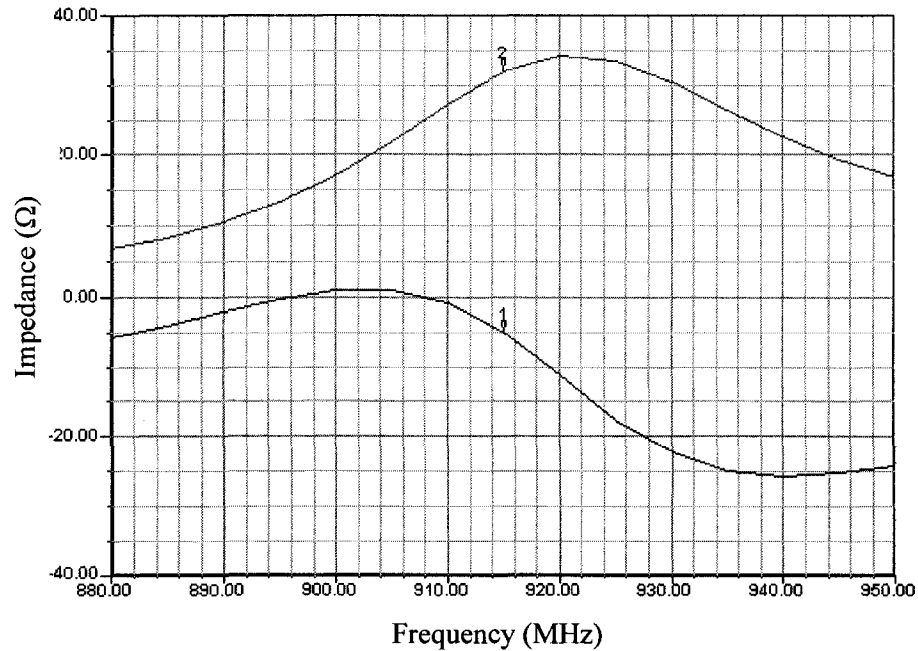


Figure 3.11 Impedance of triangular microstrip patch antenna.

3.2.1.7 Backscattered Antenna Signal

The triangular microstrip patch antenna is a passive antenna resonating at 915 MHz; hence the principle of operation of the antenna is by absorbing the electromagnetic waves impinging on the antenna conducting surface and reflecting back the signal. This is called the backscattered antenna signal. This is an important parameter of the antenna as the performance of the antenna to effectively backscatter the signal defines the mode at which the antenna is operating [76]. The two modes of operation are structural mode reflection and antenna mode reflection. Structural mode reflection occurs when the antenna is left open and the backscattered signal amplitude signifies the backscattered power is solely due to the structure of the antenna. The backscattered signal is low for this case. Antenna mode reflection occurs when the antenna is connected to a load and the backscattered signal is due to the mismatch between the impedance of the antenna

and the load. When an antenna is shorted, it is purely reflective and hence the backscattered signal is maximum, and when left open the backscattered signal is minimum and the antenna is purely absorbing. By measuring the backscattered signal amplitude, the nature of the load connected to the antenna can be identified wirelessly.

3.3 Integration of Ethylene Sensor with RFID Tag Antenna

Two methods of integration of the sensor with the antenna were tested. The first method of integration is the load integration of sensor to antenna where the sensor is connected as a load to the antenna. The second method of integration is the direct integration of sensor to the antenna.

3.3.1 Load Integration to Antenna

The sensor is connected as a load to the antenna through a transmission line as shown in Figure 3.12. It can be seen that the sensor is in series with the antenna.

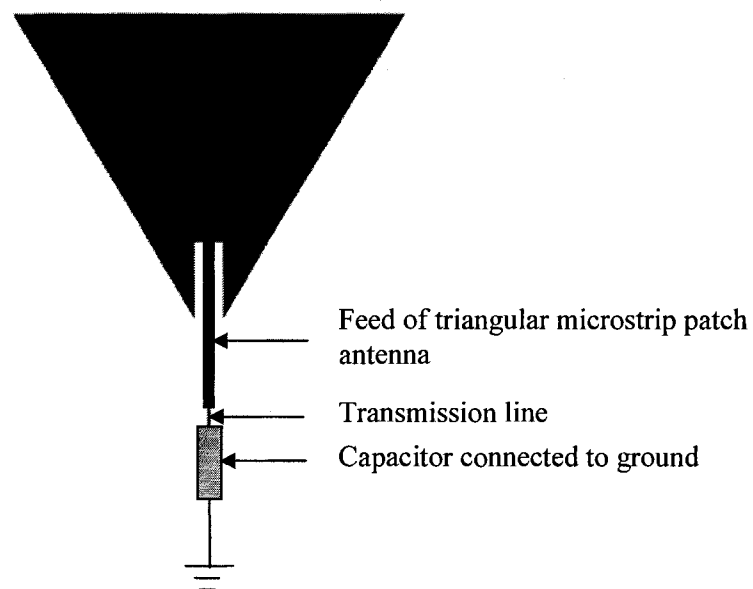


Figure 3.12 Sensor connected as a load to antenna.

The ethylene sensor is a capacitor based sensor operating in the range of 0 to 10 pF of capacitance. Capacitance greater than 10 pF pushes the antenna to resonate at much lower frequency than its resonant frequency causing the VSWR to increase rapidly and resonate with high noise. Since the RFID tag is passive, a continuous sinusoidal signal is transmitted and the signal backscattered from the tag is measured for changes in amplitude. When the value of capacitance changes, the load to the antenna changes which varies the amplitude of the reflected signal.

3.3.1.1 Analytical Analysis

For analytical analysis, capacitance from 1 to 10 pF is used. The impedance of the capacitance (Z_C), acting as the load to the antenna is given by,

$$Z_C = \frac{1}{2\pi f C} \quad (3.15)$$

where, f is the 915 MHz resonant frequency and C is the capacitance of the load capacitor. The impedance of the antenna obtained from simulation is $31.91 + j5.04$. Hence, the impedance of the antenna (Z_A) is 32.31 . The amount of reflection due to the load impedance mismatch to the antenna is given by reflection coefficient (τ).

$$\tau = \frac{Z_C - Z_A}{Z_C + Z_A} \quad (3.16)$$

The VSWR of the antenna (S) is then calculated using Equation (3.13). The reflected power (P_A) in terms of percentage value, received at the reader, for the specific VSWR of the antenna is obtained from the chart given in [77]. The change in received power P_R at the reader antenna is calculated as,

$$P_R = P_A P_t \quad (3.17)$$

The power of the reader antenna P_t is measured as,

$$P_t = \frac{V_R^2}{Z} \quad (3.18)$$

where, V_R is the voltage received by the reader antenna (experimentally measured as 200 mV) and Z is the impedance of the reader system which is approximated to be 50Ω .

The change in amplitude of the backscattered voltage (V_B) is given by,

$$V_B = \sqrt{P_R Z} \quad (3.19)$$

Figure 3.13, shows the graph obtained when the backscattered voltage is plotted for the change in capacitance.

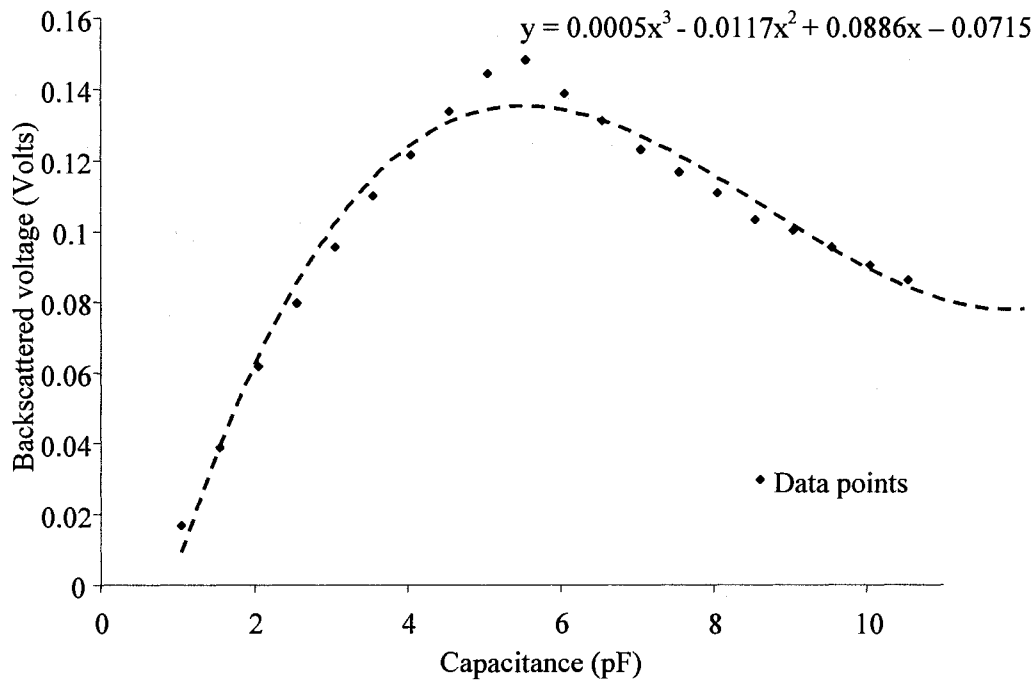


Figure 3.13 Theoretical result for backscattered voltage when sensor capacitance is connected as a load to antenna.

The curve shows a polynomial distribution. This is due to the impedance matching occurring between the sensor capacitance and the antenna at 5 pF. From the

results obtained, it is evident that integrating the sensor capacitor as a load will result in misreading of data by the reader as the same backscattered voltage is obtained for 3.3 pF and 4.7 pF. To perform further theoretical and initial experimental analysis, in place of the capacitive sensor lumped capacitor components in the range of 1 to 10 pF were used. In this experiment, the lumped capacitor was connected in series with the antenna through a transmission line. The backscattered voltage was measured using the custom built RFID reader. A detailed description of the experimental setup is given in Chapter 5.

3.3.2 Direct Integration with Antenna

In this method, the capacitive sensor is directly integrated with the antenna. The parallel integration of the sensor and the antenna was tested with lumped capacitors soldered to the antenna and grounded. This type of integration, as explained in [65], is known as a capacitively loaded antenna. Figure 3.14 shows the six different integration configurations that were explored to determine the best location for integration. The best location for integration of the sensor should be the place where even a small change in capacitance of the sensor should cause a maximum change in the antenna characteristics. For the integration of the sensor with the triangular patch antenna, lumped capacitors were used at different places to detect the maximum change in the antenna with a minimum change in the sensor. Two capacitors of 3.3 pF and 4.7 pF were tried and the output resonant frequency shift was observed. For configuration 1 and 2, the capacitor is integrated to the feed of the antenna, yet configuration 2 performs better as the capacitor is integrated to the end of the feed rather than at the middle of the feed, as is the case for configuration 1.

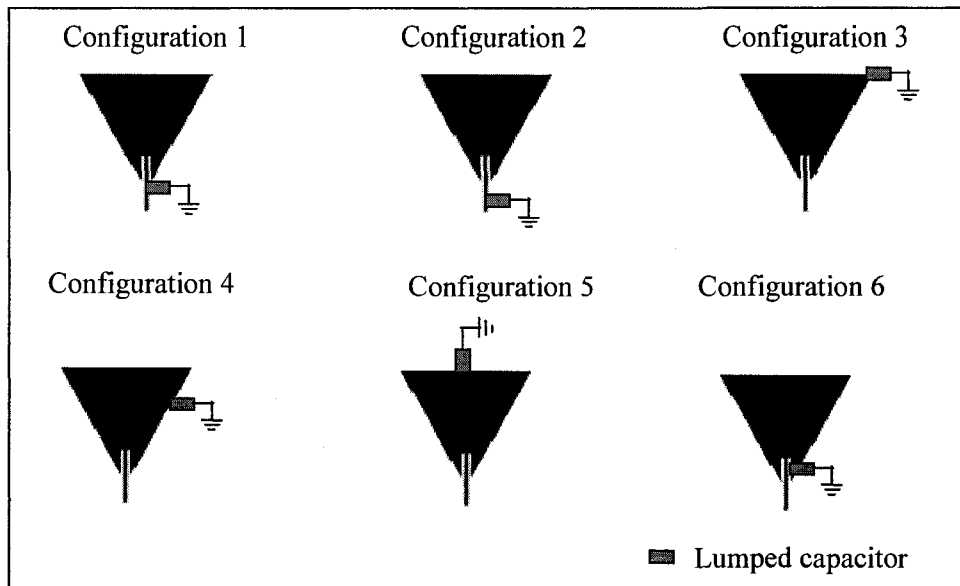


Figure 3.14 Different configurations for the direct integration of the sensor with antenna.

Figure 3.15 shows the results obtained for all the above shown configurations. Both experimental results using lumped capacitor and simulation results show a similar trend for the shift in frequency.

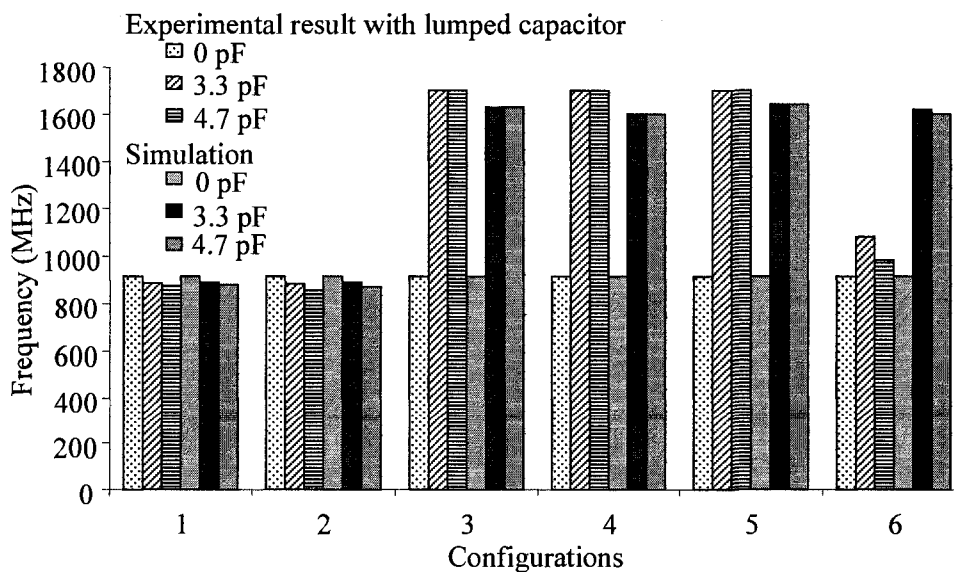


Figure 3.15 Shift in frequency for change in capacitance for six different configurations of sensor integrated with the antenna.

From the figure, we can see that configuration 2, with the sensor integrated at the feed end of the antenna, proved to be the best integration location with a consistent shift in frequency. The antenna characteristics, i.e. shift in frequency, is consistent for the capacitor integrated at the feed end of the antenna because the length and thickness of the feed plays an important role in tuning the impedance and VSWR of the antenna [72]. Also, the radiation pattern of the antenna is immensely affected by even a small change in the feed of the antenna. Hence, integrating the capacitive sensor at the feed results in maximum disturbance/change to the antenna characteristics.

The solid line in Figure 3.16 shows the change in backscattered voltage for the capacitor directly integrated with the antenna. The value of the lumped capacitor was changed from 0 to 10 pF. In Figure 3.16, the result is also compared with the capacitor connected in series with the antenna which is indicated by dotted lines.

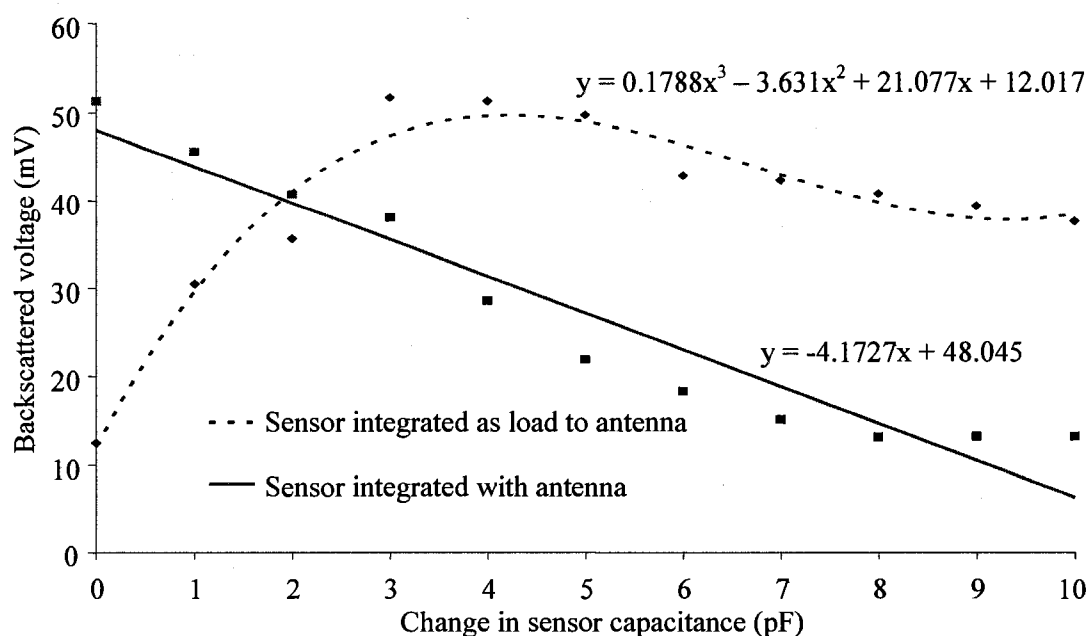


Figure 3.16 Comparison of methods of sensor integrated with antenna.

The experimental result with lumped capacitors connected as a load to the antenna through a transmission line also shows a polynomial distribution which confirms the analytical analysis for the same. The difference in the amplitude of the backscattered voltage signal is much higher than for the theoretical study because experimentally the signal is damped when traveling through air. Thus, the plot clearly shows that the direct integration of the sensor with the antenna has a linear characteristic, which is desirable for sensing application.

3.3.2.1 Theory

When a microstrip antenna is integrated with a pF capacitor, a shift in its resonant frequency is observed. Rowell, et al. in [78] shows an example of a capacitor loaded planar inverted-F antenna (PIFA) reducing in resonant frequency when capacitance of 1 to 5 pF was loaded. When the capacitance was increased, the resonant frequency decreased. The shifting of R_f also results in an increase in VSWR at the resonant frequencies. This is attributed to the straining of the antenna beyond its designed resonant frequency. Hence, only a few pF of capacitance can be loaded to the antenna. The shift in resonant frequency is explained as follows. A microstrip patch antenna is a parallel RLC circuit at resonant frequency (f) which is given as,

$$f = \frac{1}{2\pi\sqrt{LC_T}} \quad (3.20)$$

where,

L is the inductance

C_T is the capacitance.

When a capacitor (C_S) is integrated in parallel with the antenna, the total capacitance increases as $C_A + C_S$. Now Equation (3.20) becomes

$$f = \frac{1}{2\pi\sqrt{L(C_T + C_S)}} \quad (3.21)$$

The increase in capacitance in the denominator reduces the resonant frequency. Thus, when a capacitor is loaded to an antenna, its resonant frequency decreases.

The capacitor loaded to an antenna also helps in reducing the size of the antenna. This key advantage can be explained in the following manner. Antennas reduce in size when designed for higher resonating frequencies. At first the antenna to which a capacitor is to be loaded is designed at a higher frequency such that when a capacitor is added, its resonant frequency reduces to its designed resonant frequency. The initial design of the antenna to higher frequency reduces the size of the antenna. Thus, applications pertaining to antenna size reduction in mobile phones use this principle.

3.3.2.2 Simulations

Applying the same principle to a triangular patch microstrip antenna, simulations were performed to observe the change in R_f . A triangular microstrip patch antenna resonating at 915 MHz was created in an electromagnetic plane, as shown in [72], using Ansoft Designer (Figure 3.17).

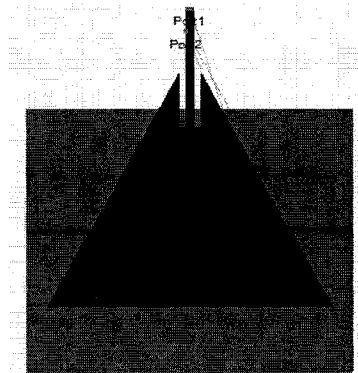


Figure 3.17 915 MHz triangular patch antenna designed in the EM plane.

Two ports were created, port 1 for the input signal and port 2 for the connection of the capacitive sensor. The EM plane triangular patch antenna was then transferred to the circuit level by creating a model for the antenna (Figure 3.18). The model is indicated as a box with two ports. Port 1 serves as the microwave input port for supplying 915 MHz continuous sinusoidal input. Port 1 is matched to 50Ω , as the input signal from signal generator practically is 50Ω . Port 2 is matched to 28.62Ω , as it is an open port in the EM plane and was measured as 28.62Ω .

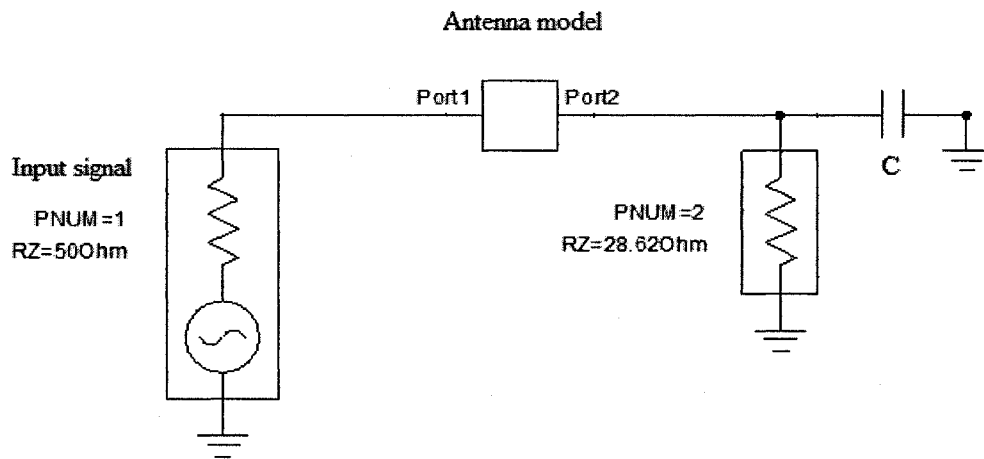


Figure 3.18 Antenna integrated with capacitive sensor in the circuit level.

The same impedance matching has to be followed in the circuit level to match the antenna R_f and VSWR in the EM level as well as in circuit level. The capacitor C was varied from 0 to 10 pF. Port 1 also serves as the microwave input port for supplying 915 MHz continuous sinusoidal input. Figure 3.19 shows the simulation result for change in R_f when the capacitance was changed.

Experimentally, lumped capacitors representing the capacitive sensors were soldered to the feed of the antenna and the change in frequency was measured using a

network analyzer. A detailed explanation for the experimental set-up and measuring techniques are given in section 5.1. Figure 3.19, shows a well matched result for change in frequency to change in capacitance.

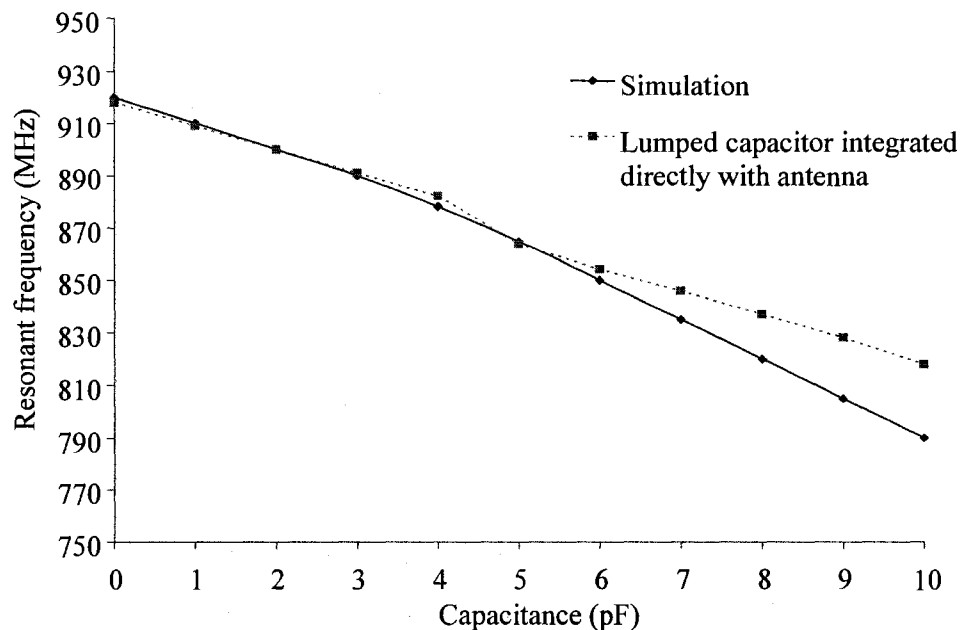


Figure 3.19 Shift in R_f when capacitive sensor is directly integrated with the antenna.

The change in R_f to the change in capacitance is linear and is similar to the linear R_f shift observed in [79]. The discrepancy in R_f after 6 pF of capacitance is due to the reflections in the experimental set-up when the antenna is pushed to operate further from its R_f of 915 MHz.

CHAPTER 4

FABRICATION AND CHARACTERIZATION

This chapter consists of three sections. The first section presents the fabrication of stand alone ethylene sensors on polyimide substrates. The section also presents the characterization (thickness and roughness measurements) of the sensing SnO₂ material and cellulose acetate insulating layer. The second section presents the fabrication of the triangular microstrip patch antenna and the third section presents the fabrication steps involved in the integration of the ethylene sensor with the microstrip patch antenna.

4.1 Fabrication of Ethylene Sensor

The ethylene sensor is a parallel capacitor plate model. Hence, it has a bottom copper plate and top copper plate with the sensing SnO₂ layer as the dielectric. The substrate used for the fabrication is a flexible polyimide substrate (Pyrallux FR copper-clad laminate, DuPont). The substrate has 35 μm thick copper on both sides of the polyimide sheet. Three solutions made up of SnO₂ nanoparticles, cellulose acetate, and poly(diallyldimethylammonium chloride) (PDDA) were used for the capacitive sensor fabrication.

4.1.1 Solution Preparation

The SnO₂ nanoparticle solution which is used as the sensing layer, is a colloidal solution purchased from Nyacol (Colloidal tin dioxide with 12 to 15 nm particle size and counter ion concentration of 0.23% NH₃). The solution is mixed with 50% de-ionized (DI) water. The insulating layer of cellulose acetate, which is used to prevent shorting between the capacitor plates was the first layer of deposition on the bottom copper plate. 100 ml of cellulose acetate is prepared by mixing 2.5 mg of cellulose acetate powder (Fluka, Cellulose acetate with 40% acetyl group as degree of substitution, MW 29000) mixed in 60 ml of tetrahydrofuron and 40 ml of acetone.

A 40 nm thick layer of PDDA is used as an adhesion promoter and is coated on top of the cellulose acetate before coating the SnO₂ sensing layer for better adhesion of SnO₂ to the cellulose acetate. The PDDA coating enhances better adhesion based on the principle of layer by layer (LbL) technique given in [80]. PDDA are polycationic particles i.e., they are positively charged with an isoelectric point value of 12. The isoelectric point of a material is the pH at which the particle has no net electric charge. As cellulose acetate is polyanionic, PDDA dip coated on cellulose acetate has good adhesion. SnO₂ being polycationic can then be coated on the single layer of PDDA. 100 ml of PDDA solution is prepared by using 1 ml of low molecular weight PDDA solution (Sigma-Aldrich; 100,000 < MW < 200,000 g/mole, 20 wt% solution in water, repeat unit molecular weight of 161 g/mole) mixed in 100 ml of DI water.

4.1.2 Fabrication Steps and Techniques

A copper clad polyimide sheet was used as the substrate for the standalone sensor fabrication. Figure 4.1 shows the fabrication steps for the ethylene sensor.

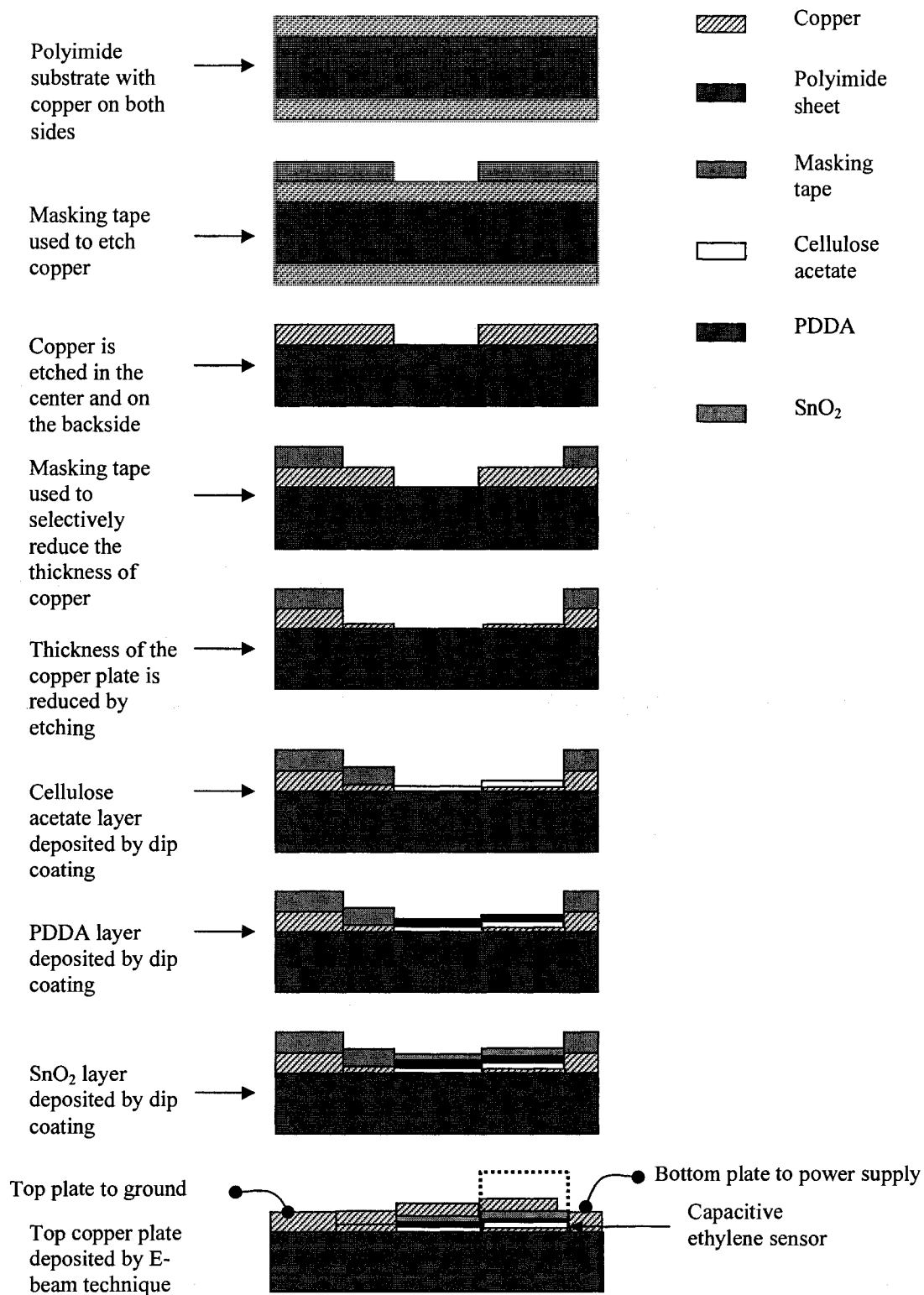


Figure 4.1 Fabrication steps for ethylene sensor on polyimide substrate.

As the thickness of the copper is 35 μm , dip coating the layers of thicknesses in the nanoscale (1200 nm for cellulose acetate, 40 nm for PDDA, and 1300 nm for SnO_2) would not provide proper step coverage. Without proper step coverage, while depositing the top copper layer, the plates will become shorted. Hence, the thickness of the top copper layer was reduced to ca 5.5 μm by etching using ferric chloride solution. Care must be taken to maintain the thickness of copper above the skin depth of 2.15 μm for 915 MHz frequency signals. The substrate was dipped in a solution of ferric chloride maintained at 35⁰ C for about 5 min. The solution was continuously agitated using a bubbler. The places where etching is not required was covered by masking tape stuck on the copper. A thin layer of 1200 nm of cellulose acetate is deposited by the dip coating technique. The sample is immersed in a Petri dish of the solution and quickly pulled out in the vertical direction. The layer is dried at room temperature for about 15 min. The next layer coated was PDDA of thickness 40 nm using the dip coating method and dried at room temperature. The SnO_2 layer of thickness 1300 nm was then coated using the same method and dried at room temperature for about 8 hours. The top copper layer is coated using electron-beam deposition. Figure 4.2 shows the structure of the capacitive ethylene sensor.

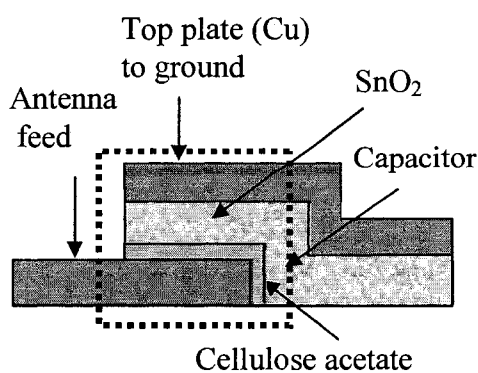


Figure 4.2 Structure of capacitive ethylene sensor.

A shadow mask was used for coating purposes and a thickness of 300 nm of copper was deposited using the e-beam technique. Crocodile clips connected to insulated copper wires were used for the connections to the top and bottom plates. Figure 4.3 shows the SnO₂ capacitive sensor fabricated on a flexible polyimide sheet.



Figure 4.3 Fabricated capacitive ethylene sensor on polyimide substrate.

4.1.3 Characterization of Deposited Layers

The thickness and roughness of copper and deposited cellulose acetate, PDDA, and SnO₂ were studied using a Tencor Profilometer. The characterization of the deposited layers was studied using a quartz crystal microbalance (QCM). For QCM measurement of thickness, the thickness of the layer to be measured is measured using step height method. In this method, the QCM sensor scans the measuring layer and also the adjacent layer at a lower elevation. Thus a step scan is obtained. As there is roughness in the coated layer, the layer thickness measurement is performed by comparing an averaged area in the measuring layer and an averaged area in the adjacent layer at a lower elevation. The initial thickness of the copper layer was 35 μm and, after reducing the thickness by etching, the thickness of the copper layer was 5.5 μm (Figure 4.4).

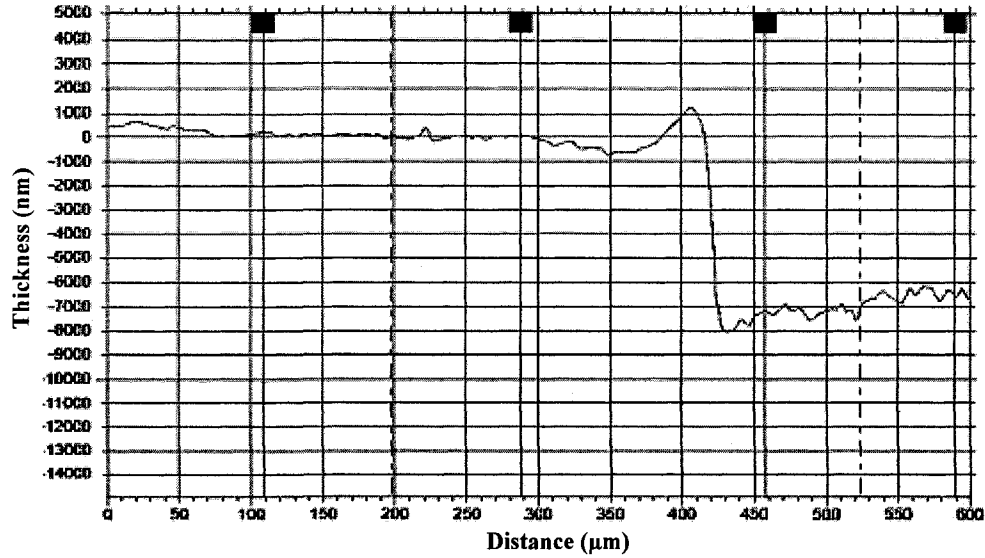


Figure 4.4 Tencor measurement of copper thickness = 6934 nm, measured after reducing the thickness using etching.

The roughness of the etched copper surface was $0.63 \mu\text{m}$ as shown in Figure 4.5. The spike in the roughness measurement seen at the end is due to the scratches present in the copper sheet. The initial roughness of the copper surface is high which is then mostly smoothed out using the cellulose acetate insulating layer.

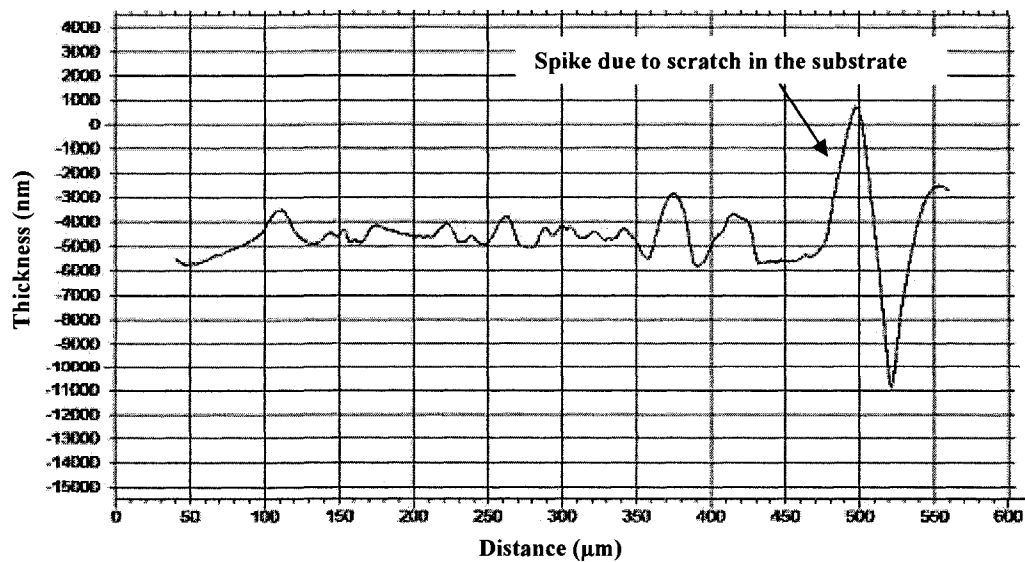


Figure 4.5 Roughness of the etched copper surface = 632 nm.

Figure 4.6 shows the roughness of the copper surface after coating with cellulose acetate to a thickness of 1200 nm. The roughness reduced to 131 nm. Thus, the layer of cellulose acetate not only works as an insulator, but also helps in planarizing the copper surface by filling the scratches. The spike in the roughness measurement seen at the end of the scan is due to the scratches present in the copper sheet itself which has been partially (nearly 50%) planarized out by the cellulose acetate coating. The thickness of the cellulose acetate layer coated using the dip coating method was 1200 nm, as shown in Figure 4.7.

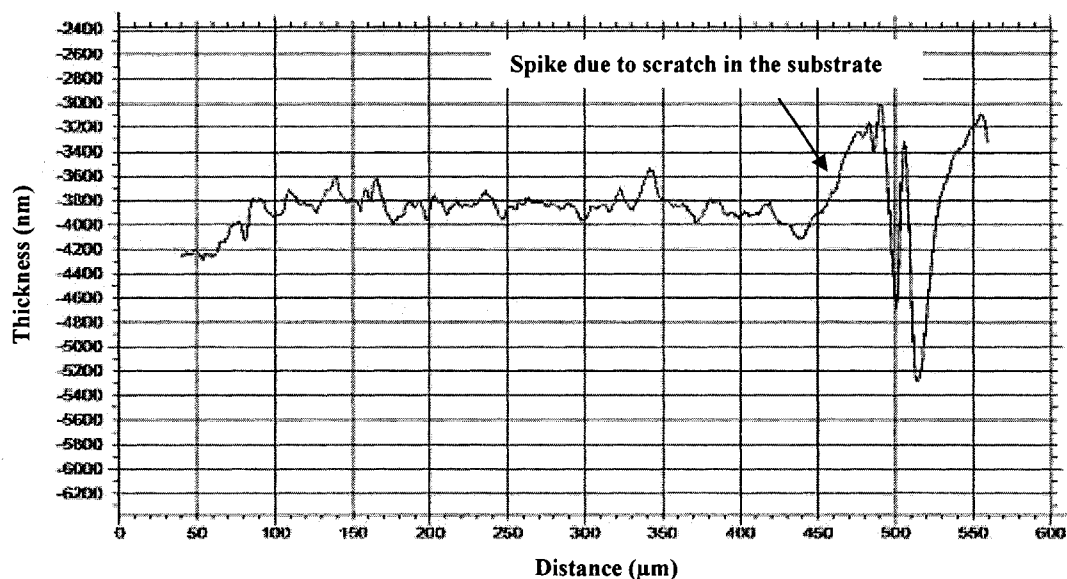


Figure 4.6 Roughness of cellulose acetate layer coated on copper = 131 nm.

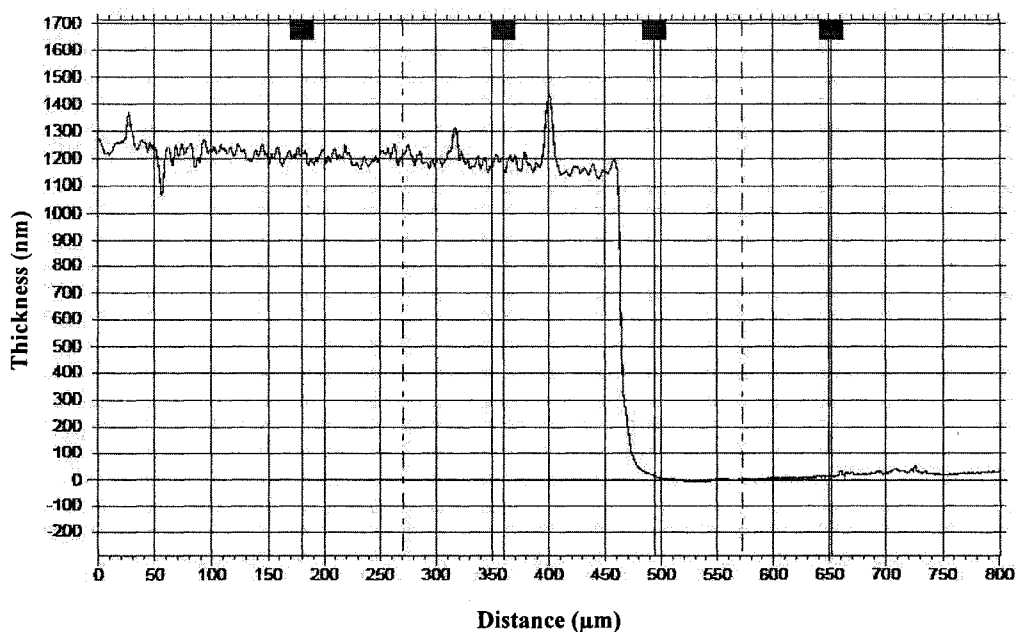


Figure 4.7 Thickness of cellulose acetate insulating layer = 1226 nm.

The characterization of the SnO₂ using Atomic Force Microscope (AFM) layer on PDDA is shown in Figure 4.8. PDDA has a very smooth coating on the cellulose acetate layer and SnO₂ tends to form clumps which crack over time.

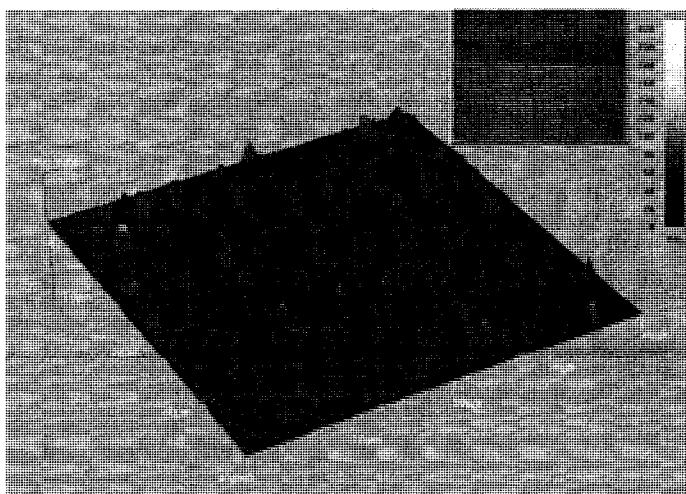


Figure 4.8 AFM image of SnO₂ coated on PDDA (20 x 20 μm area).

4.2 Fabrication of RFID Tag Antenna

The ethylene sensor fabricated in the above mentioned process is then integrated with the triangular microstrip patch antenna. Before the integration, the triangular antenna is fabricated using a photolithography technique. The new triangular antenna with the fork structure (Figure 4.9) was used to increase the R_f to 985 MHz (detailed explanation is given in section 6.2.1) rather than using the original triangular antenna without the fork structure which resonates at 915 Mhz. For preparing the mask from ansoft (adsn file format), the top copper layer of the antenna and then the ground copper layer are selected. The two layers are then transported to design layout format (dxf file) to obtain the mask, as shown in Figure 4.9. The dxf file is converted to a pdf file and is printed using a Linotronic 330 mask-maker instrument (2540 dpi).

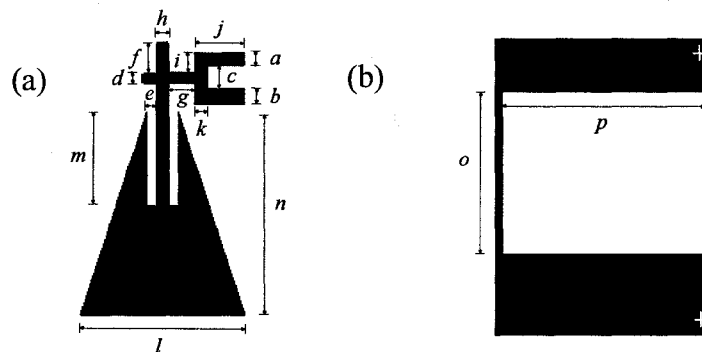


Figure 4.9 Mask for the triangular antenna (a) top layout and (b) ground slot layout.

Alignment markers (shown as the + sign in Figure 4.9) were used for proper overlapping of the top surface with the bottom ground plane. The dimensions of the antenna are $a = 2$ mm, $b = 2.5$ mm, $c = 3.65$ mm, $d = 1.6$ mm, $e = 1.2$ mm, $f = 4.58$ mm, $g = 3.2$ mm, $h = 1.5$ mm, $i = 3.26$ mm, $j = 6.18$ mm, $k = 1.58$ mm, $l = 20.47$ mm, $m = 14.61$, $n = 31.59$ mm, $o = 26.94$ mm, and $p = 40.03$ mm. The photolithography technique

followed for the fabrication of the antenna is given in Figure 4.10. The polyimide substrate was first cleaned with acetone and then with DI water on both sides. The substrate was blow dried with dry nitrogen gas before spin coating photoresist on both sides. About a 2 μm thickness of positive photoresist (PR 1813, Rohm and Haas Company) was coated using a spinner. The initial photoresist spreading speed was 500 rpm for 10 sec with a ramp of 100 rpm. The specified thickness was obtained by increasing the speed to 2000 rpm for 30 sec with a ramp of 500 rpm. After coating one side of the substrate, the substrate was soft baked for 2 min at 100⁰ C to dry the photoresist.

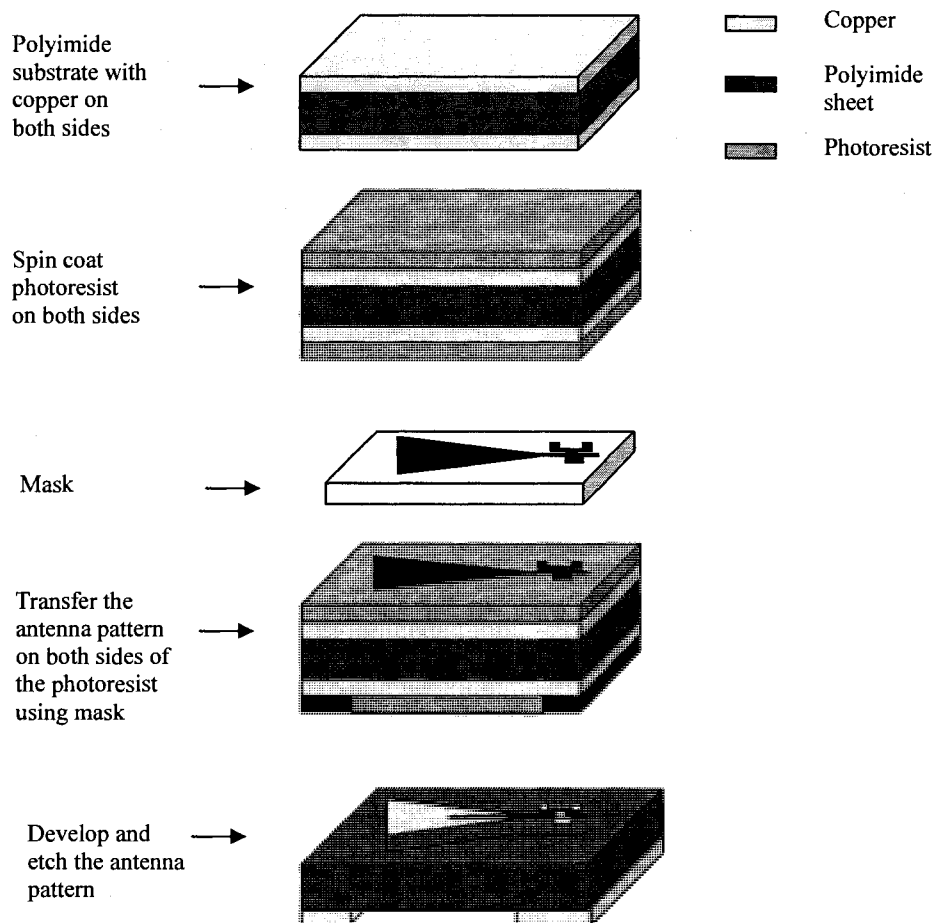


Figure 4.10 Fabrication of microstrip antenna using photolithography.

The process was repeated for the other side also. The antenna pattern is transferred to the photoresist coating by using a mask and placing the mask in contact with the surface of the substrate and exposing to UV rays (wavelength 352 nm) for 3.5 minutes. Care should be taken in aligning the ground slot mask with the top surface mask by using the alignment markers. The substrate was then developed using developer Shipley MF 321 in which the unwanted UV exposed photoresist is washed away and the unexposed photoresist in the shape of the triangular antenna protects the copper under it. The sample was washed and dried with nitrogen gas. The sample was then hard baked at 100^o C for 20 min to harden the photoresist. The antenna structure as a copper patch on the polyimide substrate was obtained by etching the unwanted and unprotected copper using copper etchant (ferric chloride solution). The final antenna structure was obtained as shown in Figure 4.11.

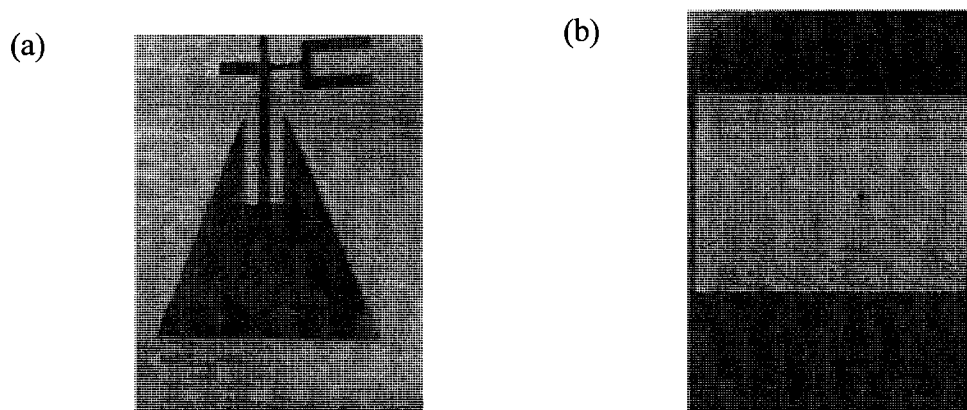


Figure 4.11 Triangular microstrip patch antenna (a) top surface (b) ground slot

4.3 Fabrication Steps for Sensor Integration with Antenna

The integration of the sensor with the antenna involves the fabrication of the sensor on the feed of the antenna. This can be achieved by using the copper feed of the antenna as the bottom plate and the e-beam deposited copper layer as the top layer of the

capacitor. The capacitor gets its electromagnetic energy from the bottom antenna feed and the top plate is grounded to the bottom ground layer of the antenna using solder. The first step in the integration process is the reducing of the thickness of the antenna feed from $35\ \mu\text{m}$ to $5\ \mu\text{m}$. It was then followed by coating the dielectric layers and finally depositing the $300\ \text{nm}$ top copper layer. Figure 4.12 shows the fabricated sensor tag antenna.

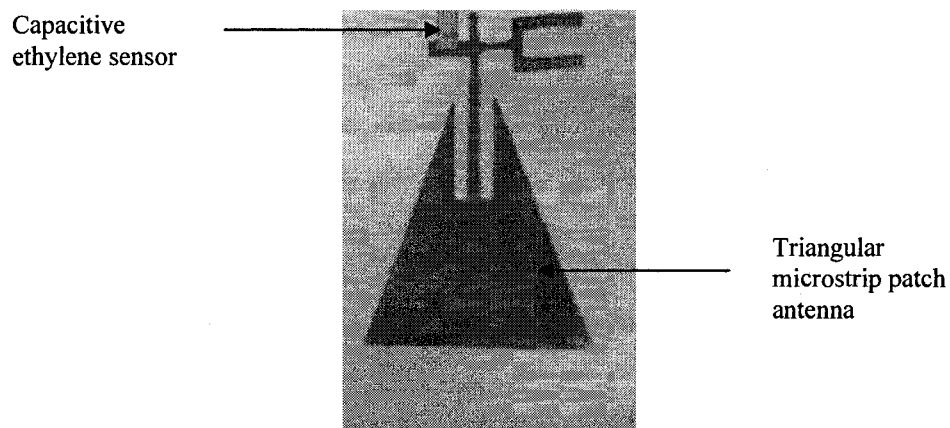


Figure 4.12 Fabricated ethylene sensor integrated with triangular microstrip patch antenna.

Care must be taken in covering the antenna surface when the sensing layer is deposited. This is done by using masking tape (Echo supply, Polyester 4" masking tape). Once the sensing layer is deposited, a shadow mask ($200\ \mu\text{m}$ thick silicon mask) is used to cover the sensing layer and is patterned in such a way so that e-beam copper deposition occurs only on the top of the sensing layer.

CHAPTER 5

EXPERIMENTAL SET-UP

In this dissertation, the experiments are divided into two parts. The first part deals with the ethylene sensor as a standalone device and the first section of this chapter deals with the experimental set-up and measurement techniques used for the experiments. The second part of the chapter deals with the experimental set-up and measurement techniques used for the sensor integrated with the tag antenna.

5.1 Ethylene Sensor

The electrical parameter of measurement for the stand alone ethylene sensor is the capacitance of the device. The instrument used and the experimental set-up is given below.

5.1.1 Experimental Set-up and Measurement Procedures

The ethylene sensors were tested with a Keithley test system 595 quasistatic capacitance-voltage (CV) meter. The two-probe micromanipulator (Model 525) was used as the probing station. Figure 5.1 shows the experimental set-up with the individual ethylene sensors placed inside an airtight chamber. A gas cylinder containing ethylene gas concentration of 100 ppm with nitrogen as the carrier gas was used as the stimulant. The ethylene gas was mixed with dry air using a T-connector with the flow of

ethylene gas and dry air individually adjusted using a flowmeter. The flowmeter used is a standard cubic feet per hour (SCFH) capacity flowmeter filling a chamber of 2.15 L capacity.

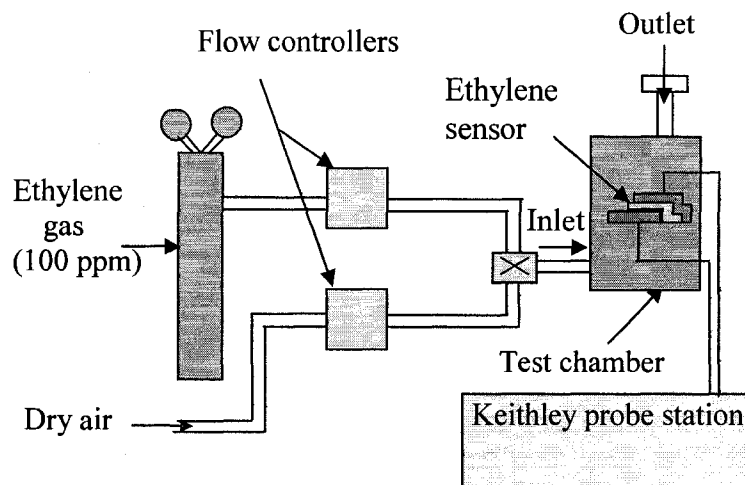


Figure 5.1 Experimental set-up for measuring ethylene sensors.

The flowmeter can supply from 1 to 5 SCFH of ethylene or dry air. To achieve a 20 ppm of ethylene, the ethylene flowmeter was set at 1 SCFH and the dry air flowmeter was set at 4 SCFH. Similarly, for 20 ppm of ethylene, the ethylene flowmeter was set at 2 SCFH and dry air flowmeter is set at 3 SCFH. Thus, 20, 40, 60, 80 and 100 ppm were achieved. A commercial ethylene detector, Oldham MX 2100, was placed inside the chamber to indicate the amount of ethylene gas concentration present inside the chamber. To flush out the ethylene gas, pure dry air was passed. The chamber has an inlet for inflow of ethylene gas and an outlet for the outflow. Two copper clippers with wires were used to connect the top and bottom layers of the capacitors to the keithley probe needles. The sensor parameter measurements can be done in two ways. In the first measurement technique, ethylene gas of specific concentration was passed for a few seconds until the

chamber was filled and then the inlet and outlet were sealed. The capacitive sensor CV measurements were then taken. The voltage supplied was from -1 V to +1 V for which the capacitance was observed. In the other measurement technique the ethylene gas of specific concentration was continuously flowed through the chamber with the outlet kept open.

5.2 Ethylene Sensor Integrated with RFID Tag Antenna

The ethylene sensor was integrated with the RFID tag antenna for wireless measurement of the ethylene gas concentration. This set of experiments needs a different experimental set-up as the measurements now involve wireless collection of sensor output data. The instruments used for this purpose are a network analyzer and RFID reader. All the experiments are done inside an anechoic chamber (Chamber dimensions: 24 x 24 x 24 cubic inches, absorbing material: C-RAM SFC-8, reflectivity at 1 GHz: -30 dB, manufacturer: Cuming Microwave). These experiments also require calibration of the instruments and measurement techniques adapted for the passive wireless detection of ethylene gas.

5.2.1 Experimental Set-up

The experimental set-up to measure the change in return loss and backscattered voltage wirelessly is given in Figure 5.2. Ethylene gas concentration of 100 ppm was mixed with dry air using flowmeters as explained in section 5.1.1. The varying ppm of ethylene was then passed to an air tight chamber in which the sensor integrated antenna was placed. In this set-up, the commercial ethylene detector to detect the concentration of ethylene present inside the chamber was placed outside as any object placed near the antenna affects its characteristics. The ethylene gas was passed to the chamber and the

outlet of the chamber was connected to the ethylene detector. The ethylene gas is vented out through the ethylene detector. The sample to be tested is suspended using a tape attached to the lid of the chamber. In order to measure the return loss of the tag, another triangular patch antenna was connected directly to the network analyzer.

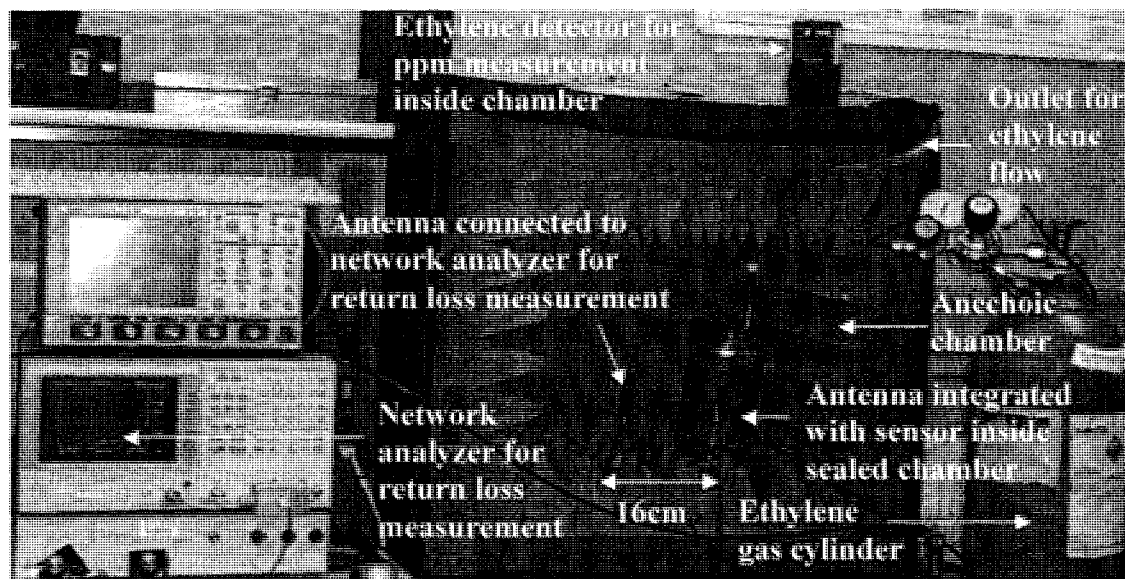


Figure 5.2 Experimental set-up for wireless sensing of ethylene gas.

The distance between the antennas was optimized at 16 cm which will be explained in the next section. A close up view of the chamber is given in Figure 5.3. The chamber with the sample and the receiving microstrip antenna was placed inside an anechoic chamber to absorb internal reflections due to objects and to reflect external noise signals affecting the measurements. For measuring the resonant frequency shift due to the presence of ethylene, the antenna was directly connected to the network analyzer through a connection to the feed of the antenna.

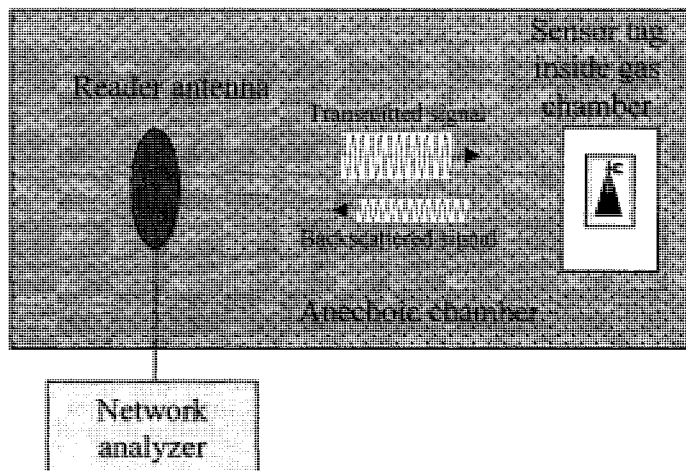


Figure 5.3 Schematic diagram to show the interaction between reader antenna and sensor tag.

For measuring the backscattered signal voltage, the receiving antenna was connected to the reader directly instead of to the network analyzer with the rest of the experimental set-up remaining the same.

5.2.2 Measurement Techniques and Procedures

Before beginning the sensor integrated antenna experiments in the anechoic chamber, network analyzer calibration, anechoic chamber noise canceling procedure, and distance optimization between the tag antenna and receiving antenna were performed. For measuring the resonant frequency, only the network analyzer calibration was performed. For measuring return loss and backscattered signal amplitude, anechoic chamber noise canceling procedure and distance optimization were performed.

(i) Network analyzer calibration

The network analyzer calibration was performed to standardize the network analyzer for open, short, and 50 Ω load. Standard calibration connectors were used for

this purpose. The three connectors were connected in sequence and then the analyzer was instructed to calibrate. The important criterion in this calibration is that the calibration connectors have to be connected only at the point where the antenna with sensor will be connected for experiments. This means that the connectors have to be connected after the cables and just before the antenna connection. This calibration also takes the cable length into consideration for reflections and cancels the effect of the cable's electrical length.

(ii) Anechoic chamber noise canceling procedure

Even though anechoic chambers are designed to absorb internal RF signals and reflect external noise signal from entering the chamber, Nikitin, et al. in [81] proved that there will still be internal reflections and these reflections affect the antenna characteristics. Hence, an anechoic chamber noise cancellation procedure as given in [81] is followed. This method is similar to the calibration of the network analyzer procedure where, instead of connecting the 50Ω load connector, the receiving antenna was connected and the gas chamber, without the sample, was also placed inside the anechoic chamber. The network analyzer was then instructed to calibrate. This procedure cancels the reflections present inside the anechoic chamber.

Figure 5.4 shows the return loss measured before and after noise cancellation. The signal before calibration shows a high return loss of -28 dB at 900 MHz due to internal reflections and after calibration, the dominant internal reflected signals were cancelled and pushed to the noise level return loss of -50 dB.

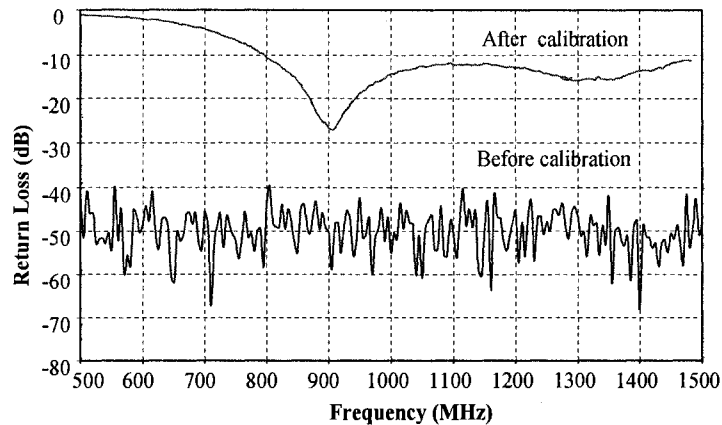


Figure 5.4 Antenna return loss measured in the empty anechoic chamber before and after calibration.

(iii) Distance optimization between the tag antenna and receiving antenna

The operating RFID tag antenna signal is a continuous 915 MHz sinusoidal signal. In air, these RF signals tend to have a standing wave pattern [76]. Due to the wave pattern, a maximum change in return loss or backscattered signal amplitude caused by the additive effect of transmitted and reflected signals occurs only at certain distance points. These points are repetitive for every wavelength cycle. Samples placed and measured at any other distance will not show a large change in parameters due to any change in the capacitance of the sensor since the subtractive effect overshadows the results. Hence, it is very important to optimize the distance between the tag antenna and the receiving antenna connected to the network analyzer or reader. Figure 5.5 shows the experimental results for the optimized distance of 16 cm between our sensor tag and the receiving antenna.

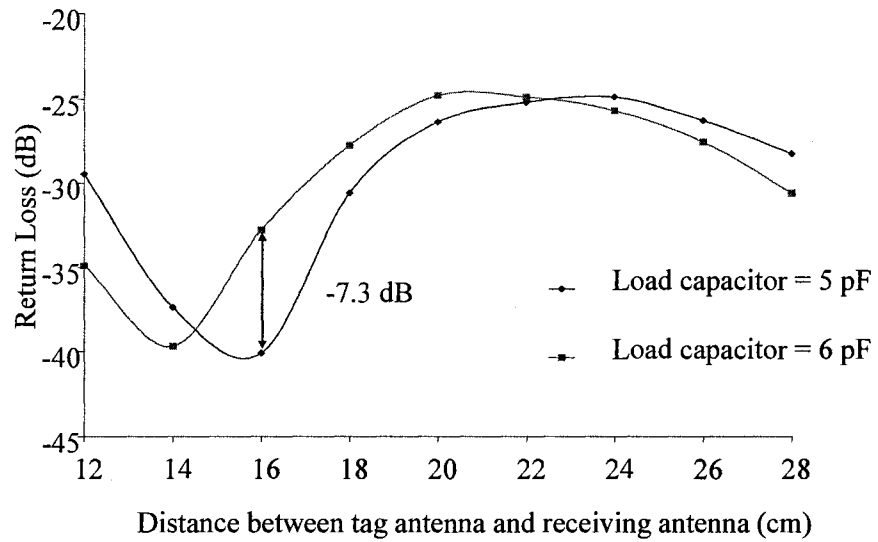


Figure 5.5 Distance optimization between the tag antenna and receiving antenna.

In order to optimize the distance, an RFID tag antenna integrated with a lumped capacitor of specific capacitance (5 pF) was placed at varying distances from the transmitting/ receiving (Tx/Rx) antenna. The return loss was measured using a network analyzer. The same procedure was repeated with another capacitor (6 pF) to observe the distance at which the return loss change is maximum. Figure 5.5 shows that a maximum return loss change of -7.3 dB occurs at 16 cm.

CHAPTER 6

RESULTS AND DISCUSSION

This chapter comprises of four sections. In the first section, we present the results and discussions for ethylene sensors working as a stand alone device. In the second part of the chapter, we present the results and discussions for the ethylene sensor integrated with the antenna. In this section we also present simulation results and compare the result with experimental values. The third part of the chapter explains the initial set of results obtained for detecting passive multiple tags functioning on backscattering technique at varying distances. The last section of this chapter deals with the experimental results for the sensor tag output read by the RFID reader.

6.1 Ethylene Sensor

The standalone ethylene sensors were tested for their response to ethylene gas concentration of 0 to 100 ppm. As mentioned before, SnO₂ nanoparticles as the sensing dielectric layer in the capacitor model was tested at room temperature. The sensor's sensitivity, repeatability, reproducibility, response time, recovery time and selectivity were experimentally observed and improved.

6.1.1 Experimental Results

The capacitive ethylene sensors were tested for ethylene concentration from 0 to 100 ppm. The CV characteristics of the sensor response to ethylene were plotted. Pure SnO₂ nanoparticles coated to form the sensing dielectric layer were tested. As Pt and Pd particles are known for their catalytic effect to enhance the sensitivity of SnO₂ nanoparticles to ethylene gas stimulant [14][82], a layer of 10 nm thickness of Pt/Pd alloy (80:20) was deposited by sputtering technique. The sensor characteristics were compared for both pure SnO₂ and SnO₂ with Pt/Pd layer.

6.1.1.1 Sensitivity and Reproducibility

Figure 6.1 shows the sensitivity to ethylene gas for a pure SnO₂ dielectric layered sample and SnO₂ coated with Pt/Pd. The capacitance decreases linearly with different concentration of ethylene.

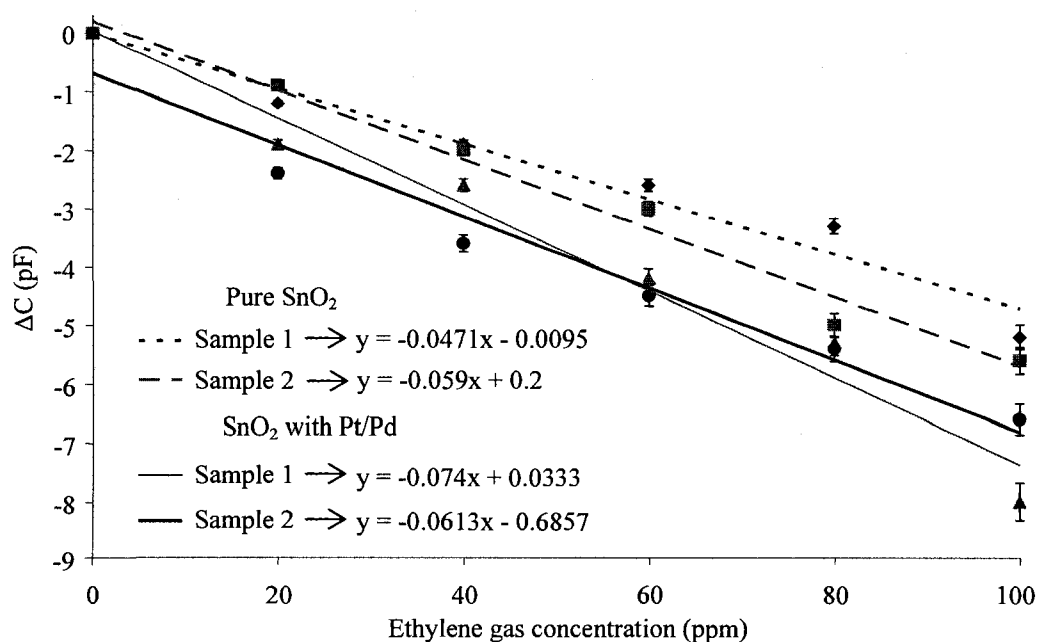


Figure 6.1 Sensitivity and reproducibility of capacitive ethylene sensor to ethylene.

ΔC represents the amount of change in capacitance when ethylene is sensed compared to the original value of sensor capacitance in air, as given below.

$$\Delta C = C - C_0 \quad (6.1)$$

where, C_0 is the capacitance of the sensor in air (0 ppm) and C is the capacitance at varying ethylene gas concentrations. The negative value indicates that the capacitance decreases for an increase in ethylene concentration. From Figure 6.2, we can see that the overall change of pure SnO₂ to ethylene gas concentration from 0 to 100 ppm is 5 pF and for SnO₂ with Pt/Pd is 7 pF, thus showing that the Pt/Pd layer on the SnO₂ has enhanced the sensitivity of SnO₂ nanoparticles to ethylene gas by 39%. Two different samples (sample A and B for pure SnO₂ as the dielectric and sample C and D for SnO₂ coated with Pt/Pd layer as the dielectric) were used to observe the reproducibility of the sensing layer. The linear fit has been plotted using statistical analysis software (SAS) [83]. The program written to extract the statistical parameters and the output data are given in Appendix A. Table 6.1 summarizes the key results used for the data analysis.

Table 6.1 Statistical data for sensitivity and reproducibility experimental data points.

	Pure SnO ₂		SnO ₂ with Pt/Pd	
	Sample A	Sample B	Sample A	Sample B
Sum of Square Error	0.57619	0.42800	1.10133	1.02343
R-Square	96.43%	98.27%	97.21%	96.25%
F- Statistic	108.00	227.73	139.22	102.76
T- Statistic (Intercept, Slope)	-0.03,-10.39	0.84,-15.09	0.09,-11.80	-1.87,-10.14
Slope	-0.0471	-0.059	-0.0471	0.0613

The key parameters used for the statistical analysis are the Sum of Square Error which quantifies the variability between the response estimate and the predicted value and R-Square value which gives the percentage of variability that has been accounted for by the linear fit. F-Statistic gives the significance of the regression and T-Statistic gives the estimate of the linear fit presenting the significance of the intercept and slope. Finally the value of the slope is noted for sensitivity comparisons between samples. The program, output data, and output plot are given in Appendix A.

From Table 6.1, we see that the R square values for sample A and B (for pure SnO₂) are 96.43% and 98.27% which indicates that almost all the data variability are accounted for in the regression model. For the same samples, the value of $F_{0.01, 1, 4}$, found using F-Table is 21.20, which is smaller than the F-Statistic (108.00 and 227.73) obtained, indicating the significance of the regression variable with 99.0% confidence. The T-Statistic $T_{0.005, 1, 4}$ for the same samples was 4.604, found using T-Table. The intercepts for sample A and sample B were -0.03 and 0.84 respectively which are less than 4.604 implying that the hypothesis that the intercept of the model is equal to zero is true with 99.0% confidence. In other words, the intercept intersects at zero. For the slopes of sample A and B their absolute t-values (-10.39 and -15.09) are greater than 4.604, implying that the hypothesis that the intercept of the model is equal to zero is rejected with 99.0% confidence. In other words the slope of the linear fit is significant which implies that the sensor is considerably sensitive to the stimulant.

For the samples C and D with the dielectric made of SnO₂ with a Pt/Pd layer, the R square values were 97.21% and 96.25% which indicates that almost all of the data variability is accounted for in the regression model. For the same samples, the value of

$F_{0.01, 1, 4}$, is 21.20 which is smaller than the F-Statistic (139.22 and 102.76) obtained, indicating the significance of the regression variable with 99.0% confidence. The T-Statistic $T_{0.005, 1, 4}$ for the same samples was 4.604. The intercepts for sample C and sample D were 0.09 and -1.87 respectively which are less than 4.604 implying that the hypothesis that the intercept of the model is equal to zero is true with 99.0% confidence. For the slopes of sample C and D their absolute t-values (-11.8 and -10.14) are greater than 4.604, implying that the hypothesis that the intercept of the model is equal to zero is rejected with 99.0% confidence. In other words, the slope of the linear fit is significant which implies that the sensor is considerably sensitive to the stimulant.

The difference between the slopes of pure SnO₂ samples A and B is 0.0119 and for samples C and D is 0.0142. As the values are almost the same, both samples with only pure SnO₂ and samples with Pt/Pd are reproducible. However, samples with dielectric SnO₂ with Pt/Pd layer are very slightly greater than samples with pure SnO₂ as the dielectric.

6.1.1.2 Hysteresis

Hysteresis of a sensor is the shift in the parametric values of the sensor when the stimulant is removed. In other words, it is the measure of the accurate repeatability of the sensor data points to the stimulant during the increasing and decreasing of the sensed stimulant. Figures 6.2 and 6.3 shows the hysteresis of the sensor with pure SnO₂ and SnO₂ with the Pt/Pd layer, respectively. The SnO₂ sample with Pt/Pd layer shows hysteresis similar to the hysteresis effect observed by Dennis, et al. [84] the cause of which is attributed to the imbalances in the catalytic nature of Pd nanoparticles dissociating oxygen and producing O⁻ ions.

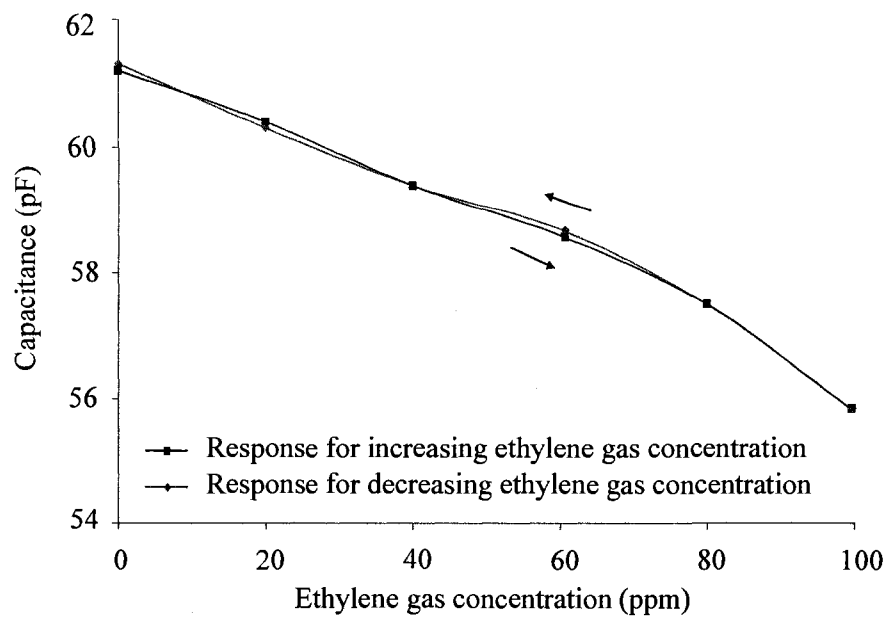


Figure 6.2 Hysteresis of pure SnO_2 dielectric layer capacitor when exposed to ethylene.

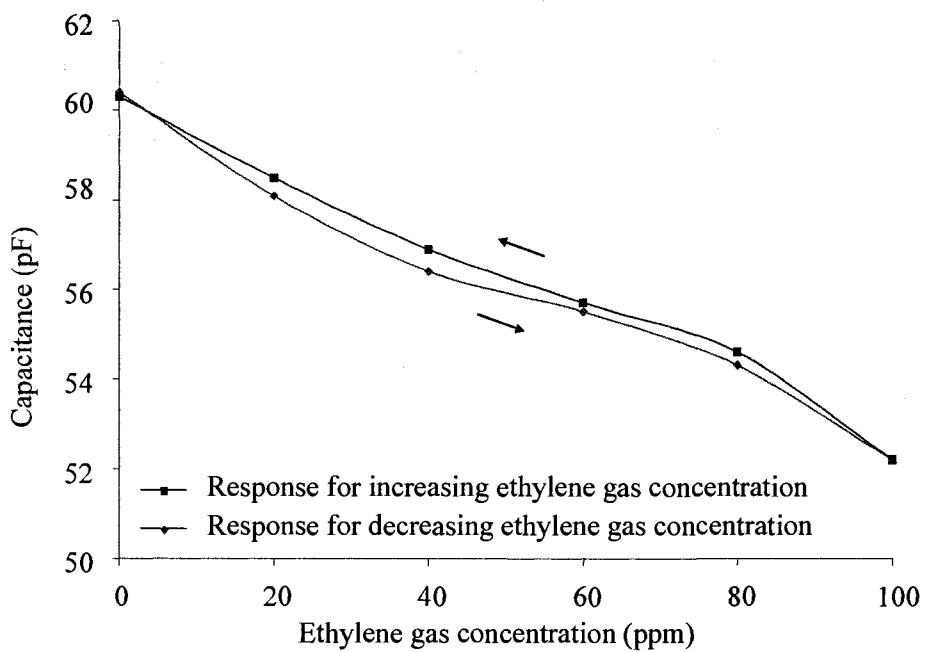


Figure 6.3 Hysteresis of SnO_2 with Pt/Pd dielectric layer capacitor when exposed to ethylene.

6.1.1.3 Degradation

Figure 6.4 shows the degradation of the sensor over time. The same sample was tested for 5 days under the same testing condition. The dotted line indicates the pure SnO₂ sample and the solid line indicates the SnO₂ with Pt/Pd sample showing an overall change of 5 pF and 7.5 pF for pure SnO₂ and SnO₂ with Pt/Pd samples, respectively.

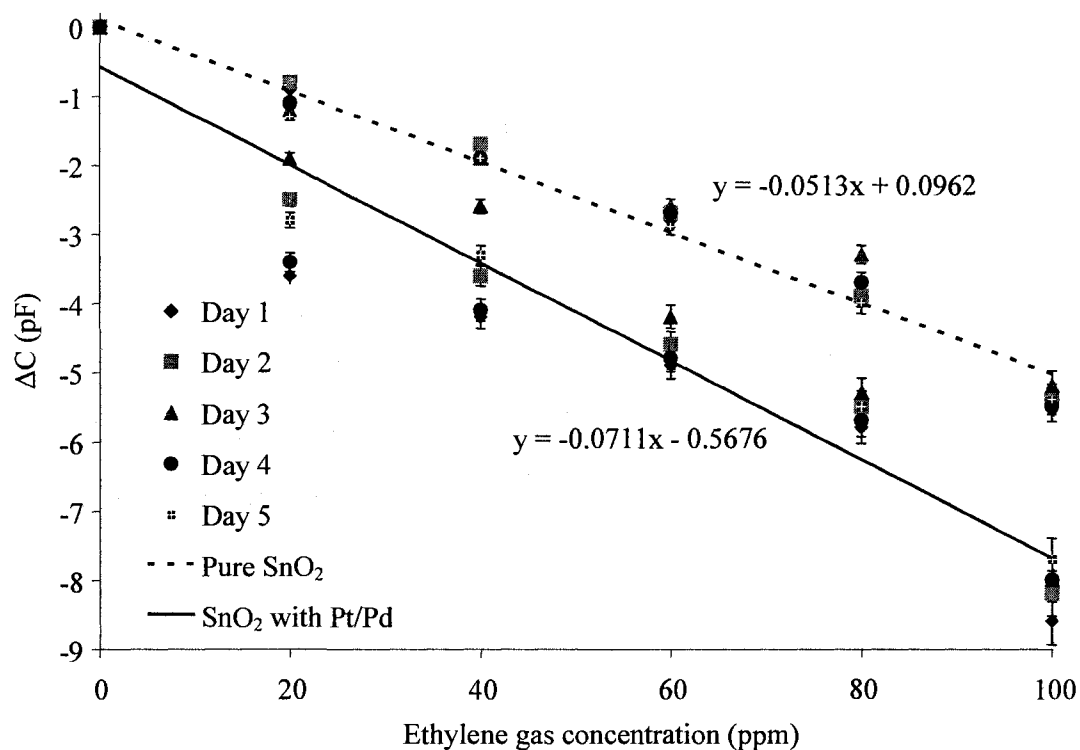


Figure 6.4 Degradation of ethylene sensor for varying ethylene concentrations.

The linear fit has been plotted using the SAS program and the summary of the extracted statistical parameters is given in Table 6.2 for both samples. From Table 6.2, we see that the sum of square error is less for both the samples, indicating that the linear fit is well suited for the experimental data points obtained as the difference between the experimental data and the predicted values are less. The R square values for pure SnO₂

and SnO₂ with Pt/Pd are 97.88% and 93.02%, which indicates that almost all the data variability is accounted for in the regression model.

Table 6.2 Statistical data for the degradation study.

	Pure SnO ₂	SnO ₂ with Pt/Pd layer
Sum of Square Error	1.99135	0.47465
R-Square	97.88%	93.02%
F-Statistic	1292.96	372.91
T-Statistic (Intercept, Slope)	1.11,-35.96	-2.55,-19.31
Slope	-0.05126	-0.07111

For the same samples, the value of $F_{0.01, 1, 28}$ is 7.64 which is smaller than the F-Statistic (1292.96 and 372.91) obtained indicating the significance of the regression variable with 99.0% confidence. The F-static values for these experimental data points are high as the number of sample data points is 28 whereas for the sensitivity experiments, the number of data points was 4. The T-Statistic $T_{0.005, 1, 28}$ for the same samples was 2.763, found using T table. The intercepts for the samples were 1.11 and -2.55 respectively which are less than 2.763 implying that the hypothesis that the intercept of the model is equal to zero is true with 99.0% confidence. In other words, the intercept intersects at zero. As for the slopes of the samples, their absolute t-values (-35.96 and -19.31) are greater than 2.763, implying that the hypothesis that the intercept of the model is equal to zero is rejected with 99.0% confidence.

Table 6.3 shows the comparison of the slope between the two samples for the first day and last day of measurement and the difference in their slope to show which sample has more degradation than the other. The difference in slope between day 1 and day 5 for

the sample with pure SnO₂ is lesser than the sample with the Pt/Pd layer indicating that the degradation is less for pure SnO₂.

Table 6.3 Comparison of slopes between day 1 and day 5 of the samples.

	Day 1	Day 5	Difference in slope
Pure SnO ₂	-0.0527	-0.0516	0.0011
SnO ₂ with Pt/Pd layer	-0.0719	-0.0689	0.0030

Statistically the difference in slope is very small indicating that both samples show little degradation over time. However, pure SnO₂ samples show more repeatable data points than SnO₂ with Pt/Pd, as seen in Figure 6.4. The variations in the data points for 20 ppm and 40 ppm can be attributed to the variations in the oxygen dissociation on Pd particle surface at room temperature [85]. Oxygen dissociates into O⁻ ions when it encounters Pd which acts as a catalyst. This atomic oxygen spill over from the Pd to the SnO₂ surface enhances the reaction of ethylene gas with the SnO₂ nanoparticles. The effect can be clearly observed from Figure 6.4, as only the first two ethylene concentrations show more variations in data values which later stabilize to more repeatable data values. Therefore, this effect can be minimized if the sensor was allowed more time for the above mentioned phenomena to take place and then measured for ethylene gas stimulant.

6.1.1.4 Response Time and Recovery Time

The sensor response time and recovery time is given in Figure 6.5. From the figure we can see that SnO₂ with the Pt/Pd layer has the faster response time of about 3

min as compared to the pure SnO_2 sample with a 5 min response time. The recovery time for pure SnO_2 is higher at 7 min as compared to SnO_2 with the Pt/Pd layer which has a faster recovery time of 5 min. Therefore, the overall response time and recovery time is improved by 40% and 28% respectively. The faster response time and recovery time is also attributed to the catalytic effect of platinum and palladium in SnO_2 to ethylene gas.

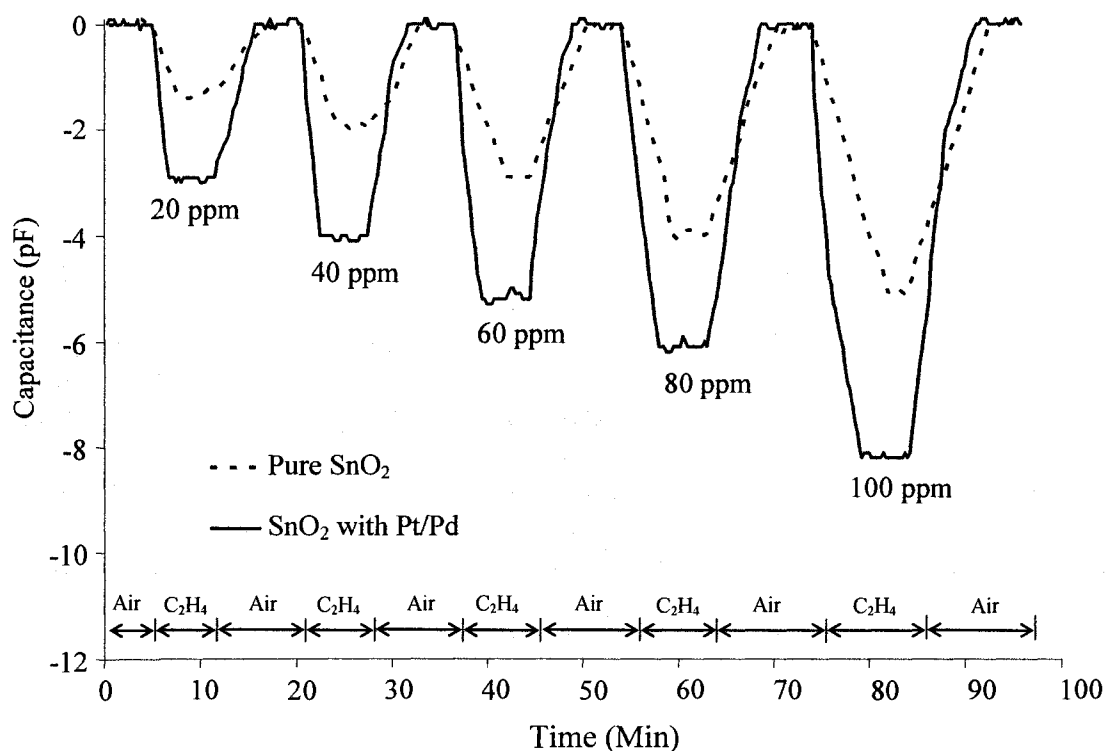


Figure 6.5 Response time and recovery time of pure SnO_2 and SnO_2 with Pt/Pd to ethylene concentration.

6.1.1.5 Selectivity

The selectivity of a gas sensor denotes the capability of the sensor to sense its targeted stimulant in a mix of other gases. In our case, the sensor is used to sense ethylene emanated from fruits which means that it should be able to detect ethylene from among other gases present in the warehouse environment as well as from gases

emanating from the fruit. In [14], the sensor is demonstrated for its sensitivity to ethylene gas when compared to ethanol and ammonia. According to the paper, ethanol is a gas that is emanated when the fruit is subjected to respiration stress. Ammonia is another gas present in warehouses due to leakage from refrigeration units. As given in [86], carbon dioxide (CO_2) is another gas most commonly present in warehouses as CO_2 emanates from both climacteric and non-climacteric fruits. The amount of CO_2 present in warehouses has been collected and presented by T. Thomas and M. Skaria, as shown in Figure 6.6.

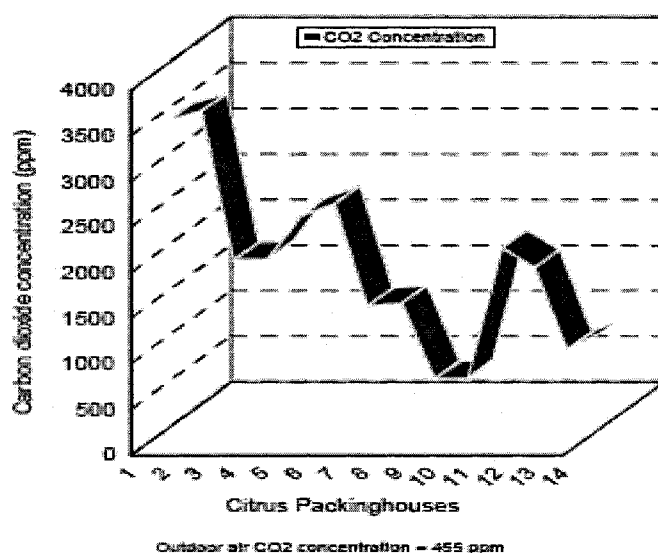


Figure 6.6 Concentration of CO_2 present in warehouses [87].

Therefore, we have checked the sensor's sensitivity to ethylene in a carrier concentration of CO_2 gas of 1000, 2000 and 3000 ppm. Sensitivity of sensors is usually increased by adding dopants and using multiple sensors in an array [88]. We have adopted the technique of adding other metals as a layer to the SnO_2 nanoparticle sensing

layers. From [14], we see that the sensitivity of the SnO₂ nanoparticle layer to ethylene gas can be increased by adding Pd or Pt.

In Figure 6.7, a comparison of the sensitivity of pure SnO₂ and SnO₂ with a Pt/Pd layer to ethylene gas concentration of 0 to 100 ppm mixed with three different CO₂ gas concentrations of 1000, 2000 and 3000 ppm is given. The calculations for achieving the required concentrations are given in Appendix B.

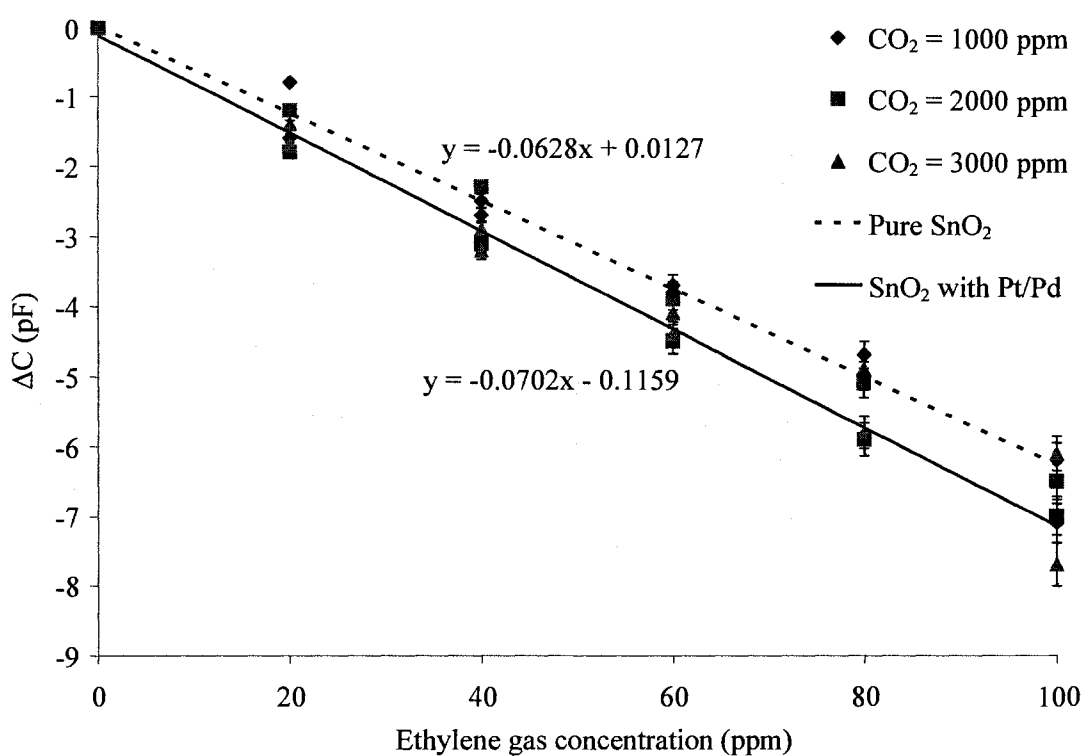


Figure 6.7 Sensitivity of pure SnO₂ and SnO₂ with Pt/Pd layer to ethylene gas concentration mixed with CO₂ gas.

The pure SnO₂ dielectric layer based capacitive sensor shows an overall change of 6 pF decrease in capacitance and SnO₂ with Pt/Pd shows an overall change of 7.2 pF for an increase in concentration of ethylene from 0 to 100 ppm.

The linear fit has been plotted using SAS program and the summary of the extracted statistical parameters for the sample with pure SnO₂ and the sample with Pt/Pd is given in Table 6.4. From Table 6.4, we see that the sum of square error is less (0.77035 for pure SnO₂ and 1.53492 for SnO₂ with a Pt/Pd layer) for both the samples, indicating that the linear fit is well suited for the experimental data points obtained as the difference between the experimental data and the predicted values are less. The R square values for pure SnO₂ and SnO₂ with Pt/Pd are 97.88% and 93.02% which indicates that almost all the data variability are accounted for in the regression model.

Table 6.4 Statistical data for selectivity study.

	Pure SnO ₂	SnO ₂ with Pt/Pd layer
Sum of Square Error	0.77035	1.53492
R-Square	99.08%	98.54%
F- Statistic	1720.69	1079.94
T- Statistic (Intercept, Slope)	0.14, -41.48	-0.9, -32.86
Slope	-0.06281	-0.07024

For the same samples, the value of $F_{0.01, 1, 16}$ is 8.53 which is smaller than the F-Statistic (1292.96 and 1079.94) obtained indicating the significance of the regression variable with 99.0% confidence. The F-static values for these experimental data points are high as the number of sample data points is 16 whereas for the sensitivity experiments, the number of data points was 4. The T-Statistic $T_{0.005, 1, 16}$ for the same samples was 2.921, found by using T table. The intercepts for the samples were 0.14 and -0.9 respectively, which are less than 2.921, implying that the hypothesis that the intercept of the model is equal to zero is true with 99.0% confidence. In other words, the

intercept intersects at zero. As for the slopes of the samples, their absolute t-values (-41.48 and -32.86) are greater than 2.921, implying that the hypothesis that the intercept of the model is equal to zero is rejected with 99.0% confidence.

Using Table 6.2 and Table 6.4, the difference in slope for the pure SnO₂ sample is 0.01155 and for SnO₂ with Pt/Pd is 0.0009 which shows that the sample with pure SnO₂ has cross sensitivities to CO₂. Also, when comparing Figure 6.1 and Figure 6.7, the overall change of pure SnO₂ has increased from 5 pF to 6 pF, whereas for SnO₂ with a Pt/Pd layer it has remained the same. This clearly indicates that pure SnO₂ has cross sensitivities to CO₂ gas and that the addition of Pt/Pd has increased the sensitivity of the SnO₂ dielectric layer to ethylene gas by 1 pF. Thus, the addition of Pt/Pd layer to SnO₂ has increased the selectivity by 66%.

6.2 Ethylene Sensor Integrated With RFID Tag Antenna

The antenna parameters were measured for the sensor integrated with tag antenna using simulation and experiments. The simulation results are presented for the shift in frequency due to the change in ethylene gas concentration. The experiments performed to sense ethylene when the ethylene sensor is integrated with tag antenna involves detecting the antenna characteristics. The antenna characteristics change when the sensor integrated with it senses ethylene. The main parameters of measurements are resonant frequency shift, return loss and backscattered voltage. Return loss and backscattered voltage are measured wirelessly and resonant frequency is measured by connecting the sensor integrated antenna with a network analyzer.

6.2.1 Simulation Results

As mentioned before in section 3.4.2.2, the triangular microstrip patch antenna with two ports is created in the EM plane. This is later modeled as a component and imported to the circuit level where the sensor is represented as a variable capacitor. When the value of the capacitance is varied, there is a shift in the antenna resonance frequency. We know that when a capacitive ethylene sensor is integrated with the antenna, the capacitance of the sensor in air before the ethylene gas is sensed has its own capacitance value. From experiments, it was observed that this value is about 6 pF. From experiments and simulation results, it was also observed that a 6 pF of capacitance shifts the resonant frequency by 70 MHz. Hence, a 915 MHz antenna is modified to resonate at 985 MHz so that when a capacitive ethylene sensor is integrated, it pushes the antenna to resonate at 915 MHz. In order to modify the triangular antenna to resonate at 985 MHz, a tuning fork structure, as shown in Figure 6.8, was added to the feed of the antenna.

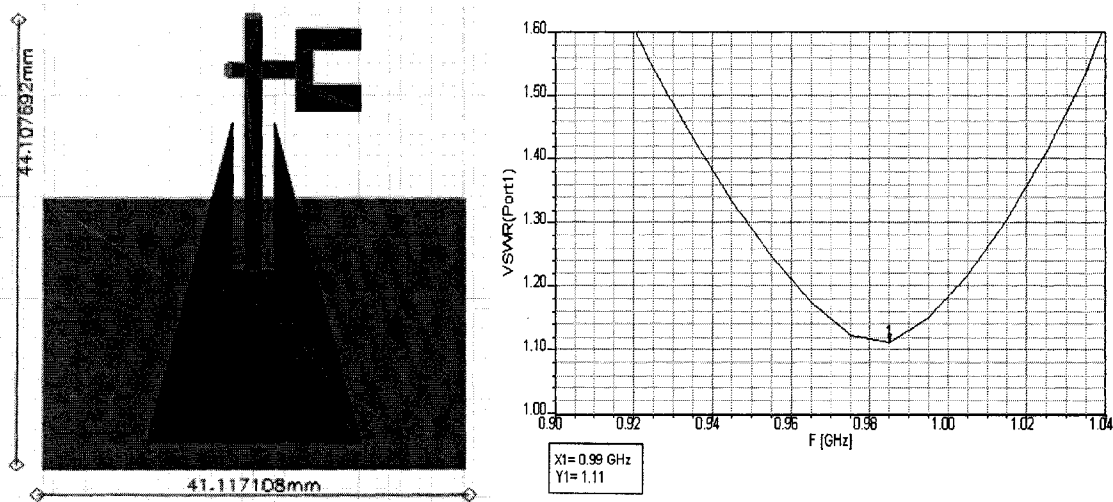


Figure 6.8 Modified triangular microstrip patch antenna resonating at 985 MHz with VSWR = 1.69.

In [89], Alam, et al. has presented that the use of a tuning fork structure has aided in better optimization of the microstrip antenna and also greatly improved the radiation pattern of the antenna. Hence, the tuning fork structure was used in our triangular antenna to increase the resonant frequency of the antenna and also for better optimization of the antenna structure with better radiation pattern. The designing of the antenna to higher resonating frequency significantly decreased the size of the antenna by 63% when compared to the original antenna given in [72].

The circuit level representation of the sensor integrated with antenna is shown in Figure 6.9. When the capacitance of the sensor model was varied from 0 to 10 pF, a shift in resonant frequency was observed (Figure 6.10).

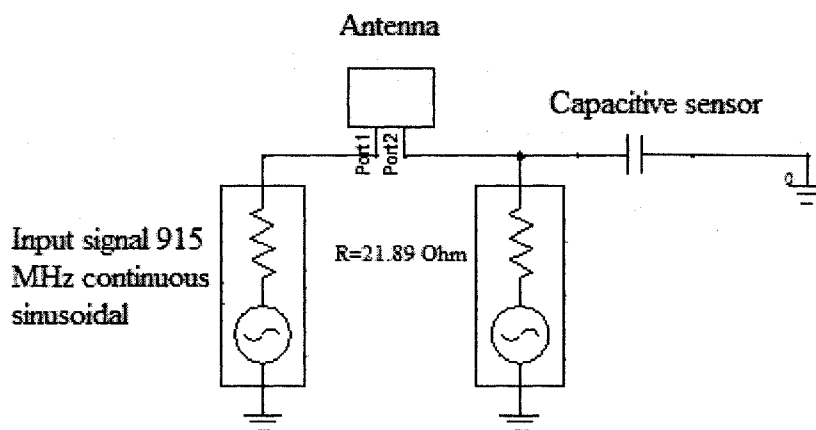


Figure 6.9 Circuit level model of sensor integrated with tag antenna.

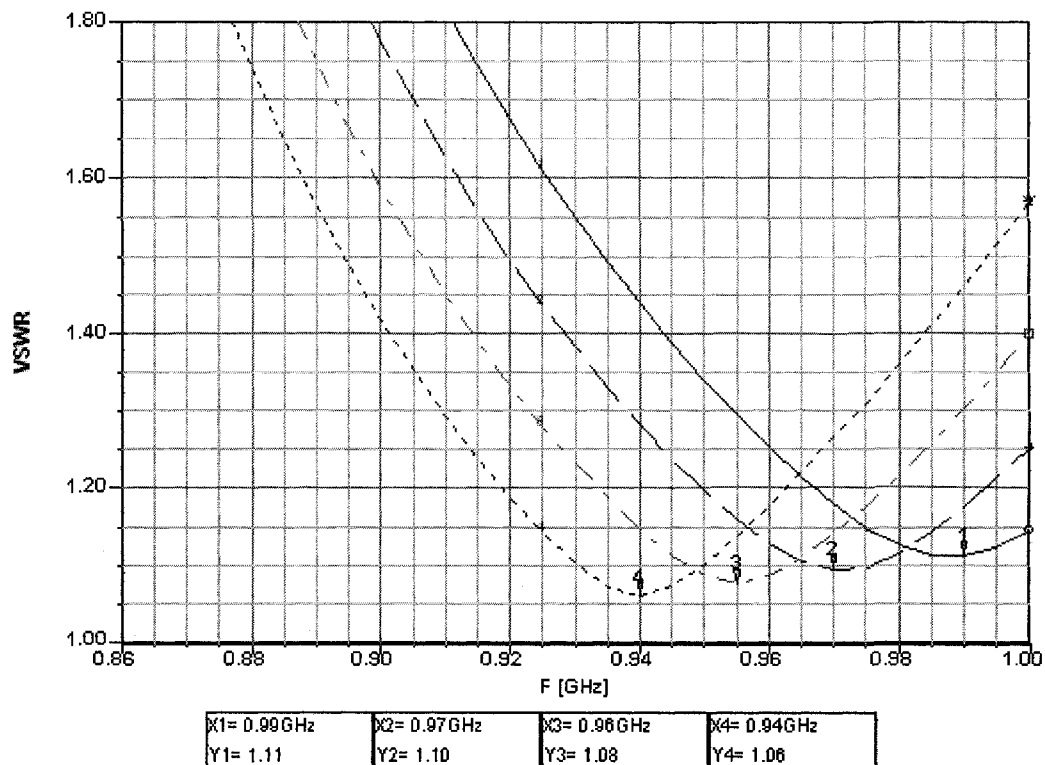


Figure 6.10 Simulation results for shift in R_f for change in capacitance of the sensor.

6.2.2 Experimental Results

Figure 6.11 shows the change in resonant frequency of the integrated sensor antenna as a function of ethylene gas concentration. As seen in the simulation result (Figure 6.10), the experimental result for the resonant frequency for the antenna integrated with the ethylene sensor also increased for a decrease in capacitance.

Two different samples, identified as samples A and B, were considered for this experiment. Sample A resonates at 961 MHz and sample B resonates at 937 MHz before being exposed to ethylene. This means that the integrated sensor for sample A has a capacitance of 2.5 pF and sample B has a capacitance of 4 pF. In order to confirm the change in resonant frequency, simulations were also performed, where the experimentally determined capacitance values corresponding to the ethylene concentrations of interest

were used as values for the capacitive loads of the simulated microstrip patch antenna. The resulting simulation curve, also shown in Figure 6.11, closely matches with the experimental data.

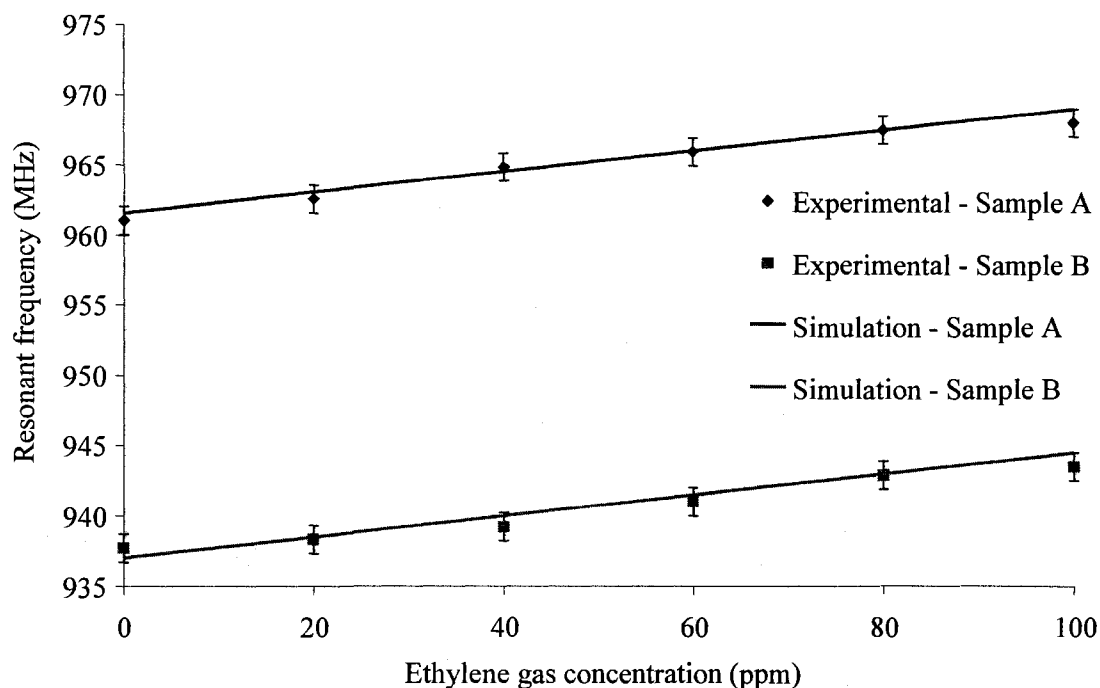


Figure 6.11 Simulation and experimental data for shift in resonant frequency of antenna.

A 7 MHz increase in resonant frequency was observed for sample A and 5.8 MHz of increase in resonant frequency was observed for sample B for a change in ethylene concentration from 0 to 100 ppm. Figure 6.12 shows the wireless detection of the change in the return loss of the sensor antenna by a receiving antenna kept at a distance of 16 cm. The initial calibration for the return loss measurement was performed. As shown in Figure 6.12, over the ethylene concentration range of 0 to 100 ppm, the return loss was reduced by 10.5 dB for sample A and 8.8 dB for sample B, with respect to the respective

antenna's initial resonant frequency (R_f). The solid line in Figure 6.12 represents the linear fit to the displayed measured data points.

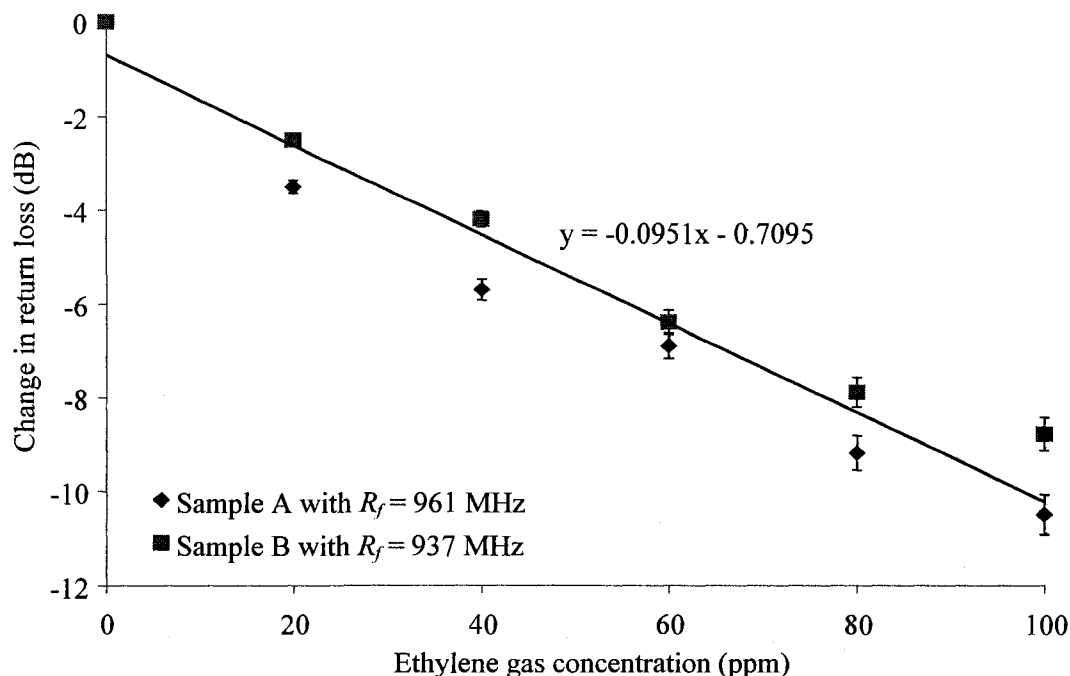


Figure 6.12 Change in return loss with ethylene gas concentration.

Comparing Figure 6.11 and Figure 6.12, we see that the amount of change in return loss is much higher for sample A with a higher frequency shift than for sample B with a lower resonant frequency shift.

6.3 Multiple Tag Detection at Varying Distance

The sensor tag presented in this dissertation detects ethylene and the output detected by the reader is in the form of a varying backscattered signal amplitude with change in ethylene concentration. With this type of passive RFID system, two types of problems exist. (1) It is also known that the amplitude of the backscattered signal is a higher amplitude when placed closer to the reader antenna than the tag placed further away from the reader antenna. Hence, a reader can misread the data from a tag sensing a

high concentration of ethylene compared to a tag sensing a low concentration of ethylene just because of the placement of the tag being further away from the reader antenna since the amplitude of the backscattered signal will be low in both cases. (2) The second difficulty in such a system is detecting multiple tags as all tags resonate at the same frequency.

The above mentioned problems have been solved by using multiple tags with different antenna resonant frequencies and measuring the return loss. The experimental set-up for this experiment is shown in Figure 6.13.

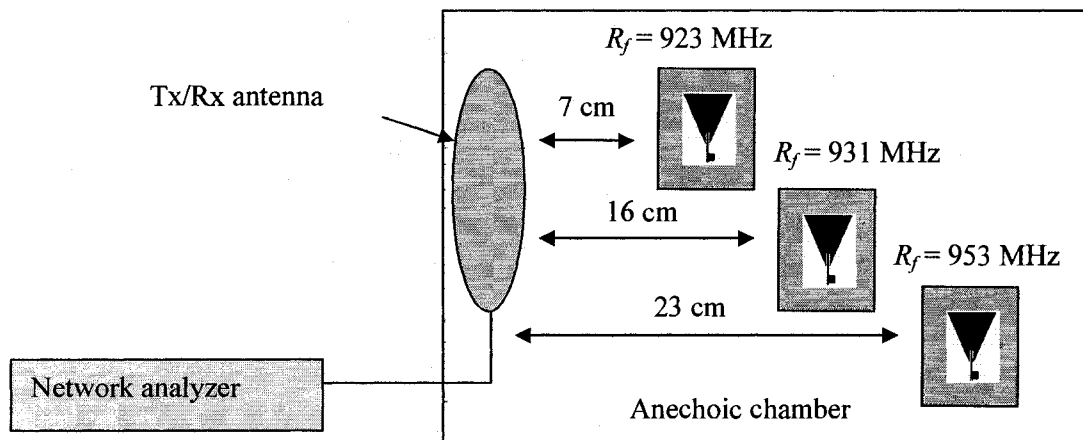


Figure 6.13 Experimental set-up for multiple tag testing at varying distances.

The network analyzer is used to transmit a range of frequencies and measure the return loss reflected from the antenna under detection. Three antennas resonating at 923 MHz, 931 MHz, and 953 MHz were consecutively tested for return loss at varying distances of 7 cm, 16 cm, and 23 cm. From the data plots shown in Figure 6.14, it can be noted that all three antennas, when placed at a distance of 7 cm from the reader, will record a return loss of -25 dB only at the respective resonant frequency of each antenna

when the reader is sweeping a frequency range. Similarly, all the three antennas when placed at 16 cm from the reader, will record a return loss of -32 dB only at respective resonant frequency of each antenna. Thus, for applications where the distance between the reader and the tags is not fixed, the tags, which are designed with varying frequencies along with the presented experimental set-up, can be used.

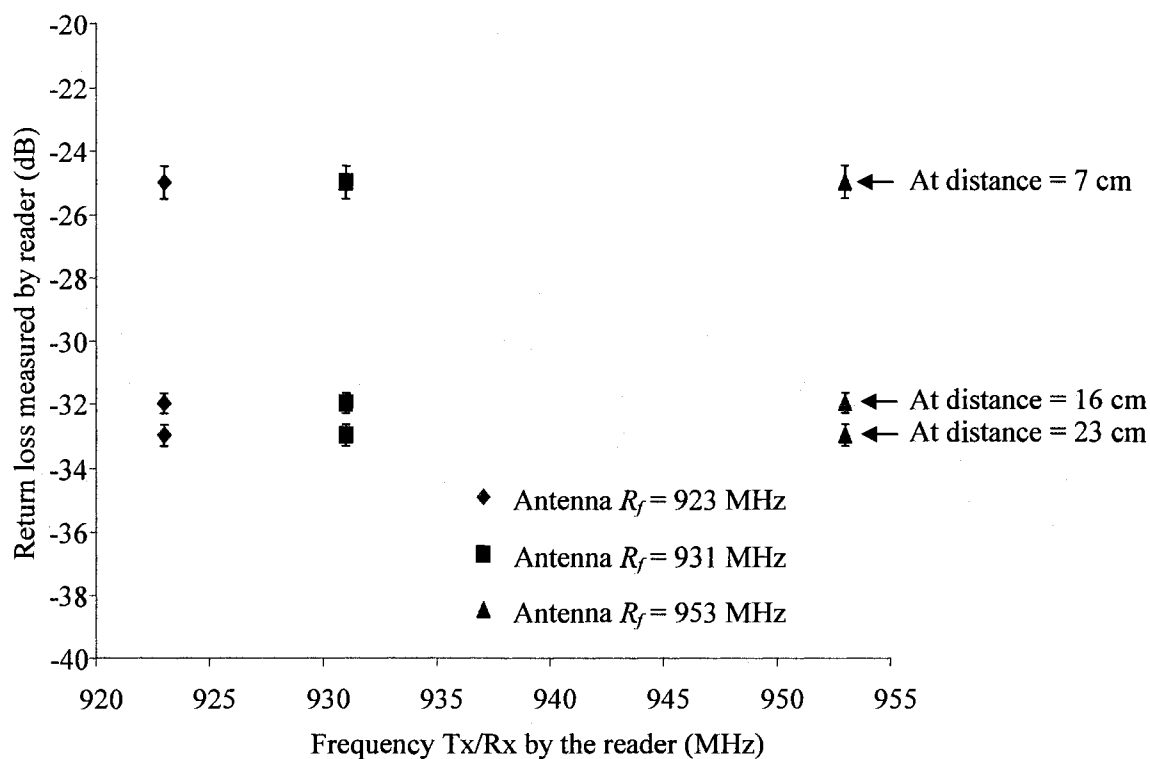


Figure 6.14 Multiple tag detection at varying distances.

However, the presented sensor tag can still be used for applications related to reading one carton of fruit at a time when loading and unloading the fruit cartons using conveyer belt systems. Each carton would contain a sensor tag operating at the same frequency and the change in ethylene concentration in the individual carton would result

in a corresponding change in return loss of the particular sensor tag. Thus the reader can detect if the carton contains unripe, ripe, or over-ripe fruit.

6.4 RFID Reader System

The RFID reader used for the sensor tag readout is a simple custom built reader presented by Shrestha, et al. in [90]. This reader is designed to read passive sensor tags working on the principle of the signal amplitude variation being proportional to the stimulant.

6.4.1 Reader Output Data

As shown in Figure 6.15, the RFID reader system consists of an analog reader section, an analog to digital converter, a single board computer, and peripherals to communicate with the outside world through cyber space. The reader sends a 915 MHz continuous sinusoidal signal to the sensor tag and receives the backscattered signal from the tag. The amplitude of the received signal changes according to the concentration of ethylene sensed by the sensor.

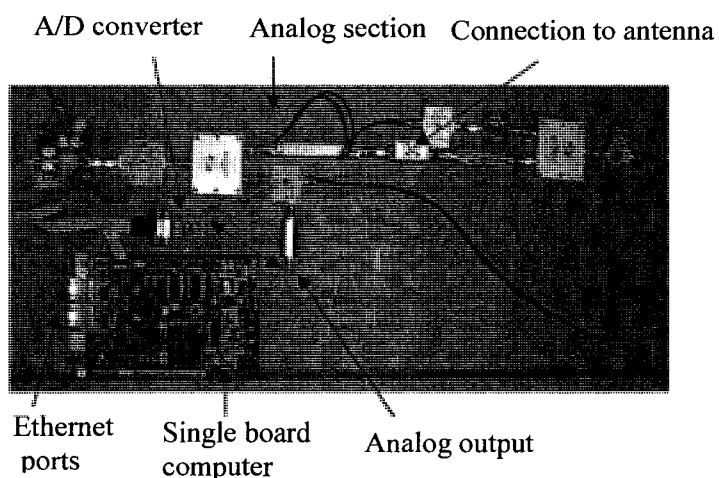


Figure 6.15 Modular prototype of the RFID reader system [90].

The change in amplitude is compared with the original signal transmitted and the amount of change in signal amplitude is translated as the concentration of ethylene sensed.

6.4.2 Experimental Results

The experimental set-up for the sensor tag output data measurement with the reader is given in Figure 6.16. The distance between the sensor tag and the reader antenna is optimized as 16 cm using the distance optimization technique explained in section 5.2.3.

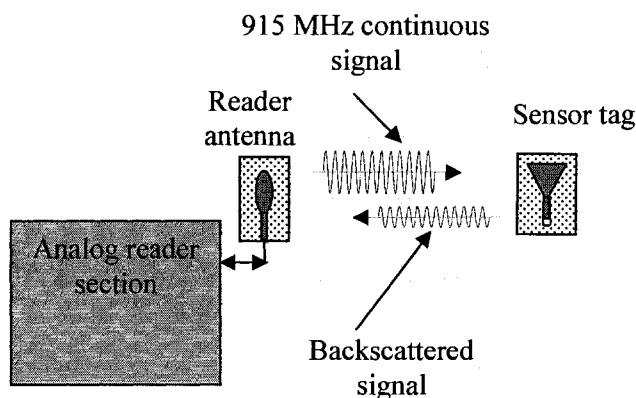


Figure 6.16 Experimental set-up for sensor tag detection of ethylene with reader.

The reader antenna is a circular disc monopole antenna with a wide band width of -10 dB around 915 MHz, as given in [72]. The sensor tag, which comprises the sensor integrated with the triangular patch antenna, is placed inside a chamber. Ethylene gas of concentration 0 ppm to 100 ppm was supplied to the chamber containing the sensor tag. When the sensor senses the ethylene, the antenna parameters vary in accordance with the concentration of ethylene present inside the chamber. The changes in the sensor tag affect the amplitude of the backscattered signal reaching the reader antenna. The backscattered signal is compared with the original signal and the output of the reader is the

demodulated output signal amplitude read on a display. Figure 6.17 shows the reader output data for a sensor tag tested over time. The solid line represents the linear fit to the displayed measured data points. An overall change of 3 mV was observed.

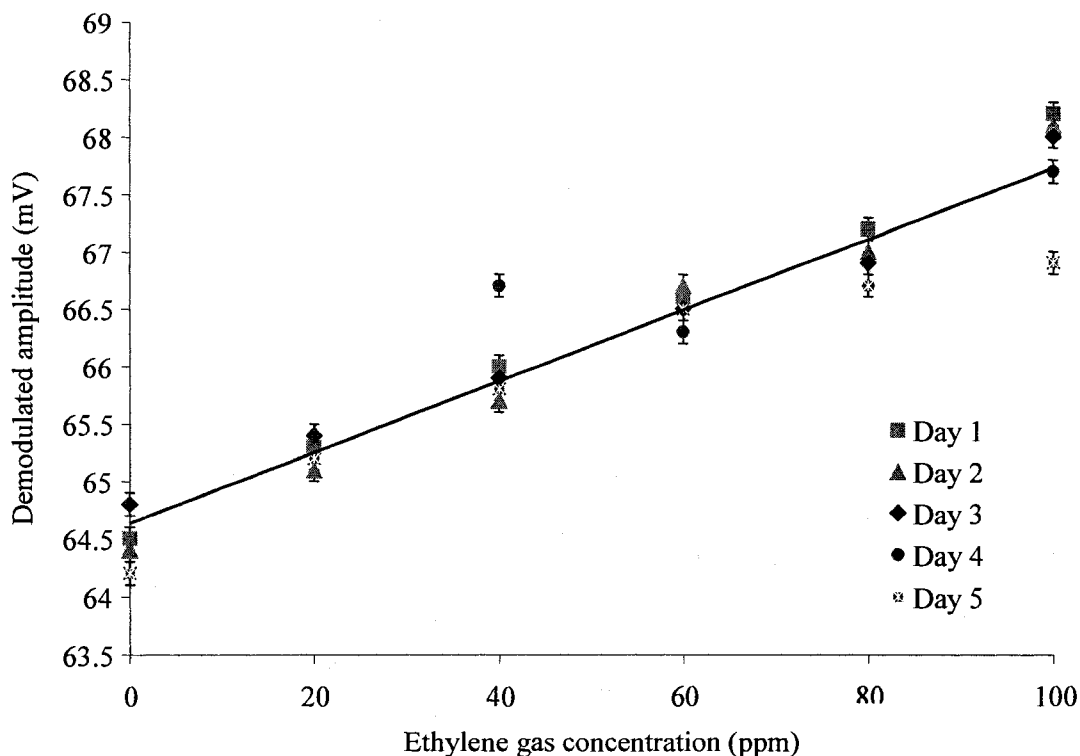


Figure 6.17 Reader output data of sensor tag sensing ethylene gas.

From the results presented in this chapter we can conclude that the sensor tag as designed has been successfully tested for wireless detection of ethylene gas with a network analyzer and 915 MHz RFID reader. Detecting the freshness status of the fruits under observation can be achieved by setting the reader to alert the user for specific ppm levels to indicate the status of the fruits as raw, ripe, over-ripe, and spoilt.

CHAPTER 7

CONCLUSIONS AND FUTURE WORK

7.1 Conclusions

In this dissertation, we present a novel SnO₂ nanoparticle based capacitive ethylene sensor integrated with a triangular microstrip patch antenna operating at 915 MHz for wireless monitoring of climacteric fruit freshness. Unlike other reported SnO₂ resistor based sensors, the SnO₂ capacitor based model senses ethylene at room temperature, which is achieved by coating a thin dielectric sensing layer of 1200 nm using 10 nm to 15 nm SnO₂ nanoparticles. The sensor was fabricated at room temperature using a dip coating technique on a flexible polyimide substrate. The dissertation also presents the sensitivity, selectivity, reproducibility, response and recovery time, and degradation study for the sensor. Pure SnO₂ and SnO₂ with a Pt/Pd layer were used as the dielectric sensing layer to improve the sensor performance.

The direct integration of the sensor with a triangular patch antenna using the capacitive loading technique represents a one of a kind sensor tag for ethylene gas sensing. The ethylene gas concentration was wirelessly monitored using two methods of detection: (1) return loss measurement method, which uses another transmitting/receiving

antenna connected to a network analyzer to monitor the changes in return loss of the antenna integrated with sensor, (2) backscattered signal amplitude method, which uses a RFID reader to wirelessly monitor the changes in backscattered voltage from the sensor tag due to the presence of ethylene gas.

Preliminary results have been presented for detecting multiple sensor tags placed at varying distances from the transmitting/receiving antenna. This was achieved by sweeping a range of frequencies and measuring the return loss at each specified resonant frequency of the tag antenna.

In a summary, this research leads to the following results and conclusions:

- A capacitive ethylene sensor with the pure SnO₂ as the sensing dielectric layer decreased in capacitance by 5 pF when ethylene gas concentration was increased from 0 ppm to 100 ppm.
- The use of a Pt/Pd layer with the SnO₂ layer further decreases the change in capacitance by 7 pF. These samples also showed a better selectivity to ethylene gas in a CO₂ environment (1000 ppm, 2000 ppm, and 3000 ppm) by showing an overall decrease in 7 pF of capacitance, which is the same as the pure ethylene gas environment. Whereas, the samples with pure SnO₂ showed an overall decrease in capacitance of 6 pF for ethylene gas in a CO₂ environment as compared to the pure ethylene gas environment change in capacitance of 5 pF, thus proving its cross sensitivity to CO₂ gas.
- The samples with sensing dielectric layer of SnO₂ with a Pt/Pd layer also had a better response time of 3 min when compared to the response time of 5 min for pure SnO₂ samples.

- However, pure SnO₂ samples showed lower hysteresis, better reproducibility, and lower degradation than samples of SnO₂ with a Pt/Pd layer.
- The sensor was integrated with the triangular microstrip patch antenna using the capacitive loading technique and an overall increase in resonant frequency and return loss of the antenna was 7 MHz and 9.5 dB, respectively. Almost 2 dB of reduction in return loss at the antenna resonant frequency was observed for every 20 ppm of change in ethylene gas concentration, which is high enough for the effective determination of the intermediate ethylene concentration values.
- The capacitive loading technique adapted for the integration of the capacitive ethylene sensor to the feed end of the triangular patch antenna reduced the size of the antenna by 63 percent.
- The detection range of the sensor tag (operating in the UHF range of 915 MHz) was at 16 cm making the tag operable in the far field range as compared to some of the near field (of few mm distance) wireless RFID sensor tag detectors.
- The sensor tag was also detected by a reader and showed an overall increase of 3 mV for the backscattered demodulated signal amplitude.

The presented sensor tag is a passive, low cost, and planar design applicable for sensing ethylene gas concentration wirelessly. Hence, it can be effectively applied for wireless monitoring of the freshness of climacteric fruit based on the concentration of ethylene gas evolved at different stages of ripening during transport and storage.

7.2 Future Work

The future research work pertaining to the presented passive ethylene gas sensor is given as follows.

- The overall sensor parameters such as sensitivity, selectivity, etc can be improved by using different dopants. For instance, from the related research presented in Chapter 2, we know that WO_3 and TiO_2 are other materials which are known for their selective sensitivity to ethylene gas. Doping these materials with SnO_2 could result in increased sensitivity and selectivity. The sensitivity of the sensor can also be improved by using an interdigitated capacitor model [91] with the two plates fabricated with dielectric gap, as shown in Figure 7.1.

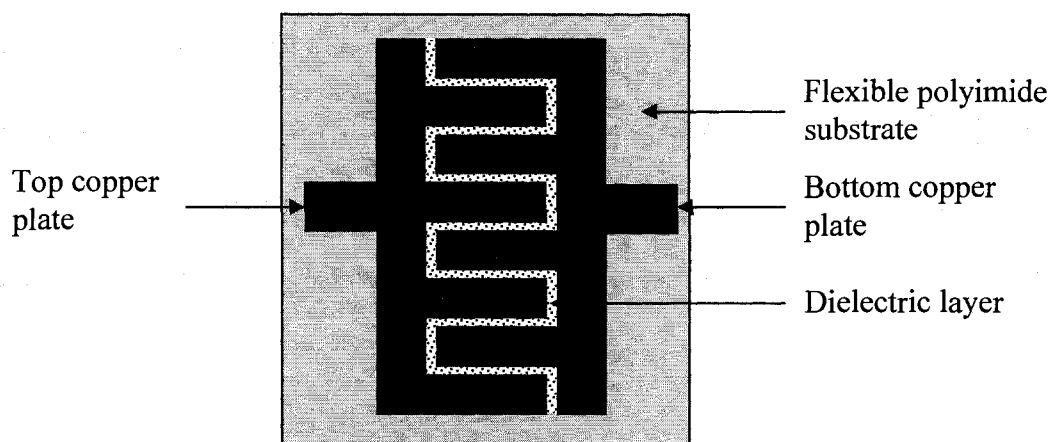


Figure 7.1 Top view of interdigitated capacitor model.

The sensing dielectric layer is then deposited in the gap using dip coating between the two plates and thus forming a parallel plate capacitor in the horizontal plane. This interdigitated capacitor model maximizes the exposure of the sensing dielectric layer to the stimulant instead of relying on the diffusion of

the stimulant in the present capacitor model with the top plate deposited on top of the dielectric layer. This will also reduce the fabrication process by two steps by eliminating the need for the insulating layer used to prevent shorts and e-beam deposition of the top copper plate. Using this model, the capacitor performance can be improved when integrated with 915 MHz RFID antenna as the uneven deposition of the top copper plate (due to ridges in the coated SnO₂ layer) is eliminated.

- Other sensor models like a diode can be designed using SnO₂ as the sensing layer in the MIS diode configurations. This will cause a non-linear output which can be used as a switch in triggering the sensor in the ON mode or OFF mode.
- Challenges do exist in the improvement and optimization of the fabrication process at room temperature for depositing the sensing layer as it tends to crack when the substrate is strained due to bending.
- The application of this sensor tag can be extended to other areas of applications by simply replacing the ethylene sensing dielectric layer with other (temperature, humidity, pressure etc) sensing dielectric layer.
- Presently the ethylene sensor is unprotected and is prone to physical and chemical damages. For example the SnO₂ coating can be removed by physical contact and the copper plates are subjected to oxidation reaction over time. Hence, there is a research need for using a protective layer.

The future work pertaining to the presented sensor tag is given as follows.

- The overall increase in the demodulated signal output amplitude was 3 mV when detected by a reader in a laboratory set-up with anechoic chamber. Importance

should be given to increase the amount of change in the demodulated backscattered voltage to about 20 mV to avoid misreading by the reader due to the dominance of amplitude noise. Increasing the measured backscattered voltage also aids in the effective measurement in the on-site storage facilities without the use of the anechoic chamber.

- Presently the efficiency of the sensor tag in monitoring the climacteric fruit freshness is limited to sensing only the ethylene gas evolved. This can be greatly improved if other fruit damaging factors, like temperature variations and bacterial infections, can also be monitored by using multiple sensors in the sensor tag. Also, the application of monitoring freshness of climacteric fruit can also be extended to non-climacteric fruits by monitoring the CO₂ levels emitted during its ripening stage in the plant itself so that the fruits are picked at a mature state for transport and storage.

APPENDIX A

SAS PROGRAM AND OUTPUT DATA FOR THE STANDALONE ETHYLENE SENSOR

A.1 SAS Program

The SAS program for plotting the linear fit for the experimental data points for the sensitivity of pure SnO₂ obtained for Sample 1 is given below. The overall SAS program structure for generating the statistical analysis and plot remain the same for all the data points. Only the input data is changed for each set of experimental values. The x-axis is the ethylene gas concentration (conc) and the y-axis represents the normalized capacitance (capc).

```
data Sensitivity of pure SnO2 for Sample 1;
input conc capc;
cards;

0      0
20     -1.2
40     -1.9
60     -2.6
80     -3.3
100    -5.2
;

ods pdf file="DATA1.pdf";
axis1 label=(angle=90 "Normalized capacitance (pF)");
axis2 label=("Ethylene gas concentration (ppm)");
proc gplot data= Sensitivity of pure SnO2 for Sample 1;
plot capc*conc/vaxis=axis1 haxis=axis2;
run;

proc reg;
    model capc = conc;
plot capc*conc;
run;
ods pdf close;
quit;
```

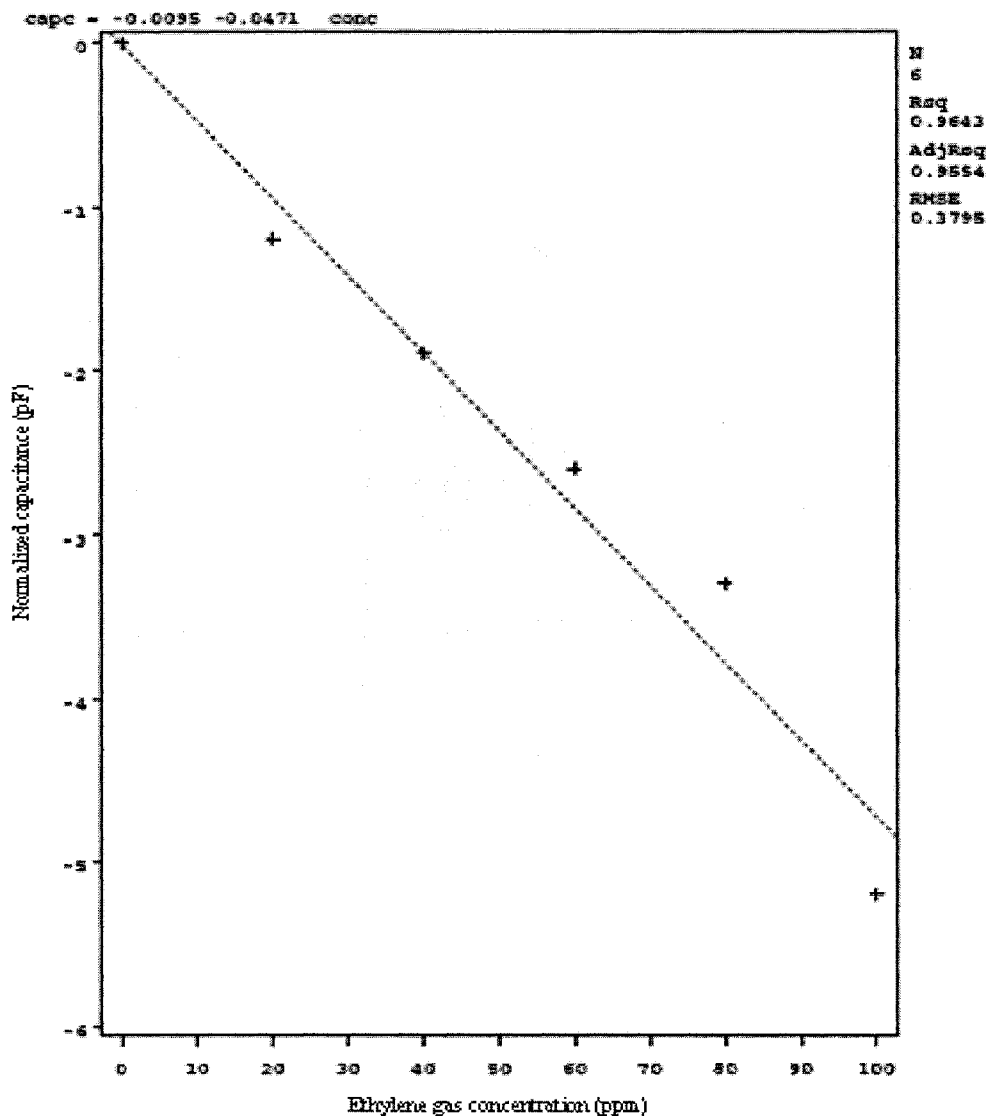
A.2 Output Data

The output data obtained for the above program is given as follows. Similar data output was obtained for all the other data points. The number of data points taken for the SAS analysis is 6, of which the predicted values and square sum of error are calculated for 4 data points.

<i>The SAS System</i>					
<i>The REG Procedure</i>					
<i>Model: MODEL1</i>					
<i>Dependent Variable: cupc</i>					
Number of Observations Read					6
Number of Observations Used					6
Analysis of Variance					
Source	DF	Sum of Squares	Mean Square	F Value	Pr > F
Model	1	15.55714	15.55714	108.00	0.0005
Error	4	0.57619	0.14405		
Corrected Total	5	16.13333			
Root MSE		0.37954	R-Square		0.9643
Dependent Mean		-2.36667	Adj R-Sq		0.9554
Coeff Var		-16.03673			
Parameter Estimates					
Variable	DF	Parameter Estimate	Standard Error	t Value	Pr > t
Intercept	1	-0.00952	0.27469	-0.03	0.9740
conc	1	-0.04714	0.00454	-10.39	0.0005

A.3 Output Plot

The output plot obtained for the above program is given below. The linear fit obtained ($\text{capc} = -0.0095 - 0.0471 \text{conc}$) gives the slope and the intercept values for the experimental data points. The plot also gives the number of data used and the root mean square error of the data points with respect to the predicted values.



APPENDIX B

CALCULATIONS FOR CO₂ GAS CONCENTRATION

The calculations for filling 1000, 2000, and 3000 ppm of CO₂ gas in the chamber for the selectivity experiments using the given equipments are given below. The available data are,

Size of the gas chamber = 2.15 L

Total amount of CO₂ gas required = 1000 ppm

Pressure of the gas inside the CO₂ gas cylinder (p) = 550 psi = 37.425 atm

Flow rate of flowmeter = 1 SCFH = 0.472 L/min

We know that 1 mg per L = 1 ppm, Hence, in order to fill a chamber of 2.15 L with 1000 ppm, we need 2150 mg of the gas.

Molar mass of CO₂ = 12 + (16 x 2) = 44 g/Mol.

The number of moles (*n*) present in 44g of CO₂ is 2.15/44 = 0.04886 moles.

The total number of moles (*N*) required with a flow rate of 0.472 L/min to fill the 2.15 L chamber is given as,

$$N = \frac{pv}{RT}$$

Where *p* is the pressure, *v* is the volume, *R* is the universal gas constant (0.082057 L atm mole⁻¹ K⁻¹), and *T* is the temperature in Kelvin (300 K).

$$N = \frac{37.425 \times 0.472}{0.082057 \times 300} = 0.717574 \text{ moles}$$

The time (*t*) required to fill 2.15 L of the chamber with flow rate of CO₂ gas of 1 SCFH under 550 psi pressure is given as,

$$t = \frac{n}{N}$$

$$\begin{aligned}
 &= \frac{0.04886}{0.717574} \\
 &= 0.0680905 \text{ min} \\
 &\approx 4 \text{ sec}
 \end{aligned}$$

Thus, for filling 1000 ppm of CO₂ gas we need 4 sec. But there is 300 ppm of CO₂ gas in air which is already present inside the chamber which has to be taken into account as the CO₂ gas is pumped into the chamber with the outlet closed.

Therefore, for 1000 ppm we require the flowmeter to be open for 4 sec, then for 700 ppm we need to keep the flowmeter open for 2.8 sec which can be approximated to 3 sec. The summary of the time required for 1000, 2000, and 3000 ppm is given below.

Concentration of CO ₂ gas (ppm)	Time (Sec)
1000 (actual 700)	3
2000 (actual 1700)	7
3000 (actual 2700)	11

REFERENCES

- [1] S. R. Harris, "Production is only half the battle," Training manual, Food and Agriculture Organization of United Nations, Bridgetown, Barbados, December 1988.
- [2] O. P.-Lopez, *Molecular Biotechnology for Plant Food Production*. Lancaster, Pennsylvania, CRC Press, 1999, ch. 8.
- [3] A. A. Kader, "Increasing food availability by reducing postharvest losses of fresh produce," Proceedings of 5th Int. Postharvest Symp. Acta Hort., 682, pp. 2169-2176, 2005.
- [4] J. B. Biale, R. E. Young, and A. J. Olmstead, "Fruit respiration and ethylene production," *Plant Physiology*, vol. 29, no. 2, pp. 168–174, March 1954.
- [5] M. A. Ritenour and J. K. Brecht, "Ethylene treatments for ripening and degreening," Postharvest Institute at Florida Agricultural Conference & Trade Show, April 2003.
- [6] J. Lapworth, "A novel approach (scoring system) for integrating dissolved gas analysis results into a life management system," IEEE International Symposium on Electrical Insulation, Boston, Massachusetts, April 2002.
- [7] C. Alonso, T. Gasmi, A. Ureña, "Dial remote sensed ethylene and ozone-Ethylene correlation in presence of urban NO_x," *Journal of Atmospheric Chemistry*, vol. 50, no. 2, pp. 159-169, February 2005.
- [8] M. Z. Jacobson, *Fundamentals of atmospheric monitoring*. New York, Cambridge University Press, 2005.
- [9] G. Giubileo, L. D. Dominicis, R. Fantoni, M. Francucci, A. C. Castellano, M. G. Furfaro, S. Gaudenzi, A. Antonini, and C. C. Lombardi, "Photoacoustic detection of ethylene traces in biogenic gases," *Laser Physics*, vol. 12, pp. 653–655, 2002.
- [10] M. Jones, "Ethylene contamination: Symptoms and sources in the greenhouse," Northwest Ohio's Commercial Floriculture RESOURCE Newsletter, Department of Horticulture and Crop Science, The Ohio State University.

- [11] K. Ihokura and J. Watson, *The stannic oxide gas sensor: Principles and applications*, Boca Raton, Florida, CRS Press, 1994.
- [12] *General Information for TGS Sensors*, Figaro Technique Manual, pp. 2, 1998.
- [13] M. Madou, "Application of micromachining in solid-state chemical sensors," *Opportunities for innovation: Chemical and biological sensors*, NIST, 1991.
- [14] P. Ivanov, E. Llobet, A. Vergara, M. Stankova, X. Vilanova, J. Hubalek, I. Gracia, C. Cané, and X. Correig, "Towards a micro-system for monitoring ethylene in warehouses," *Sensors and Actuators B: Chemical*, vol. 110, no. 2, pp. 63-70, November 2005.
- [15] A. Giberti, M. C. Carotta, V. Guidi, C. Malagù, M. Piga, and G. Martinelli, "Monitoring of ethylene for agro-alimentary applications and compensation of humidity effects," *Proceedings of Eurosensor XVII*, 2003.
- [16] B. S. Kang, S. Kim, F. Rem, B. P. Gila, C. R. Abernathy, and S. J. Pearton, "AlGaIn/GaN based diodes and gateless HEMTs for gas and chemical sensing," *IEEE Sensors Journal*, vol. 5, no. 4, pp.677-680, August 2005.
- [17] B. S. Kang, S. Kim, F. Ren, K. Ip, Y. W. Heo, B. Gila, C. R. Abernathy, D. P. Norton, and S. J. Pearton, "Detection of C₂H₄ using wide-bandgap semiconductor sensors AlGaIn/GaN MOS diodes and bulk ZnO schottky rectifiers," *Journal of the Electrochemical Society*, vol. 151, no. 7, pp. G468-G471, 2004.
- [18] H. Cheraga, S. Belhousse, and N. Gabouze, "Characterization of a new sensing device based on hydrocarbon groups (CH_x) coated porous silicon," *Applied Surface Science*, vol. 238, no. 1- 4, pp. 495-500, November 2004.
- [19] F. Winqvist, I. Lundstrom, and H. Bergkvist, "Ethylene production from fruits measured by a simple field-effect structure and compared with a gas chromatographic method," *Analytica Chimica Acta*, vol. 231, no. 1, pp. 93-100, 1990.
- [20] F. Winqvist and I. Lundstrom, "Thin metal film-oxide-semiconductor structures with temperature-dependent sensitivity for unsaturated hydrocarbons," *Sensors and Actuators*, vol. 12, no. 3, pp. 255-261, 1987.
- [21] B. Pietrucha and B. Lalevic, "Detection of hydrocarbon gases using Pd-MNOS capacitors," *Sensors and Actuators*, vol. 13, no. 3, pp. 275-286, 1988.
- [22] C. H. Kwon, H. Hong, S. T. Kim, K. C. Lee, D. H. Yun, H. W. Shin, and H. S. Park, "Vegetable freshness keeping device having a sensor," U.S. Patent 5609096, March 11, 1997.

- [23] S. Pitcher, J. A. Thiele, H. Ren, and J. F. Vetelino, "Current/voltage characteristics of a semiconductor metal oxide gas sensor," *Sensors and Actuators B: Chemical*, vol. 93, no. 1, pp. 454-462, August 2003.
- [24] R. Zhang, M. I. Tejedor, M. A. Anderson, M. Paulose, and C. A. Grimes, "Ethylene detection using nanoporous PtTiO₂ coatings applied to magnetoelastic thick films," *Sensors*, 2, 331-338, 2002.
- [25] H. Molero, D. Stacchiola, and W. T. Tysoe, "The kinetics of ethylene hydrogenation catalyzed by metallic palladium," *Catalysis letters*, vol. 101, no. 3-4, pp. 145-149, 2005.
- [26] Helmut Öfner and Francisco Zaera, "Ethylene adsorption on platinum: Kinetics, bonding, and relevance to catalysis," *Journal of the American Chemical Society*, vol. 124, no. 37, pp. 10982 -10983, August 2002.
- [27] S. C. Pyke, "Detection of fluids with metal-insulator-semiconductor sensors," U.S. Patent 5591321, January, 1997.
- [28] A. Chiorino, G. Ghiotti, M. C. Carotta, and G. Martinelli "Electrical and spectroscopic characterization of SnO₂ and Pd-SnO₂ thick films studied as CO gas sensors," *Sensors and Actuators B: Chemical*, vol. 47, no. 1-3, pp. 205-212. April 1998.
- [29] Th. Becker, S. Ahlers, Chr. Bosch-v.Braunmühl, G. Müller, and O. Kiesewetter "Gas sensing properties of thin- and thick-film tin-oxide materials," *Sensors and Actuators B: Chemical*, vol. 77, no. 1-2, 15, pp. 55-61, June 2000.
- [30] L. R. Jordan, P. C. Hauser, and G. A. Dawson, "Humidity and temperature effects on the response to ethylene of an amperometric sensor utilizing a gold-nafion electrode," *Electroanalysis*, vol. 9, no. 15, pp. 1159-1162, April 2005.
- [31] J. Liu, X. Huang, G. Ye, W. Liu, Z. Jiao, W. Chao, Z. Zhou, and Z. Yu, "H₂S detection sensing characteristic of CuO/SnO₂ sensor," *Sensors*, vol. 3, pp. 110-118, 2003.
- [32] E. Llobet, P. Ivanov, X. Vilanova, J. Brezmes, J. Hubalek, K. Malysz, I. Gràcia, C. Cané, and X. Correig, "Screen-printed nanoparticle tin oxide films for high-yield sensor Microsystems," *Sensors and Actuators B: Chemical*, vol. 96, no. 1-2, pp. 94-10, November 2003.
- [33] B. Cavicchi, M.C. Carotta, M. Ferroni, G. Martinelli, M. Piga, and S. Gherardi, "Au-, Pd-, Pt-doped thick films for gas sensing," International Meeting on Chemical Sensors, Boston, pp.142, July 2002.

- [34] R. S. Niranjana and I. S. Mulla, "Spin coated tin oxide: A highly sensitive hydrocarbon sensor," *Materials Science and Engineering B: Solid-State Materials for Advanced Technology*, vol. 103, no. 2, pp. 103-107, October 2003.
- [35] J. Arbiol, "Metal additive distribution in TiO₂ and SnO₂ semiconductor gas sensor nanostructured materials," Ph.D. Dissertation, University of Barcelona, Spain, 2001.
- [36] L. E. Depero, L. Sangaletti, B. Allieri, E. Bontempi, A. Marino, and M. Zocchi, "Correlation between crystallite sizes and microstrains in TiO₂ nanopowders," *Journal of Crystal Growth*, vol.198, pp. 516-520 Part 1, March 1999.
- [37] M. Radecka, K. Zakrzewska, and M. R. kas, "SnO₂-TiO₂ solid solutions for gas sensors," *Sensors and Actuators B: Chemical*, vol. 47, no. 1-3, pp. 194-20, April 1998.
- [38] M. Epifani, L. Francioso, P. Siciliano, A. Helwig, G. Mueller, R. Díaz, J. Arbiol, and J. R. Morante, "SnO₂ thin films from metalorganic precursors: Synthesis, characterization, microelectronic processing and gas-sensing properties," *Sensors and Actuators B: Chemical*, vol. 124, no. 1, pp. 217-226, June 2007.
- [39] S. Majumder, S. Hussain, R. Bhar, and A.K. Pal, "Liquid petroleum gas sensor based on SnO₂/Pd composite films deposited on Si/SiO₂ substrates," *Vacuum*, vol 81, no. 8, pp. 985-996, March 2007.
- [40] S. Tanaka and T. Esaka, "High NO_x sensitivity of oxide thin films prepared by RF sputtering," *Materials Research Bulletin*, vol. 35, no. 14-15, pp. 2491-2502, November 2000.
- [41] G. I. Garrido, F. C. Patcas, G. Upper, M. Türk, S. Yilmaz, and B. Kraushaar-Czarnetzki, "Supercritical deposition of Pt on SnO₂-coated Al₂O₃ foams: Phase behaviour and catalytic performance," *Applied Catalysis A: General*, vol. 338, no. 1-2, pp. 58-65, April 2008.
- [42] K. Sekizawa, H. Widjaja, S. Maeda, Y. Ozawa, and K. Eguchi, "Low temperature oxidation of methane over Pd/SnO₂ catalyst," *Applied Catalysis A: General*, vol. 200, no. 1-2, pp. 211-217, August 2000.
- [43] M. H. M. Reddy and A. N. Chandorkar, "E-beam deposited SnO₂, Pt-SnO₂ and Pd-SnO₂ thin films for LPG detection," *Thin Solid Films*, vol. 349, no. 1-2, pp. 260-265, July 1999.

- [44] A. M. Serventi, R. Dolbec, M. A. El Khakani, R. G. Saint-Jacques, and D. G. Rickerby, "High-resolution transmission electron microscopy investigation of the nanostructure of undoped and Pt-doped nanocrystalline pulsed laser deposited SnO₂ thin films," *Journal of Physics and Chemistry of Solids*, vol. 64, no. 11, pp. 2097-2103, November 2003.
- [45] A. Pereira, L. Cultrera, A. Dima, M. Susu, A. Perrone, H. L. Du, A. O. Volkov, R. Cutting, and P. K. Datta, "Pulsed laser deposition and characterization of textured Pd-doped-SnO₂ thin films for gas sensing applications," *Thin Solid Films*, vol. 497, no. 1-2, 21, pp. 142-148, February 2006.
- [46] E. D. Butrym and T. G. Hartman, "Determination of ethylene by adsorbent trapping and thermal desorption-Gas chromatography," *PittCon. 98*, New Orleans, LA, March 1998.
- [47] D. Weidmann, A. A. Kosterev, C. Roller, R. F. Curl, M. P. Fraser, and F. K. Tittel, "Monitoring of ethylene by a pulsed quantum cascade laser," *Applied Optics*, vol. 43, no. 16, pp. 3329-3334, June 2004.
- [48] N. Quickert, W. J. Findlay, and J. L. Monkman, "Modification of a chemiluminescent ozone monitor for the measurement of gaseous unsaturated hydrocarbons," *Science of the Total Environment*, vol. 3, no. 4, pp. 323-328, 1974.
- [49] S. Hartwig, J. Hildenbrand, M. Moreno, J. Fonollosa, L. Fonseca, J. Santander, R. Rubio, C. Cane, A. Lambrecht, and J. Wöllenstein, "A highly sensitive IR-optical sensor for ethylene-monitoring," *Smart Sensors, Actuators, and MEMS II. Proceedings of the SPIE*, vol. 5836, pp. 452-460, May 2005.
- [50] J. N. Burstyn, A. B. Ellis, O. Green, and N. A. Smith, "Photoluminescent ethylene sensors," U.S. Patent 7105274, September, 2006.
- [51] C. H. Kwon, H. -K. Kong, S. T. Kim, K. C. Lee, D. H. Yun, H. W. Shin, and H. S. Park, "Vegetable freshness keeping device having a sensor," U.S. Patent 5609096, March, 1997.
- [52] I. Gagnadre, C. Gagnadre, and J. P. Fenelon, "Circular patch antenna sensor for moisture content measurement on dielectric material," *Electronics Letters*, vol. 31, no. 14, pp. 1167 - 1168, 1995.
- [53] K. Chang, Y. H. Kim, Y. J. Kim, and Y. J. Yoon, "Functional antenna integrated with relative humidity sensor using synthesized polyimide for passive RFID sensing," *Electronics Letters*, vol. 43, no. 5, pp. 7-8, March 2007.

- [54] T. J. Harpster, B. Stark, and K. Najafi, "A passive wireless integrated humidity sensor," *Sensors and Actuators A: Physical*, vol. 95, no. 2, pp. 100-107, January 2002.
- [55] A. Denoth, "The monopole-antenna: A practical snow and soil wetness sensor," *IEEE Transactions on Geoscience and Remote Sensing*, vol. 35, no. 5, pp. 1371-1375, September 1997.
- [56] M. Bogosanovich, "Microstrip patch sensor for measurement of the permittivity of homogeneous dielectric materials," *IEEE Transactions on Instrumentation and Measurement*, vol. 49, no. 5, pp. 1144-1148, October 2000.
- [57] V. Thomy, L. Dubois, C. Vanoverschelde, J. Sozanski, and J. Pribetich, "New antenna-sensor for temperature control by microwave radiometry," *Proceedings of IEEE Sensors*, vol. 1, no. 2, pp. 1308-1312, 2002.
- [58] S. Nambi, S. Nyalamadugu, S. M. Wentworth, and B. A. Chin, "Radio frequency identification sensors," Technical report, Auburn University, 2003.
- [59] G. W. Pope, T. E. Myers, S. Kaye, and J. Burchell, "Shelf-life monitoring sensor-transponder system," U.S. Patent 0248455, November, 2005.
- [60] A. Vergara, E. Llobet, J. L. Ramirez, P. I vanov, L. Fonseca, S. Zampolli, A. Scorzoni, T. Becker, S. Marco, and J. Wollenstein, "An RFID reader with onboard sensing capability for monitoring fruit quality," *Sensors and Actuators B* vol. 127, no. 1, pp. 143-149, August 2007.
- [61] M. D. Balachandran, S. Shrestha, M. Agarwal, Y. Lvov, and K. Varahramyan, "SnO₂ capacitive sensor integrated with microstrip patch antenna for passive wireless detection of ethylene gas," *IEE Electronics Letters*, vol. 44, no. 7, pp. 464-466, March 2008.
- [62] T. N. Agarwal and R. N. Saxena, "Tin oxide thin film capacitors," *Indian Journal of Pure and Applied Physics*, vol. 19, pp. 1057-1061, November 1981.
- [63] G. Korotcenkov, "Gas response control through structural and chemical modification of metal oxide films: State of the art and approaches," *Sensors and Actuators B*, vol. 107, no. 1, pp. 209-232, 2005.
- [64] J. Gong, W. Fei, Z. Xia, Q. Chen, S. Seal, and L. C. Chow, "Development of micromachined nanocrystalline mesoporous SnO₂ gas sensor for electronic nose," *Proceedings of IEEE Sensors*, vol. 1, no. 22-24, Oct. 2003.
- [65] J. Lu, C. Tang, and K. Wong, "Slot-coupled compact broadband circular microstrip antenna with chip-resistor and chip-capacitor loadings," *Microwave and Optical Technology Letters*, vol. 18, no. 5, pp. 345-349, 1998.

- [66] Z. M. Jarzebski, "Physical properties of SnO₂ materials," *Journal of the Electrochemical Society*, vol. 123, no. 7, pp. 199C-205C, 1976.
- [67] G. Korotcenkov, A. Cornet, E. Rossinyol, J. Arbiol, V. Brinzari, and Y. Blinov, "Faceting characterization of SnO₂ nanocrystals deposited by spray pyrolysis from SnCl₄-5H₂O water solution," *Thin Solid Films*, vol. 471, no. 1-2, pp. 310-319, 2004.
- [68] B. Kamp, R. Merkle, R. Lauck, and J. Maier, "Chemical diffusion of oxygen in tin dioxide: Effects of dopants and oxygen partial pressure," *Journal of Solid State Chemistry*, vol. 178, no. 10, pp. 3027-3039, October 2005.
- [69] R. B. Vasiliev, M. N. Romyantseva, S. G. Dorofeev, Y. M. Potashnikova, L. I. Ryabova, and A. M. Gaskov, "Crystallite size effect on the conductivity of the ultradisperse ceramics of SnO₂ and In₂O₃," *Mendeleev Communications*, vol. 14, no. 4, pp. 167-169, 2004.
- [70] H. M. Yates, M. E. Pemble, A. Blanco, H. Miguez, C. Lopez, and F. Meseguer, "Growth of tin oxide in opal," *Chemical Vapor Deposition*, vol. 6, no. 6, pp. 283 - 285, 2000.
- [71] G. Sakai, N. S. Baik, N. Miura, and N. Yamazoe, "Gas sensing properties of tin oxide thin films fabricated from hydrothermally treated nanoparticles. Dependence of CO and H₂ response on film thickness," *Sensors and Actuators B: Chemical*, vol. 77, no. 1-2, pp. 116-121, June 2001.
- [72] J. Vemagiri, "Design and development of triangular, spiral and fractal antennas for radio frequency identification tags," Ph.D. dissertation, Louisiana Tech University, 2006.
- [73] L. C. Godara, *Handbook of Antennas in Wireless Communications*, CRC Press, 2002.
- [74] Ansoft Designer, Version 2.0, Ansoft Corporation, March, 2004.
- [75] J. Vemagiri, M. Balachandran, M. Agarwal, and K. Varahramyan, "Development of compact half-Sierpinski fractal antenna for RFID applications," *Electronics Letters*, vol. 43, no. 22, October 2007.
- [76] S. Shrestha, M. Balachandran, M. Agarwal, L. H. Zou, and K. Varahramyan, "A method to measure radar cross section parameters of microstrip antennas," *IEEE Transaction on Antenna and Propagation*, submitted on January 2008.
- [77] <http://www.antennex.com/preview/vswr.htm>, Date accessed: March 14, 2008.

- [78] C. R. Rowell and R. D. Murch, "A capacitively loaded PIFA for compact mobile telephone handsets," *IEEE transactions on antennas and propagation*, vol. 45, no. 5, pp. 837-842, May 1997.
- [79] J. Thaysen and K. B. Jakobsen, "Capacitive top-loading of a mobile phone antenna for size reduction," JINA, International Symposium on Antennas, November 4 2004.
- [80] R. C. Ghan, Y. Lvov, and R. S. Besser, "Characterization of self-assembled SnO₂ nanoparticles for fabrication of a high sensitivity and high selectivity micro-gas sensor," *Proceedings of Materials Research Society Symposium*, vol. 703, pp. 297-302, 2002.
- [81] P. V. Nikitin, and K. V. S. Rao, "Theory and measurement of backscattering from RFID tags," *IEEE Antennas and Propagation Magazine*, vol. 48, no. 6, pp. 212-218, 2006.
- [82] R. Srivastava, R. Dwivedi, and S. K. Srivastava, "Effect of oxygen, nitrogen and hydrogen plasma processing on palladium doped tin oxide thick film gas sensors," *Physics of semiconductor devices*, vol. 3316, no. 2, pp. 526-528, 1998.
- [83] SAS, Version 9.1, SAS Institute Inc., Cary, North Carolina, USA, April 2003.
- [84] J. O. Dennis, M. M. A. Karim, Z. Ibrahim, and M. K. Saidin, "Hysteresis behaviour of sensitivity in CH₄ detection in air using SnO₂ with Pd as sensitizing additive," *Jurnal Teknologi C*, 36 (C). pp. 55-60, 2002.
- [85] G. Korotcenkov, V. Brinzari, Y. Boris, M. Ivanov, J. Schwank, and J. Morante, "Influence of surface Pd doping on gas sensing characteristics of SnO₂ thin films deposited by spray pyrolysis," *Thin Solid Films*, vol. 436, no. 1, pp. 119-126, July 2003.
- [86] M. Vallet, M. Brunel, F. Bretenaker, F. A. Le, J. -L. Adam, N.-H. Duhamel, J. -Y. Allain, H. S. M. de Vries, M. A. J. Wasono, F. J. M. Harren, E. J. Woltering, H.C.P.M van der Valk, and J. Reuss, "Ethylene and CO₂ emission rates and pathways in harvested fruits investigated, in situ, by laser photothermal deflection and photoacoustic techniques," *Postharvest Biology and Technology*, vol. 8, no. 1, pp. 1-10, April 1996.
- [87] T. Thomas and M. Skaria, "Air quality parameters in ethylene degreening rooms in the valley influence citrus fruit decay," Technical Report, Department of Agriculture, Texas A & M University, College Station, Texas, USA.
- [88] J. Gong, "Non-silicon microfabricated nanostructured chemical sensors for electric nose application," Ph.D. dissertation, University of Central Florida, 2005.

- [89] A. H. M. Z. Alam, R. Islam, and S. Khan, "Design of a tuning fork type UWB patch antenna," *International Journal of Computer Science and Engineering*, vol. 1, no. 4, pp. 240-243, 2007.
- [90] S. Shrestha, M. D. Balachandran, M. Agarwal, V. V. Phoha, and K. Varahramyan, "A chipless RFID sensor system for cyber centric monitoring applications," (Submitted for journal publication), May 2008.
- [91] K. Arshak, A. Arshak, D. Morris, O. Korostynska, and E. Jafer, "A wireless pressure measurement system based on TiO₂ interdigitated sensors," *Proceedings of IEEE Sensors*, October 31- November 3, 2005.